Model Predictive Control of Impedance Source Inverter for Photovoltaic Applications

2018

Sally Sajadian

Submitted to the graduate degree program in Elcetrical Engineering and Computer Science and the Graduate Faculty of the University of Kansas in partial fulfillment of the requirements for the degree of Doctor of Philosophy.

Chair: Reza Ahmadi

Member 2: Glenn Prescott

Member 3: Alessandro Salandrino

Member 4: James Stiles

Member 5: Huazhen Fang

Date Defended: 11 October 2018

The dissertation committee for Scholar Sally Sajadian that this is the approved version of the following

Model Predictive Control of Impedance Source Inverter for Photovoltaic Applications

Chair: Reza Ahmadi

Date Approved: 11 October 2018

ABSTRACT

A model predictive controlled power electronics interface (PEI) based on impedance source inverter for photovoltaic (PV) applications is proposed in this disssertation. The proposed system has the capability of operation in both grid-connected and islanded mode. Firstly, a model predictive based maximum power point tracking (MPPT) method is proposed for PV applications based on single stage grid-connected Z-source inverter (ZSI). This technique predicts the future behavior of the PV side voltage and current using a digital observer that estimates the parameters of the PV module. Therefore, by predicting *a priori* the behavior of the PV module and its corresponding effects on the system, it improves the control efficacy. The proposed method adaptively updates the perturbation size in the PV voltage using the predicted model of the system to reduce oscillations and increase convergence speed. The experimental results demonstrate fast dynamic response to changes in solar irradiance level, small oscillations around maximum power point at steady-state, and high MPPT effectiveness from low to high solar irradiance level.

The second part of this work focuses on the dual-mode operation of the proposed PEI based on ZSI with capability to operate in islanded and grid-connected mode. The transition from islanded to grid-connected mode and vice versa can cause significant deviation in voltage and current due to mismatch in phase, frequency, and amplitude of voltages. The proposed controller using MPC offers seamless transition between the two modes of operations. The main predictive controller objectives are decoupled power control in grid-connected mode and load voltage regulation in islanded mode. The proposed direct decoupled active and reactive power control in grid-connected mode enables the dual-mode ZSI to behave as a power conditioning unit for ancillary services such as reactive power compensation. The

proposed controller features simplicity, seamless transition between modes of operations, fast dynamic response, and small tracking error in steady state condition of controller objectives. The operation of the proposed system is verified experimentally.

The final part of this dissertation focuses on the low voltage ride through (LVRT) capability of the proposed PV systems during grid faults such as voltage sag. In normal grid condition mode, the maximum available power from the PV panels is injected into the grid. In this mode, the system can provide reactive power compensation as a power conditioning unit for ancillary services from DG systems to main ac grid. In case of grid faults, the proposed system changes the behavior of reactive power injection into the grid for LVRT operation according to the grid requirements. Thus, the proposed controller for ZSI is taking into account both the power quality issues and reactive power injection under abnormal grid condions.

Table of Contents

Table of Figures

Table of Tables

I. INTRODUCTION

A. Photovoltaic Power Electronics Interfaces

The economic and environmental implications of fossil fuel based electricity generation exacerbated by the growing power demand are the major motivations for recent efforts toward harnessing renewable energy sources. In fact, it is predicted that the renewable energy generation to be tripled within the next few decades [1, 2]. Photovoltaic (PV) systems are one of the most promising electric power generation systems due to their low environmental impact and high availability of solar irradiation in most geographical locations [3, 4]. The energy generated by the PV systems is highly dependent on the environmental and ambient conditions such as the solar irradiance level and the module temperature. In order to ensure extraction of the maximum available energy in any ambient condition, Maximum Power Point Tracking (MPPT) for PV systems is essential [5]. The Maximum Power Point (MPP) of a PV module corresponds to the knee of the current-voltage (I-V) characteristic curve of the module. The PV system efficiency can be degraded easily and consequently the amount of generated electric power can be reduced significantly if the PV module is not forced to operate at its MPP at all times regardless of the environmental conditions.

Conventional grid-tied PV systems typically use a two-stage power conversion topology: an upstream dc/dc power conversion stage from the PV module to a dc link energy buffer (such as a capacitor), and a downstream dc/ac power conversion stage from the energy buffer to the grid. Traditionally, in these systems the MPPT is implemented in the upstream conversion stage and is only responsible for transferring the maximum available energy from the PV module to the energy buffer. The downstream stage is responsible for controlling the flow of energy to the grid by

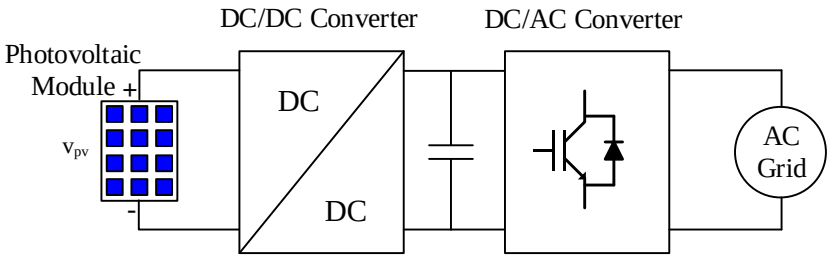

Fig. 1. Two stage grid-tied PV system configuration.

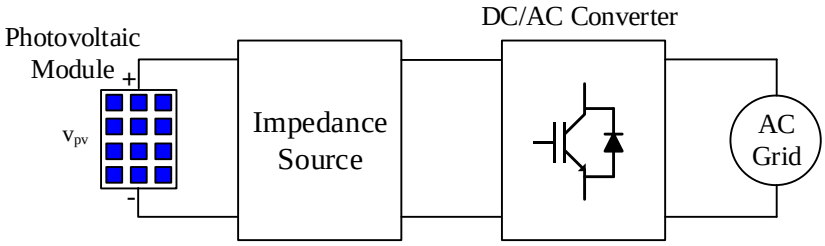

Fig. 2 Single stage impedance source grid-tied PV system configuration.

generating ac voltages that are synched with the grid voltage and controlling the power factor of the operation. The general schematic of a conventional two-stage grid-tied PV system is illustrated in Fig. 1.

The use of a two-stage topology is necessitated due to the inherent limitation of the dc/ac inverters for stepping up/down the voltage freely. Commonly, the conventional inverters classified as Voltage-Source Inverters (VSI) can only step-down the voltage while the Current-Source Inverters (CSI) can only step-up the voltage (the VSIs can have a boost factor of almost 1.15 which is not enough for most applications) [6, 7]. Therefore, a conventional dc/ac inverters in general, cannot both step-down and step-up the voltage freely. As mentioned above, the MPP voltage of a PV module is not constant and needs to be tracked by the PV harvesting system. This voltage can be higher/lower than the grid voltage based to the environmental conditions, necessitating a power conversion system that can step up/down the voltage freely to track the MPP accurately. Hence,

the dc/dc stage in the conventional systems is used to step up/down the dc link voltage freely when necessary.

Recently a new converter topology, denoted as the impedance-source converter, is developed by the researchers that undermines the limitations with the conventional VSIs and CSIs [8-10]. These new converters provide several advantages for a variety of applications with different input-output requirements (dc/dc, dc/ac, ac/dc, ac/ac) [11-15]. In particular, a class of dc/ac inverters designed based on the concept of impedance-source conversion, denoted as Z-Source Inverter (ZSI), can step up/down the voltage freely, and thus is very well suited for designing single-stage PV harvesting systems. Moreover, the ZSIs feature several additional advantages over the conventional inverters that makes them even more appealing for energy harvesting systems [16]. Fig. 2 demonstrates a single-stage PV harvesting system built around a ZSI.

B. *Maximum Power Point Tracking Techniques*

Fast convergence, small power ripple at MPP, and accurate and robust tracking of MPP are the key desired properties of a MPPT technique. Several algorithms, architectures, and mechanisms for tracking the MPP of a PV module have been proposed in the literature in the past two decades. Some of the very well-known MPPT methods include: hill-climbing algorithm [17], power-matching scheme [18-20], curve-fitting technique [21, 22], P&O algorithm [23-27], incremental conductance algorithm [28-31], and fractional open-circuit voltage (V_{oc}) control [32]. Additionally, plenty other effective MPPT methods with less popularity are proposed in the literature as well: fractional short-circuit current (I_{sc}) control [33], array reconfiguration method [34], linear current control [35], fuzzy control [36], neural network technique [37], dc-link capacitor droop control [38], pilot cells method [39], current sweep technique [40], and limit-cycle control [41].

The P&O algorithm is one of the most popular MPPT methods due to its simplicity and reliance on engineering intuition for tracking the MPP. The P&O algorithm can be implemented in two fashions: (a) Searching for the MPP while checking the sign of the differential coefficient of the power (P), with respect to the current (I), according to the P−I characteristic curve of the PV module (dP/dI method) [42, 43], or (b) Searching for the MPP while checking the sign of the differential coefficient of the power (P), with respect to the voltage (V), according to the P−V characteristic curve of the PV module (dP/dV method) [44]. The P&O method tracks the MPP by repeatedly updating the operating voltage of the PV array through varying the duty cycle of the interfacing power converter with a fixed step size.

In this work, the idea behind the P&O algorithm is used as grounds to develop a new model predictive based MPPT technique that features better energy harvesting efficacy for a wide range of solar irradiance levels and can more effectively hedge against dynamic environmental conditions that affect the MPP of the PV modules.

C. *Model Predictive Control of Power Converters*

The recent improvements in speed and reliability of real-time digital processing devices has given rise to an ever-increasing interest to devising fast and reliable digital control schemes for control of power electronic converters. Power electronic converters are nonlinear systems with finite number of switching devices that need to be controlled according to stringent operational goals and constraints. Controlling power electronic converters with the aforementioned characteristics demands for elaborate control schemes. As such, the MPC technique has been emerging lately as a promising new control strategy for control of power electronic systems [45-47]. The MPC based techniques feature simplicity and flexibility, and can be programmed to compensate for the inherent non-linearities associated with power electronic converters.

Comparing to classical control schemes, MPC techniques deliver a fast dynamic response with a high stability margin, making them well suited for MPPT of PV systems operating under dynamic environmental conditions. Predictive controllers eliminate the need for a cascaded structure commonly found in classical MPPT systems that employ linear controllers, thus, offering a much faster transient response. This property is observed for the proposed MPPT scheme and verified by providing comparative experimental results. Additionally, predictive control techniques are coincident with the demands of present day control platforms such as discrete-time implementation and knowledge-based modeling.

The MPC techniques use the discrete-time model of the system to evaluate the predicted value of system states and use the predictions to determine an optimal switching schedule for the future steps that will minimize a pre-defined cost function. Designing an MPC scheme for a power electronic converter involves the following steps [46] :

- Identifying all possible switching configurations of the converter and deriving the discrete-time model of the converter for each configuration. The derived models allow for prediction of future values of system states such as output voltage or current.
- Defining a cost function that upon minimization leads to the desired behavior of the system.

Developing the model and cost function, the MPC algorithm should,

- Predict the behavior of the system states for all possible switching configurations.
- Evaluate the cost function for each possible switching configuration.
- Select the switching configuration for the next step that minimizes the cost function.

D. *Model Predictive Control of Grid-Tied ZSI*

Although very resourceful, the ZSIs operate differently than conventional inverters due to incorporation of energy storage elements in their input port and thus require new and innovative control strategies to boost their performance. The first part of this work presents a new control scheme for a grid-tied ZSI based PV energy harvesting system based on the concept of Model Predictive Control (MPC). The core of the proposed system is a new model predictive based MPPT technique that maximizes the energy harvest performance under dynamic weather conditions. Additionally, the proposed system uses a power injection control system that can freely control the ZSI operation and realize a desirable power factor for operation. The MPC techniques feature simplicity and flexibility, and can be programmed to compensate for the inherent non-linearities associated with power electronic converters. Comparing to classical control schemes, MPC techniques deliver a fast dynamic response with a high stability margin, making them well suited for MPPT of PV systems operating under dynamic environmental conditions.

A few research works have been recently published focusing on the MPPT for grid-tied PV system by MPC [48-51]. The work presented by Shadmand et al [48, 51] uses a conventional Perturb and Observe (P&O) algorithm for identification of MPP. This P&O algorithm generates reference points for the inductor current of the PV side Flyback converter. Then a MPC algorithm is used to regulate the actual inductor current to the generated reference points. As a result, in that work the MPC method is not directly involved in MPPT procedure. However, in the approach presented in this paper, the MPC method is used directly to predict the power generated by the PV panel, subsequent to possible changes to the PV voltage. Accordingly, in this paper, the decisions

on the trajectory of the PV voltage are directly made by a MPC algorithm. This provides advantages to the MPPT process over the conventional methods.

The work presented by Mo et al. [49, 50] uses a conventional incremental conductance MPPT algorithm with an internal MPC loop for controlling the inverter. Similar to the work by Shadmand et al., this work does not use MPC for direct identification of the MPP, rather, it uses the incremental conductance method for generation of voltage references for the PV module to regulate its voltage to the voltage at MPP. The MPC method then uses these voltage references to control the inverter switching states such that the input voltage to the Z-source circuit would converge to the provided references. As a result, similar to what mentioned above, the proposed method in this paper is very different than approach taken by Mo et al. by directly identifying the MPPT using MPC calculations.

Other differences between the proposed method in this paper and the mentioned papers is that our method uses a fixed switching frequency and an adaptive voltage step. The voltage step change (ΔV) in our paper at each sampling time is an adaptively predicted value that can change according to the proximity to the MPP by using the predicted model of the system. This will improve the tracking response due to changes in solar irradiance level and minimizes the oscillation around the MPP. Thus, the proposed MPPT technique features high control effectiveness, fast dynamic response, and small oscillations around MPP without requiring expensive sensing devices to measure the solar irradiance level directly. Due to nature of MPC which predicts the system behavior in a specified time horizon, the most significant advantage of the proposed technique is high accuracy tracking of gradually changing solar irradiance levels, a property absent in most well-known MPPT techniques such as P&O. Moreover, due to small oscillations around MPP, the proposed technique makes it possible to use a ZSI with small inductors/capacitors for the PV

harvesting system. This is especially important because according to [52], one of the challenges of employing impedance source inverters such as ZSIs is the large size of the passive elements in the impedance network. Consequently, by using the proposed method, the foot print of a ZSI converter can be reduced significantly. Although the proposed method can be used in conjunction with other converters, its benefits will signify when used with a ZSI.

On the other hand, use of traditional linear control methods for grid tied PV systems using ZSIs appears to be challenging since many cascaded loops are required [53-56]. This is due to the fact that the passive components' voltages and currents at the PV side (dc side) should be controlled to achieve MPP operation simultaneous with the control of variables on the grid side (ac side). However the proposed MPC method achieves the high performance MPP operation while keeping the design very simple through tackling a single cost function subject to minimization. This is another reason that signifies the advantages of the proposed model predictive based MPPT for ZSIs.

E. *Dual-mode Operation of ZSI: Grid-connected and Islanded Modes of Operation*

The second part of this work focuses on MPC of dual-mode ZSI with capability to operate in islanded and grid-connected mode. Conventional power systems are made-up of large central power plants that supply the loads through the transmission and distribution system. However, due to the recent increasing interest in exploiting renewable energy resources, the Distributed Generation (DG) facilities that are interfaced directly to the Distribution Network (DN) are becoming more ubiquitous. PV generation systems are one of the most widely adopted DG facilities that are frequently connected to DN. The existing DN was not initially built with a concern for high level DG integration, thus the recent trend is leading to degraded DN system performance, safety, and reliability. Some of the well-known concerns pertaining to integration of

more DG into the grid are the power quality issues, islanding operation mode, protection issues, and increased fault currents [57-60].

Islanding refers to the condition in which a portion of the grid (e.g. a microgrid) becomes temporarily isolated from the main grid but remains energized by its own DG resources [61]. Islanding may occur accidentally or deliberately. Commonly during the grid-connected operation, the DG systems are not responsible for frequency or voltage regulation, rather, they only inject power to the grid. However, when a microgrid is cut off from the main grid at the Point of Common Coupling (PCC), each renewable electricity generator has to detect the islanding situation [62, 63], and attempt to regulate the frequency and voltage of the microgrid. Sudden reconnection of an islanded microgrid to the grid after a period of islanded operation can have detrimental effects on DN operation because of the differences between the microgrid's and main grid's frequency, phase, and amplitude of the voltages. Therefore, sophisticated power electronic interface circuitry and advanced control schemes are required for DG inverters to ensure a smooth transition from/to the islanding condition.

There are many works in the literature that look at the islanding operation of microgrids and the effects on the main grid. In this regard, Pedersen et al. have provided several mathematical approaches for islanding analysis of a wind farms based on measured voltage [64]. Ropp et al. proposed an islanding detection method using phase criteria and non-detection zones for photovoltaic applications [65]. Woyte et al. investigated the safety issues concerning the grid-connected photovoltaic inverters in case of un-intentional islanding [66]. Bloemink et al. proposed a robust control strategy for multi-sourced microgrid with islanding capability [67]. Eghtedarpour et al. investigated control strategy for hybrid ac/dc microgrids for islanding operation [68]. Other researchers have also proposed several protection strategies, supervisory controllers, and

architectures to enhance the islanding operation and smooth reconnection of microgrids with DG [69-75].

The focus of this part of the work is to propose a reliable and efficient control strategy for a dual-mode operation ZSI for PV applications. The main features of the proposed system are: single loop multi-objective predictive controller with hybrid cost function and adaptive weight factors, robust operation under distorted grid voltage, decoupled active and reactive power control in grid-connected mode, seamless transition between islanded and grid-connected modes of operation, voltage regulation in islanded mode, and reactive power compensation at PCC as an ancillary service from the DG system to the grid.

The transition between grid-connected and islanded operating modes may result in voltage spikes across the local loads, at PCC, leading to injection of inrush currents into the grid due to mismatch between frequency, phase, or amplitude of the voltages. Although several control methods have been proposed in the literature for dual-mode operating inverters with seamless transfer characteristics [76-79], most of these methods use multiple-loop cascaded controllers which are difficult to tune and implement, and may not have reliable operation under abnormalities in the grid such as distorted grid voltage. This work uses the MPC to develop a new control strategy for dual-mode ZSIs with the capability to seamlessly transit between grid-connected and islanded modes of operation. The proposed methodology is solving only a single optimization problem for all operation modes. This feature simplifies the controller algorithm compared to linear multi-loop classic controllers for dual-mode operation inverters. This advantage is particularly more important for impedance source inverters which requires advance modulation scheme due to existence of shoot-through state in addition to active and null states.

F. Ancillary Services of Grid-tied Photovoltaic Systems

Power systems are commonly made-up of large central power plants that feed power to the transmission and distribution systems to supply the loads. However, due to the recent increasing interest in exploiting renewable energy resources, the DG facilities that are interfaced directly to the Distribution Network (DN) are becoming ubiquitous. PV generation systems are one of the most widely adopted DG facilities that are frequently connected to DN. The existing DN was not initially built with a concern for high level DG integration, thus the recent trend is leading to degraded DN system performance, safety, and reliability. Some of the well-known concerns pertaining to integration of more DG into the DN are the power quality issues, frequency stability, islanding operation mode, voltage stability, protection issues and increased fault currents [80-85]. Therefore, several grid codes and standards have been issued to regulate DG systems integration with the DN [86-89].

The future PV connected to DN should be able to provide wide range of ancillary services due to grid mandates and codes [90]. Thus, the PV inverters should be able to operate in different modes of operation under grid fault such as intentional islanding [91, 92] and low voltage ride through (LVRT) mode with reactive power compensation capability [93-95]. In addition to these ancillary services, highly reliable and efficient PEI for PV systems are required to harvest maximum available power from PV panels. Therefore, an efficient and reliable PEI for PV sources in DG systems requires a single stage power conversion with robust control strategy considering the grid status to meet the grid codes and standards.

A few research works have been recently published focusing on the LVRT operation for two stage and single stage grid-tied PV systems using classical multi-loop controllers [93, 94, 96]. As mentioned earlier, the two-stage power conversion suffers from low efficiency and limited

dynamic response [97, 98]. The single stage power conversion also suffers from inability to freely step down/up the voltage, because they are either voltage source or current source inverters [97, 99]. In addition, LVRT operation appears to be challenging since many additional cascaded loops required for traditional control scheme of PV systems [94, 96]. In addition, the use of multi-loop controller causes slow dynamic response under harsh PV ambient condition or/and abnormal grid condition.

As mentioned earlier, the ZSIs' operation and modulation is different than conventional inverters due to the existence of impedance network at their input port. Also, the required LVRT operation will add additional control complexity in comparison to conventional control strategies for ZSIs. MPC [100] is a suitable solution for ZSIs with different modes of operation and multi-objective control functionality. Comparing to classical control schemes, MPC techniques deliver fast dynamic response with high stability marking, making them well suited for PV systems [101] in harsh ambient condition and abnormal grid condition. This dissertation also proposes a single stage smart PV system for grid interaction based on ZSI and MPC framework with capability to operate in LVRT mode. The main features of the proposed smart PEI are: a) High efficiency and reliable operation due to a single power conversion stage, b) Maximum Power Point (MPP) operation under normal grid condition, c) Reactive power compensation, d) LVRT operation under grid faults such as voltage sag with reactive power compensation capability to meet the grid codes and standards, e) Simple control architecture without requirement of many cascaded loops as in classical linear control methods for ZSIs, f) Fast dynamic response under harsh PV ambient condition and grid abnormalities, g) Seamless transition between MPPT and LVRT modes of operation.

II. MODEL PREDICTIVE BASED MPPT FOR GRID-TIED ZSI

A. Overview

Due to inclusion of the shoot-through states, controlling ZSIs requires innovative modulation strategies. Several novel modulation strategies based on Pulse Width Modulation (PWM) method, have been proposed for ZSIs in the literature lately [6, 102] . Three notable modulation strategies for ZSIs are simple-boost [8], maximum-boost [103], and constant-boost [104] techniques. The maximum-boost strategy is usually used for applications with high inverter output frequency [103], while the constant-boost technique is more suitable for applications where independent control of shoot-through is not required [105]. Due to requirement of independent control of shoot-through duty ratio for MPPT in the proposed system and the low grid side frequency, in this work, the simple boost strategy is chosen for generating the switching signals for the ZSI of Fig. 3.

The simple boost modulation technique defines an upper and a lower threshold in addition to the sinusoidal modulating signals for generating the shoot-through states. The thresholds are always equal or greater than the amplitude of the three-phase sinusoidal reference signals. The inverter goes into the shoot-through state (shown in Fig. 4(a)), only when the carrier signal is larger than the upper threshold or smaller than the lower threshold. When the carrier signal is between the two thresholds, this modulation strategy operates similar to a traditional carrier based PWM [106]. The voltage gain of ZSI of Fig. 3 operating with this modulation strategy is given by [8],

$$G = MB = \frac{V_{ac}}{V_0 / 2} = \frac{M}{2M - 1} \tag{1}$$

where M is the modulation index, B is the boosting factor of the impedance-network, V_{ac} is the amplitude of the output voltage of the inverter (equivalent to grid peak phase voltage when grid-tied), and V_0 is the dc-link voltage. The boosting factor B is given by [105],

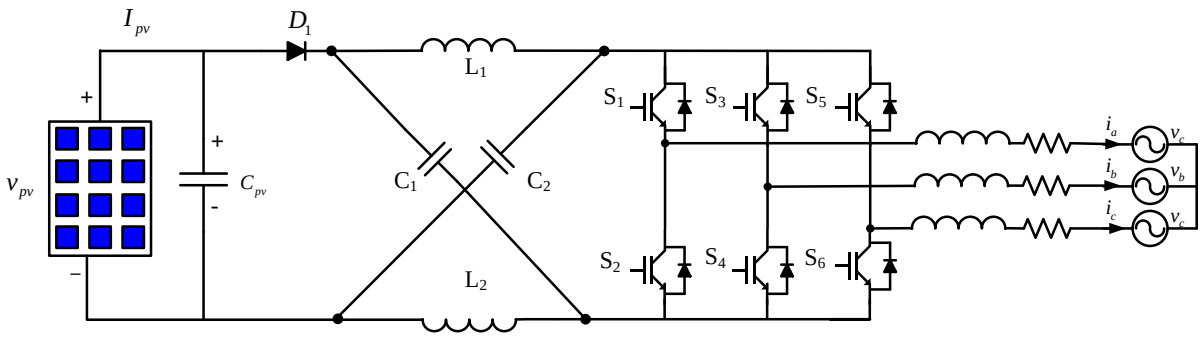

Fig. 3. The three phase grid tied ZSI based PV harvesting converter.

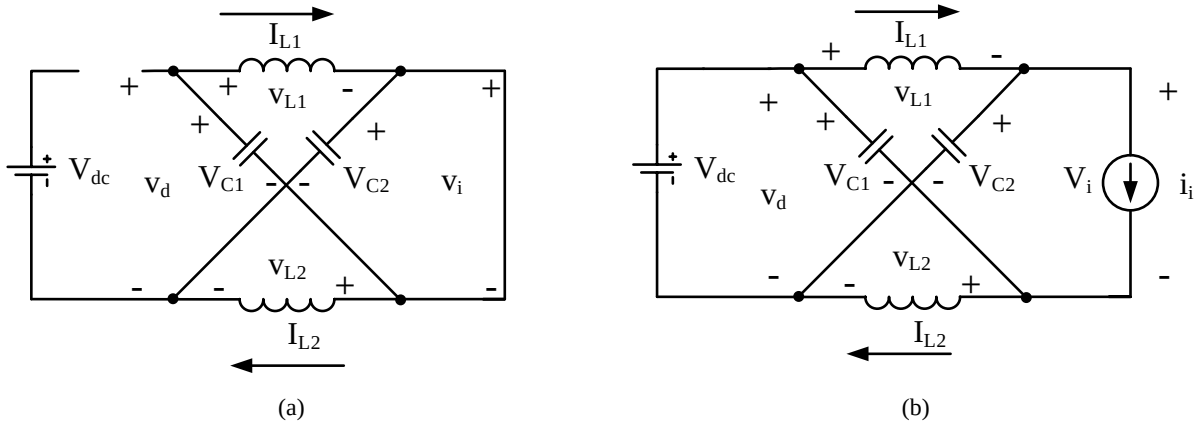

Fig. 4. The equivalent circuit of the impedance network of the ZSI of Fig. 3 during (a) a shoot-through mode, and (b) a non-shoot-through mode.

$$B = \frac{1}{1-2D} \tag{2}$$

where D is the shoot through duty ratio. The voltage stress on the inverter switches is given by [103],

$$V_s = BV_0 = (2G-1)V_0 \tag{3}$$

The grid-tied ZSI and the block diagram of the proposed MPPT system for this converter are illustrated in Fig. 5. The overall control system is comprised of two parts: the PV side model predictive based MPPT and the grid side ZSI power injection control.

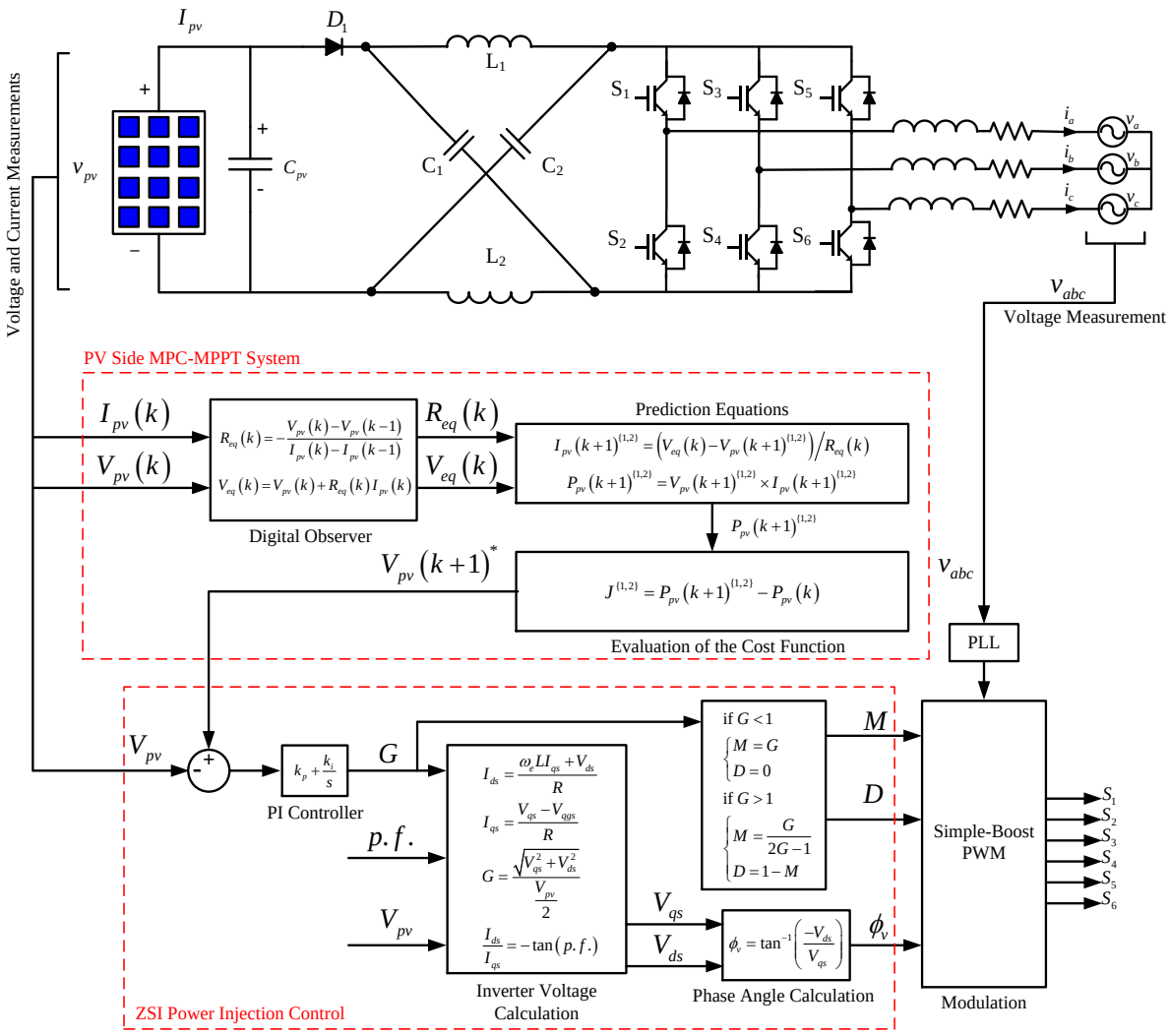

Fig. 5. The grid-tied ZSI and the block diagram of the proposed control system.

B. PV Side Model Predictive Based MPPT

The proposed model predictive based MPPT algorithm tracks the MPP of the PV module by shifting the PV voltage to the voltage at MPP through the following steps,

Step 1 – At any given sample time *k* (referred to as the "current sample time" hereinafter) during the operation, the ZSI can be commanded to either increase or decrease the PV voltage $V_{pv}(k)$. As a result, there are two possible values for the future PV voltage $V_{pv}(k+1)$ at sample time $k+1$

(referred to as "next sample time" hereinafter). In the first step, the algorithm calculates the two possible future PV voltage values,

$$\begin{aligned} V_{pv}(k+1)^1 &= V_{pv}(k) + \Delta V \\ V_{pv}(k+1)^2 &= V_{pv}(k) - \Delta V \end{aligned} \tag{4}$$

where ΔV is a voltage step which is an adaptively predicted value that can change according to the proximity to the MPP. In this work, the following update law for ΔV is proposed,

$$\Delta V = \left| \tilde{V}_{pv}^{ave}(k+1) - V_{pv}(k) \right| \tag{5}$$

Where $\tilde{V}_{pv}^{ave}(k+1)$ is the predicted average PV voltage for the next sample time $(k+1)$. The procedure of finding $\tilde{V}_{pv}^{ave}(k+1)$ is explained at the end of this section.

Step 2 – In this step the algorithm calculates (predicts) the power that would be drawn from the PV module if the PV voltage where to shift to either of the two possible values of $V_{pv}(k+1)^1$ or $V_{pv}(k+1)^2$, in the next sample time. To predict the generated power, the algorithm requires the knowledge of the local P-V characteristic of the module around the operating point of $V_{pv}(k)$. In this work a digital observer is designed to generate the required knowledge for the predictions. The digital observer models the PV module with the Thevenin circuit of Fig. 6. The elements of this circuit, the equivalent voltage (V_{eq}) and equivalent resistance (R_{eq}) of the module, are functions of the P-V characteristic of the PV module and subject to local estimation by the digital observer. The employed estimator equations are,

$$\begin{aligned} R_{eq}(k) &= -\frac{V_{pv}(k) - V_{pv}(k-1)}{I_{pv}(k) - I_{pv}(k-1)} \\ V_{eq}(k) &= V_{pv}(k) + R_{eq}(k) I_{pv}(k) \end{aligned} \tag{6}$$

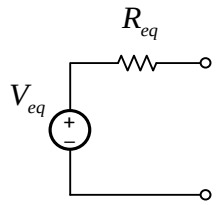

Fig. 6. The equivalent circuit model of the PV module.

Where $V_{pv}(k-1)$ and $I_{pv}(k-1)$ are the values of the PV module voltage and current from the previous sampling time. Estimating the equivalent resistance and voltage of the PV module, the two possible values for the generated power in the next sampling time can be easily predicted from,

$$P_{pv}(k+1)^1 = V_{pv}(k+1)^1 \times I_{pv}(k+1)^1 \tag{7}$$

where,

$$I_{pv}(k+1)^1 = \frac{V_{eq}(k) - V_{pv}(k+1)^1}{R_{eq}(k)} \tag{8}$$

and,

$$P_{pv}(k+1)^2 = V_{pv}(k+1)^2 \times I_{pv}(k+1)^2 \tag{9}$$

where,

$$I_{pv}(k+1)^2 = \frac{V_{eq}(k) - V_{pv}(k+1)^2}{R_{eq}(k)} \tag{10}$$

Step 3 – In this step the predicted power for the two cases will be used to evaluate the following cost function,

$$J^{\{1,2\}} = P_{pv}(k+1)^{\{1,2\}} - P_{pv}(k) \tag{11}$$

To increase the generated power in each step, the predicted power, $P_{pv}(k+1)^1$ or $P_{pv}(k+1)^2$, that will result in a larger value of *J* from (11), will be selected as the desirable trajectory for the next

step. For instance, if $J^1 > J^2$, then the algorithm chooses to generate $P_{pv}(k+1)^1$ in the next sampling time, which correspondingly means the PV voltage will need to be shifted to $V_{pv}(k+1)^1$ by proper adjustment of the inverter gain. The desirable value of the PV voltage for the next step is denoted as $V_{pv}(k+1)^*$ hereinafter. In order to regulate the PV voltage to $V_{pv}(k+1)^*$, the inverter gain needs to be adjusted. The ZSI power injection control system described in the next section is responsible for accomplishing this task.

Procedure of finding $\tilde{V}_{pv}^{ave}(k+1)$ – In order to find the predicted average PV voltage for the next sample time, the discretized average value model of the ZSI needs to be developed. The discretized equations for the ZSI in a shoot through and a non-shoot-through state can be used to develop the average value model. The discretized equations for a non-shoot through state are found in the literature as [55, 107],

$$\begin{cases} I_{L1}(k+1) = I_{L1}(k) + \dfrac{T_S}{L_1}(V_{pv} - V_{C1}(k) - R_{L1}I_{L1}(k)) \\ V_{C1}(k+1) = V_{C1}(k) + \dfrac{T_S}{C_1}(I_{L1}(k+1) - I_{inv}(k+1)) \end{cases} \tag{12}$$

where T_S is the sampling time and,

$$I_{inv}(k+1) = S_1 \times I_a(k) + S_2 \times I_b(k) + S_3 \times I_c(k) \tag{13}$$

The discretized equations for the shoot through state are found similarly from [55, 107],

$$\begin{cases} I_{L1}(k+1) = I_{L1}(k) + \dfrac{T_S}{L_1}(V_{C1}(k) - R_{L1}I_{L1}(k)) \\ V_{C1}(k+1) = V_{C1}(k) - \dfrac{T_S}{C_1}I_{L1}(k+1) \end{cases} \tag{14}$$

The $V_{C1}(k+1)$ is assumed to be approximately equal to $V_{C1}(k)$ since the change is minor for sufficiently small sampling time T_S [55, 107]. The average current going through the C_{pv} and C_1

should be zero, thus the I_{PV} is the same as the ZSI inductor current I_{L_1}. Therefore the predicted average PV current can be formulated using (12) and (14) as,

$$\begin{aligned}\tilde{I}_{pv}^{ave}(k+1) = &\left[I_{L1}(k) + \frac{T_S}{L_1}(V_{pv} - V_{C1}(k) - R_{L1}I_{L1}(k)) \right] \times \left(1 - D(k)\right) \\ &+ \left[I_{L1}(k) + \frac{T_S}{L_1}(V_{C1}(k) - R_{L1}I_{L1}(k)) \right] \times D(k)\end{aligned} \tag{15}$$

Considering that the relationship between the PV voltage and V_{C1} can be described as [53],

$$V_{pv} = \frac{2}{B+1} V_{C1} \tag{16}$$

the average PV voltage can be predicted using (12), (14), (16) as,

$$\tilde{V}_{pv}^{ave}(k+1) = \frac{2}{B+1} \left\{ \begin{array}{l} \left[V_{C1}(k) + \frac{T_S}{C_1}(I_{L1}(k+1) - I_{inv}(k+1)) \right] \times \left(1 - D(k)\right) + \\ \left[V_{C1}(k) - \frac{T_S}{C_1} I_{L1}(k+1) \right] \times D(k) \end{array} \right\} \tag{17}$$

where *B* is the boosting factor.

C. ZSI Power Injection Control Scheme

This part of the control system has three goals: regulating the PV voltage to $V_{pv}\left(k+1\right)^*$ provided by the PV side MPPT system by properly adjusting the inverter gain, controlling the ratio of active/reactive power injected to the grid (power factor control) according to the specific application requirements, and minimizing the voltage stress on the switches. The proposed control system accomplishes the three mentioned goals by generating *M*, *D*, and the phase angle of the inverter voltages ϕ_v. The generated values will be used by the simple-boost modulator to produce proper switching signals for controlling the inverter.

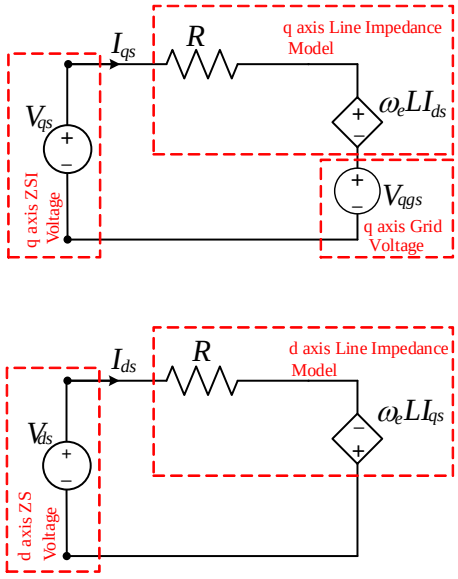

Fig. 7. The q-d model of the grid tied ZSI system.

As pictured in Fig. 5 the proposed system uses a Proportional-Integral (PI) controller to regulate the PV voltage to $V_{pv}(k+1)^*$ by adjusting the inverter gain. Therefore, the output of the PI controller in Fig. 5 is the inverter gain. The inverter gain generated by the PI controller can be used along with the desired power factor of the operation to calculate the phase angle of the inverter voltages ϕ_v. To calculate ϕ_v the inverter system needs to be analyzed in a rotational q-d reference frame. The equivalent circuits of the grid-tied ZSI system in the steady-state condition in a q-d reference frame synchronized with the grid voltage is shown in Fig. 7 [108]. According to this figure, the q and d axis inverter currents, I_{qs} and I_{ds}, can be formulated as,

$$I_{ds} = \frac{\omega_e LI_{qs} + V_{ds}}{R}$$
$$I_{qs} = \frac{V_{qs} - \omega_e LI_{qs} - V_{qgs}}{R} \quad (18)$$

Where $\omega_e, L, R, V_{ds}, V_{qs}, V_{qgs}$ respectively represent, the grid angular frequency, line inductances, line resistances, the d axis inverter voltage, the q axis inverter voltage, and the q axis grid voltage. Additionally by substituting,

$$V_{ac} = \sqrt{V_{qs}^2 + V_{ds}^2} \tag{19}$$

in (1), the following equation between the inverter voltages and the inverter gain is found,

$$G = \frac{\sqrt{V_{qs}^2 + V_{ds}^2}}{\frac{V_{pv}}{2}} \tag{20}$$

Moreover, the desired power factor (p.f.) can be associated with the inverter currents by the following equation,

$$\frac{I_{ds}}{I_{qs}} = -\tan\left(p.f.\right) \tag{21}$$

Knowing the inverter gain and the power factor, (18), (19), (20), and (21) can be solved to find the inverter q and d axis voltages, V_{qs} and V_{ds}. Finally, by knowing V_{qs} and V_{ds}, the phase angle of the inverter voltages can be calculated from,

$$\phi_v = \tan^{-1}\left(\frac{-V_{ds}}{V_{qs}}\right) \tag{22}$$

The values of *M* and *D* are generated by the voltage stress minimization block in Fig. 5. Using simple boost control, any inverter gain for a ZSI can be realized using infinite combinations of modulation indices and shoot-through duty ratios. However, inverter gains can be realized using a unique combination of *M* and *D* that will result in the minimum voltage stress on the switches [8, 103, 104]. This combination can be found from,

$$\begin{cases} M = G \\ D = 0 \end{cases} \tag{23}$$

for inverter gains less than or equal to one, and from,

$$\begin{cases} M = \dfrac{G}{2G-1} \\ D = 1 - M \end{cases} \tag{24}$$

for the inverter gains more than one.

D. Results and Discussion

The proposed controller is implemented in MATLAB/Simulink and experimentally validated. A SUNTECH270S-24-Vb PV module with I-V and P-V characteristics shown in Fig. 8 is used as the source of energy for the system. The system parameters are given in **Error! Reference source ot found.**. A unity power factor is targeted for the entire operation. The performance of the proposed model predictive based MPPT is evaluated by looking into three important merit criteria: the response to a step change in the solar irradiance level, operation in the event of gradually changing solar irradiance (aka clouds moving in sky), and operation in steady-state to evaluate the oscillation around MPP.

TABLE I: System Parameters

Parameter	Value
C1	1000 µF
C2	1000 µF
L1	0.7 mH
L2	0.7 mH
Sampling time	60 µs
Cpv	470 µF
Lgrid	1 mH

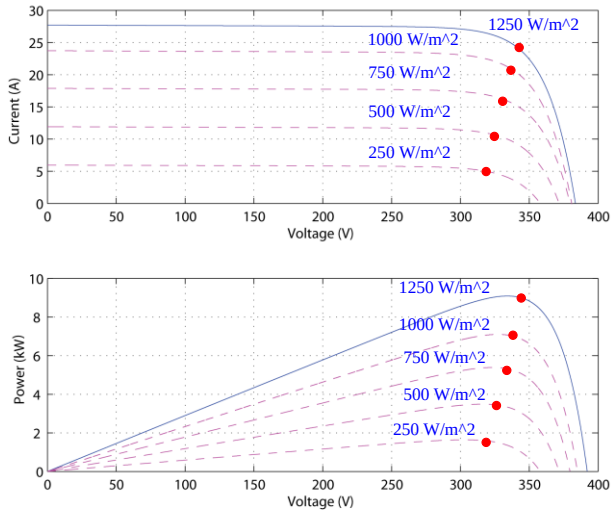

Fig. 8. The P-V and I-V characteristic curves of the employed PV module for experimental verification.

To begin the analysis, the operation of the system in steady-state with solar irradiance of 1250 W/m^2 is explored. The PV side and grid side voltages and currents are shown in the scope shots of Figs. 9 and 10. As pictured in Fig. 9, the PV side waveforms have negligible ripple of less than 2% and the ZSI input voltage is a pulsating high frequency waveform with constant peak at steady state. The grid side current and voltage waveforms verify the targeted unity power factor requirement and the calculated Total Harmonic Distortion (THD) of 2.32% from these waveforms is within the IEEE-519 standards for grid-tied systems [109].

In the first experiment the solar irradiance level is stepped down from 1250 W/m^2 to 750 W/m^2 to analyze the dynamic response of the proposed MPPT system. The expected I_{pv} and V_{pv} from the I-V characteristics of the PV modules are respectively 24.5 A and 345 V at 1250 W/m^2 and 17 A and 323 V at 750 W/m^2. Fig. 11 illustrates the response of the PV voltage and current to this step change. The results demonstrate fast and accurate dynamic tracking performance with convergence time of less than 10 ms for the proposed model predictive MPPT. The actual measured values of the I_{pv} and V_{pv} are 24 A and 342 V at 1250 W/m^2 and 16. 7 A and 319 V at 750 W/m^2, indicating good agreement between the experimental results and the expected

outcomes. To analyze the level of voltage and current oscillations around MPP, the waveforms of Fig. 11 are shown in a larger scale (zoomed in) in Fig. 12. According to this figure the oscillations around MPP are negligible at steady-state. The grid side current and voltage of phase 'a' for this experiment are illustrated in Fig. 13. As pictured, the grid side voltage and current are completely in phase (unity power factor) with fast dynamic response to the step change in solar irradiance level. The individual harmonic components of the grid current are listed in TABLE II, and its fast-fourier-transform (FFT) spectrum analysis is illustrated in Fig. 15.

In the second scenario, to evaluate the system performance under more realistic dynamic environmental conditions, a gradually changing solar irradiance test is performed. For this experiment, the solar irradiance was gradually decreased at a rate of 0.85 W/m^2/ms from 1250 W/m^2 to 750 W/m^2 in course of 600 ms. The PV voltage, ZSI input voltage, and PV current waveforms for this experiment are shown in Fig. 14. As pictured, the PV voltage and current are gradually tracking MPP with high accuracy. According to Fig. 14, the ZSI input voltage V_{in}, is a high frequency pulsed waveform with a constant peak value when the solar irradiance is constant and a slightly decaying peak value when the solar irradiance gradually decreases.

The control efficacy of the proposed model predictive MPPT is calculated for several solar irradiance levels (from low to high) experimentally and compared to the conventional P&O method (presented in TABLE III). To calculate the control efficacy, the actual captured power at the PV side for each solar irradiance level is measured and divided by the maximum available power at MPP determined from the P-V curves of the utilized PV module shown in Fig. 8. According to TABLE III, for low to high solar irradiance level, the proposed technique has smaller oscillation (ΔP_{PV}) around MPP and more power capture, thus resulting to MPPT efficacy of more than 99% for all scenarios. Although the P&O exhibits relatively good performance at high solar

irradiance levels but the performance degrades significantly for medium to low solar irradiance levels.

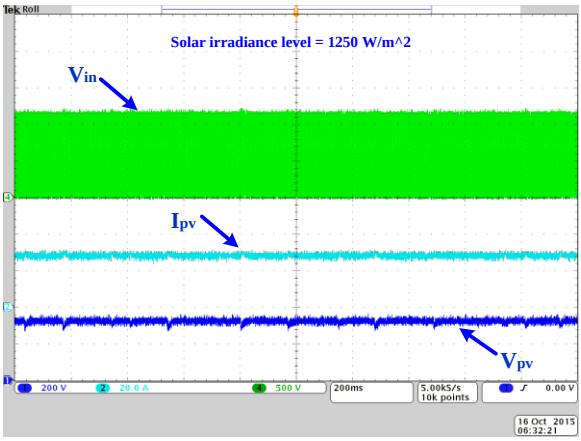

Fig. 9. The PV side voltage and current and the ZSI input voltage in steady-state for solar irradiance level of 1250 W/m2.

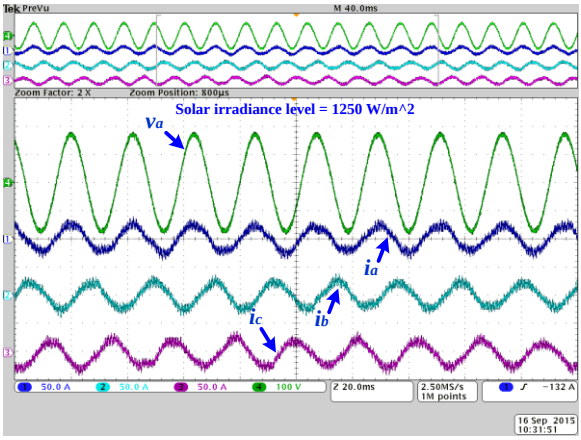

Fig. 10. The three phase grid side currents and phase 'a' voltage in steady-state for solar irradiance level of 1250 W/m2.

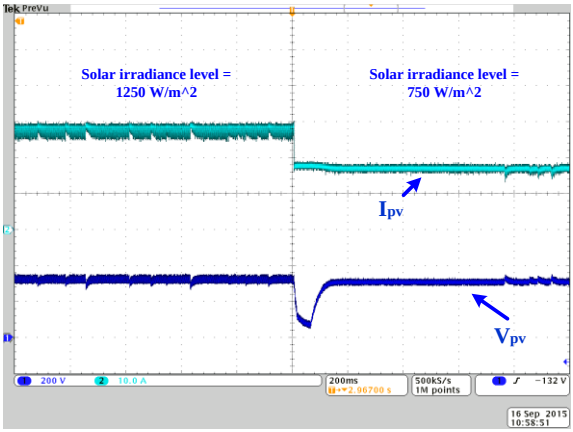

Fig. 11. The response of the PV voltage and current to a step change in solar irradiance

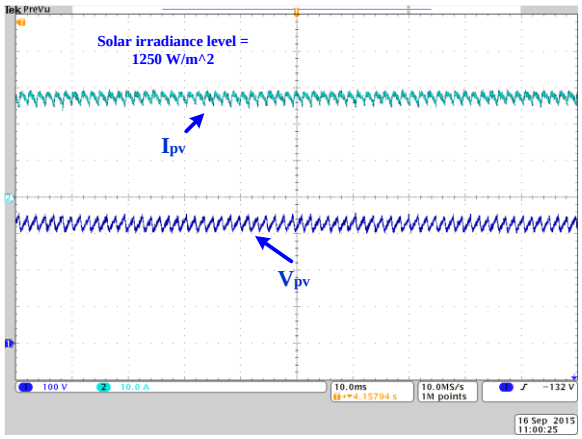

Fig. 12. PV voltage and current ripple at MPP.

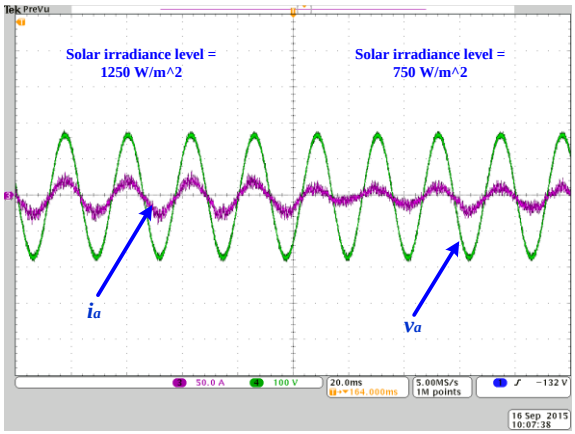

Fig. 13. The grid side voltage and current of phase ‘a’ in case of a step change in the solar irradiance level

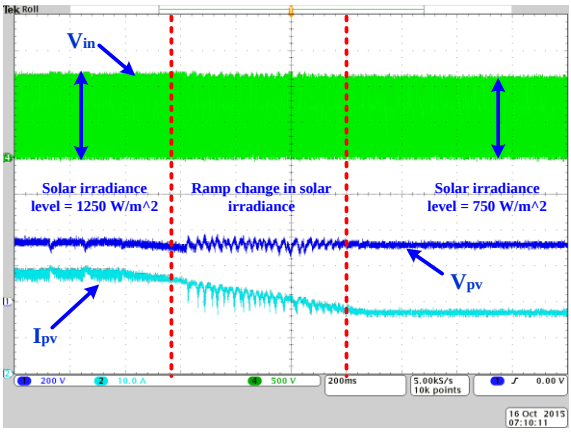

Fig. 14. The PV voltage, the ZSI input voltage, and PV current when solar irradiance is gradually decreased from 1250 W/m^2 to 750 W/m^2

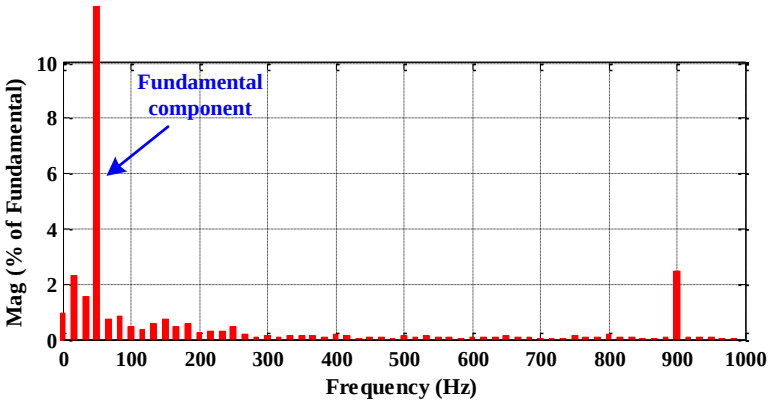

Fig. 15. The FFT spectrum analysis of the phase 'a' of the grid side current.

TABLE II: Harmonics distortion of grid-side current

Harmonics Order	Distortion (%)
3rd	0.7%
5th	0.37%
7th	0.18%
9th	0.13%
11th	0.12%
13th	0.05%
15th	0.06%
17th	0.01%

TABLE III: The efficacy comparison for the proposed MPC based MPPT VS. P&O method

Solar Irradiance Level	Conventional P&O method		Proposed model predictive MPPT	
	ΔP_{PV} (%)	Efficacy (%)	ΔP_{PV} (%)	Efficacy (%)
1250	4.21%	98.58%	1.52%	99.03%
1000	4.14%	98.24%	2.47%	99.24%
750	3.94%	98.12%	1.77%	99.07%
500	3.91%	97.43%	2.3%	99.68%
250	3.56%	95.19%	1.65%	99.58%

The dynamic performance of the proposed model predictive based MPPT is also compared to the well-known P&O MPPT technique for comparative analysis. The results are shown in Figs. 16 and 17. To accurately compare the results side-by-side, the raw data from oscilloscope for the conventional P&O and the proposed method are exported to MATLAB and plotted on the same time axis. As pictured, the proposed technique exhibits better response to a 1250 W/m^2 to 750 W/m^2 step change in solar irradiance level both in terms of convergence time and low oscillations around MPP. According to Figs. 16 and 17, the convergence time of the P&O technique is 35 ms

while the convergence time of the proposed technique is only 10 ms. Moreover, the proposed model predictive based MPPT has significantly lower oscillations around MPP comparing to the P&O technique thus eliminating the need of large passive elements in the impedance network.

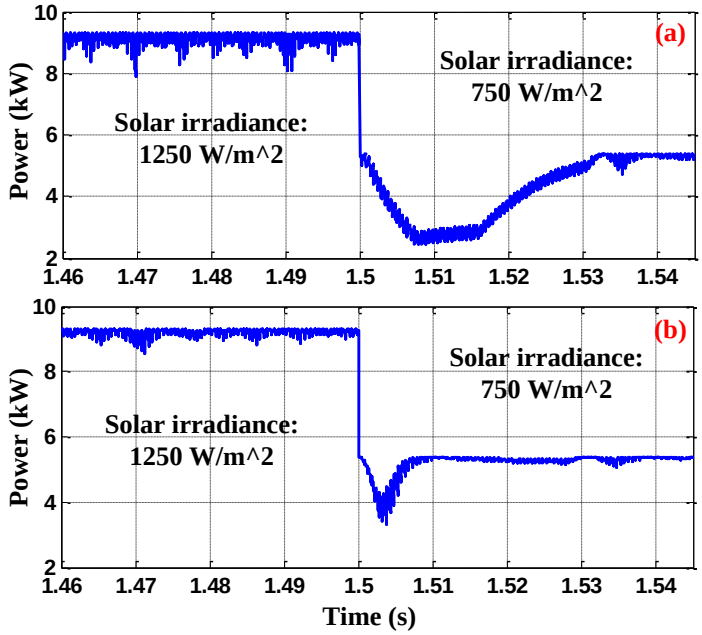

Fig. 16. The PV side response to a 1250 W/m2 to 750 W/m2 step change in solar irradiance (a) conventional P&O technique (b) proposed model predictive MPPT

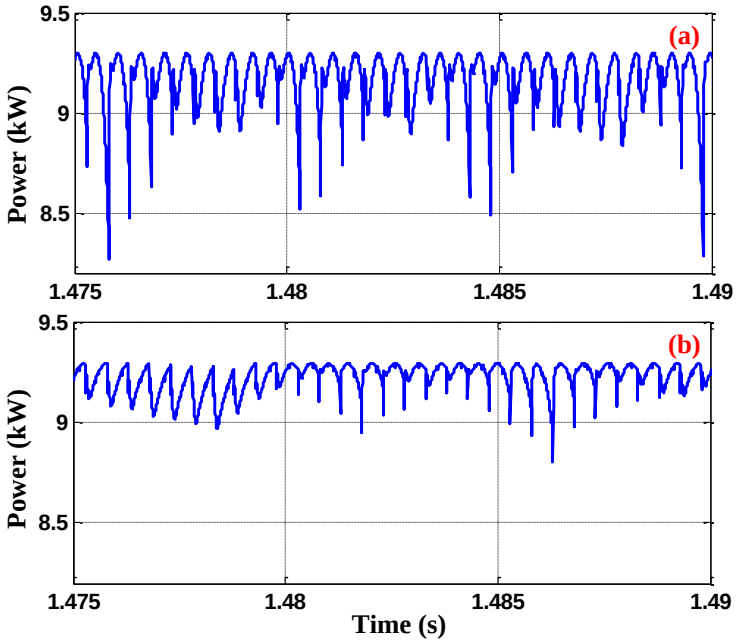

Fig. 17. The PV side power oscillation around the MPP at steady-state for solar irradiance level of 1250 W/m2 (a) conventional P&O technique (b) proposed model predictive MPPT

One of the main drawbacks of the model predictive control is the effect of model parameters error on the controller performance. In this paper, the robustness and performance of the proposed model predictive MPPT is analyzed for ±40% error in the impedance network model at the PV side of the system, the control efficacy at solar irradiance level of 1000 W/m^2 is calculated and plotted in Fig. 18 for up to ±40% error in the L_1 as well as C_1 where 0% error is the nominal inductor and capacitor values (Table I). In Fig. 18, the error in the models are assumed to be not simultaneously. As it is depicted in Fig. 18, the MPPT efficacy with 0% error is 99.24% and for the worst case scenarios (+40% or –40% error in the models of C_1 and L_1), the proposed MPPT efficacy is more than 97.5% which still has acceptable performance. It is also interesting to see the MPPT efficacy when multiple errors in the model are happening simultaneously. For this scenario, the errors in the C_1 and L_1 are assumed to be happened at the same time, thus the worst case scenario is when there ±40% error in the models of C_1 and L_1 at the same time. The MPPT efficacies for this analysis at solar irradiance level of 1000 W/m^2 are depicted in Fig. 19. As it is shown in this figure, even for the worst case scenario the controller has acceptable efficacy of 94%.

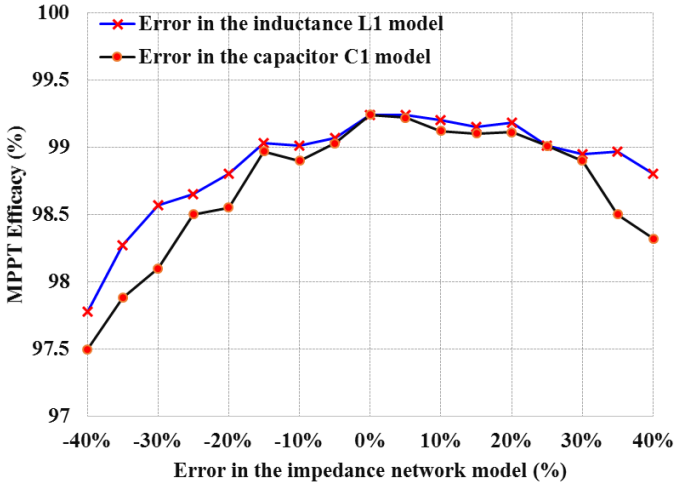

Fig. 18. Effect of the impedance network model error on the MPPT efficacy of the proposed system.

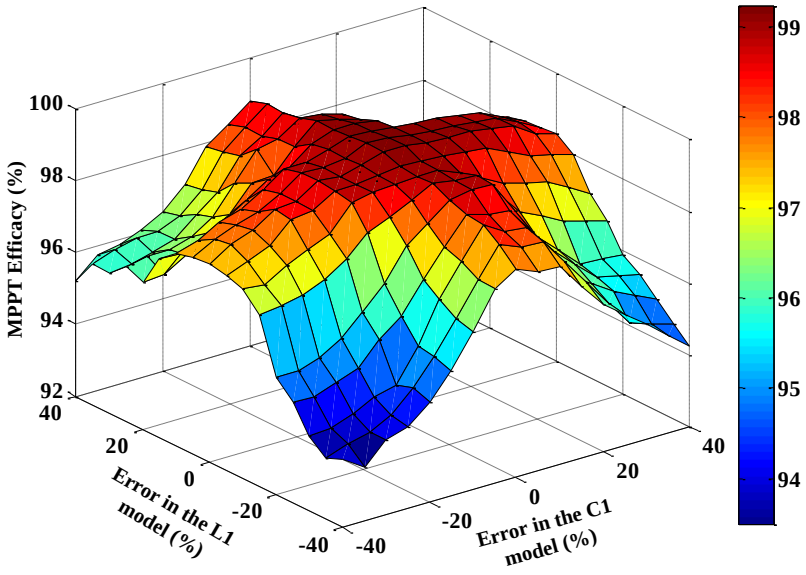

Fig. 19. Effect of the error in the impedance network elements C1 and L1 model simultaneously on the MPPT efficacy of the proposed system.

E. Conclusion

This section of disseration presents a highly efficient control scheme for a ZSI based grid-tied PV system. The presented control system has two components: The proposed model predictive based MPPT, and the grid side power injection controller. The model predictive based MPPT is proposed for tracking the MPP of the PV module. The proposed technique predicts the future values of the PV voltages and currents using a digital observer that estimates the values of the equivalent voltage and resistance of the PV module at any operating point. The perturbation size in PV voltage is adaptively predicted to determine the desirable trajectory PV voltage for the developed cost function, thus high control effectiveness is achieved from low to high solar irradiance level. The power injection control system uses the reference values generated by the MPPT system to control operation of the ZSI system while keeping the voltage stress on the converter switches at the lowest possible value. The experimental results demonstrate low THD of the grid side current that is within the IEEE 519 standards, fast dynamic response to a step

change in solar irradiance level, and negligible oscillations around MPP under dynamically changing sky condition.

III. Model Predictive Controlled ZSI with Dual Mode Operations Capability: Grid-connected and Islanded Modes

A. System Description

Fig. 20 demonstrates a single-stage PV DG system built around a ZSI. The modes of operation of the system can be classified to two steady-state modes and two transition modes. The steady-state modes are the grid-connected and islanded modes. The transition modes are transition from the grid-connected mode to the islanded mode and vice versa. The state diagram for transition between the four modes of operation of system is illustrated in Fig. 21. As pictured, a decoupled active and reactive power controller that can freely adjust the power factor of the ZSI is proposed for the grid-connected mode. In the islanded mode the required local load voltage is regulated by the same controller but with different terms in the proposed MPC cost function. In both steady-state modes, the voltage and current of the impedance network are controlled to adjust the ZSI gain by operating in the shoot-through and non-shoot-through states, for applications such as the Maximum Power Point Tracking (MPPT) for the PV source. For transition modes, a grid-synchronization and phase adjustment algorithm is proposed to seamlessly transit from the grid-connected mode to the islanded mode and vice versa. Based on the application, the reference

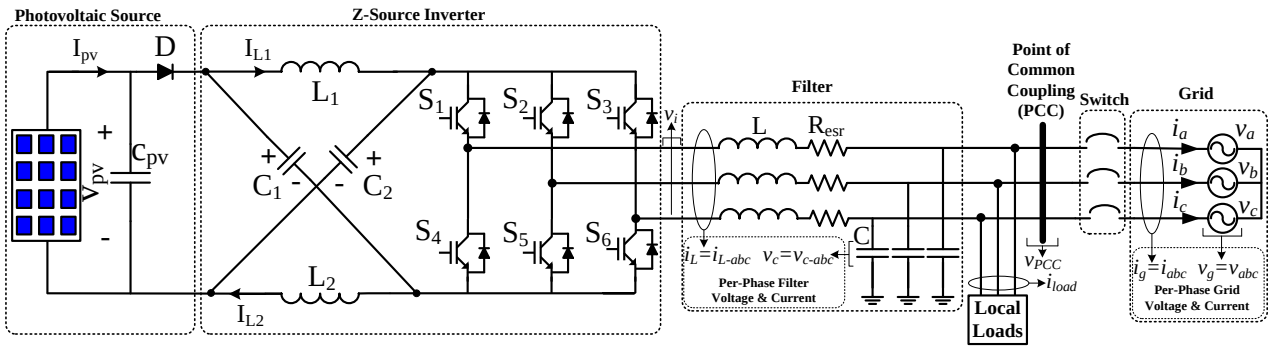

Fig. 20. Dual-mode Z-Source inverter.

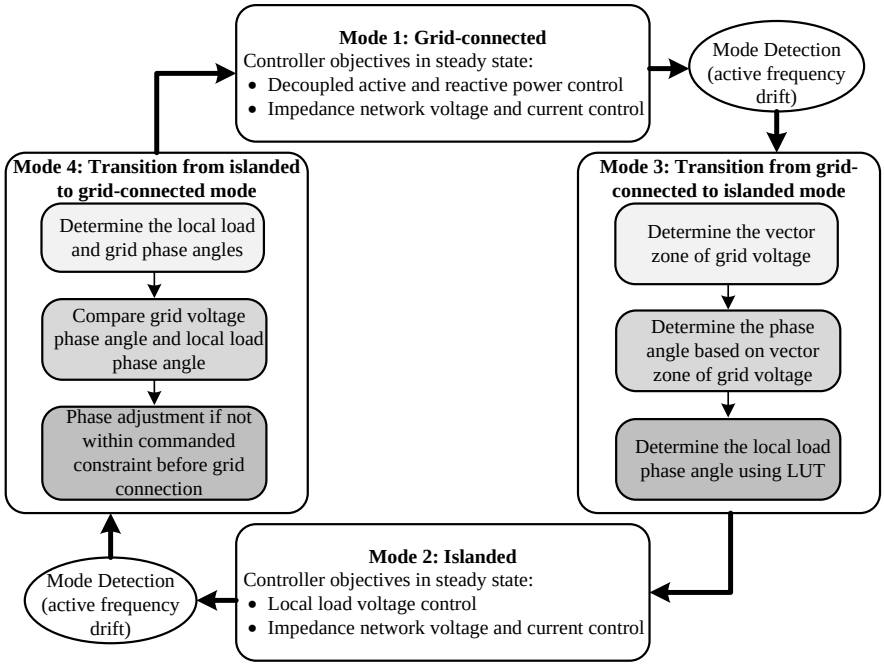

Fig. 21. Modes of operation of the proposed Z-source inverter

signals for the MPC cost function is generated. For example, for the PV application, the reference active power is determined from the MPPT algorithm and the dc-link voltage control [110].

In this section, the derivation of the predictive model of the system will be discussed. In the stationary reference frame, the per-phase output filter dynamic model of the ZSI is given by the output filter inductor current and capacitor voltage,

$$\frac{d}{dt} i_L(t) = \frac{1}{L}(v_i(t) - v_{PCC}(t) - i_L(t)R_{esr}) \tag{25}$$

$$\frac{d}{dt} v_C(t) = \frac{d}{dt} v_{PCC}(t) = \frac{1}{C}(i_L(t) - i_{Load}(t)) \tag{26}$$

where i_L (t) is the filter inductor current, v_i (t) is the output voltage before the filter, v_{PCC} (t) is the voltage at the PCC, L is the grid side inductance of the filter, and R_{esr} is the equivalent series resistance of the inductor. Using the Euler forward method, (25) and (26) can be approximated using,

$$\frac{dx(t)}{dt} \approx \frac{\tilde{x}(k+1) - x(k)}{T_S} \tag{27}$$

where T_s is the sampling period and k is discretized t. The predicted inductor current $\tilde{i}_L(k+1)$ and capacitor voltage $\tilde{v}_C(k+1)$ can be found from (25)-(27) as,

$$\tilde{i}_L(k+1) = \frac{T_s}{L}(v_i(k) - v_{PCC}(k) - i_L(k)R_{esr}) + i_L(k) \tag{28}$$

$$\tilde{v}_C(k+1) = \frac{T_s}{C} i_C(k+1) + v_C(k) \tag{29}$$

Moreover, the grid side voltage (v_g) can be predicted at time (k+1) using,

$$\tilde{v}_g(k+1) = v_g(k)e^{j\omega T_S} \tag{30}$$

where ωT_s is the amount of change in angle of the grid side voltage over one sampling interval T_s , for a grid voltage with angular frequency of ω. If the sampling interval is sufficiently small, it can be approximated that $\tilde{v}_g(k+1) \approx v_g(k)$. Additionally, from (26) and the Euler forward approximation, the predicted value of the per-phase local load current in islanded mode can be formulated by,

$$\tilde{i}_{Load}(k+1) = i_L(k+1) - \frac{C}{T_s}(v_c(k+1) - v_c(k)) \tag{31}$$

At the PV side, the discretized equations for a non-shoot-through state are found by (12)-(14).

B. Grid Connected and Islanded Modes

In the grid connected mode, the proposed controller for the ZSI behaves as a current regulator by injecting power to the grid. The controller objectives in this mode of operation are decoupled active and reactive power control as well as the voltage and current control for the impedance network elements. The dual-mode operation ZSI system can operate with adjustable power factor, enabled by the proposed decoupled power control.

Most of the robust grid synchronization techniques available in the literature require multiple cascaded control loops that need to be designed and tuned. Commonly, the grid synchronization requires the amplitude and phase angle information of the grid voltage detected by the phase-locked loop (PLL) [111, 112]. Also, some other synchronization subsystems are usually needed

for conventional grid-connected inverter system including synchronization reference frame (SRF) [81, 113]. These multi-loop cascaded control loop adds design complexity, adverse transient performance, and even system instability [95, 114]. Therefore, second-order generalized integrator (SOGI) which is a simple synchronization algorithm with proved harmonic distortion rejection capability is used in this paper for generation of orthogonal α-β phase components for the ZSI. The characteristic transfer functions of SOGI in S-domain are given by [115],

$$\frac{x_\alpha(s)}{x(s)} = \frac{\chi\omega s}{s^2 + \chi\omega s + \omega^2} \tag{32}$$

$$\frac{x_\beta(s)}{x(s)} = \frac{\chi\omega^2}{s^2 + \chi\omega s + \omega^2} \tag{33}$$

where χ is the damping factor and ω is the fundamental frequency. The SOGI can filter the harmonics that are far from the fundamental frequency. The SOGI can effectively extract the fundamental component from signals with all harmonic components.

In order to determine the predictive active and reactive power model for MPC, by using the SOGI, the orthogonal α-β phase components of PCC voltage v_{PCC} and current i_L are generated and given by,

$$\begin{aligned} v_{PCC-\alpha} &= V_m \sin(\omega t) \\ v_{PCC-\beta} &= -V_m \cos(\omega t) \end{aligned} \tag{34}$$

$$\begin{aligned} i_{L-\alpha} &= I_m \sin(\omega t - \phi) \\ i_{L-\beta} &= -I_m \cos(\omega t - \phi) \end{aligned} \tag{35}$$

Accordingly, the active and reactive power in α-β can be formulated as [116],

$$x = \begin{bmatrix} P \\ Q \end{bmatrix} = \frac{3}{2} \begin{bmatrix} v_{PCC-\alpha} & v_{PCC-\beta} \\ v_{PCC-\beta} & -v_{PCC-\alpha} \end{bmatrix} \begin{bmatrix} i_{L-\alpha} \\ i_{L-\beta} \end{bmatrix} \tag{36}$$

Then, the derivative of active and reactive power with respect to time can be found as,

$$\begin{bmatrix} \frac{dP}{dt} \\ \frac{dQ}{dt} \end{bmatrix} = \frac{3}{2}\begin{bmatrix} \frac{dv_{PCC-\alpha}}{dt} & \frac{dv_{PCC-\beta}}{dt} \\ \frac{dv_{PCC-\beta}}{dt} & -\frac{dv_{PCC-\alpha}}{dt} \end{bmatrix}\begin{bmatrix} i_{L-\alpha} \\ i_{L-\beta} \end{bmatrix} + \frac{3}{2}\begin{bmatrix} v_{PCC-\alpha} & v_{PCC-\beta} \\ v_{PCC-\beta} & -v_{PCC-\alpha} \end{bmatrix}\begin{bmatrix} \frac{di_{L-\alpha}}{dt} \\ \frac{di_{L-\beta}}{dt} \end{bmatrix} \tag{37}$$

while the derivative of PCC voltages $v_{PCC\text{-}\alpha}$ and $v_{PCC\text{-}\beta}$ with respect to time can be found as,

$$\begin{aligned} \frac{dv_{PCC-\alpha}}{dt} &= -\omega \times v_{PCC-\beta} \\ \frac{dv_{PCC-\beta}}{dt} &= \omega \times v_{PCC-\alpha} \end{aligned} \tag{38}$$

The state-space model of the system with respect to active and reactive power can then be found from (36)-(38) and (25) as,

$$\frac{dx}{dt} = Ax + Bv_i - Ev_{PCC} \tag{39}$$

where

$$\begin{aligned} x &= \begin{bmatrix} P & Q \end{bmatrix}^T, \; B = \frac{3}{2L}\begin{bmatrix} v_{PCC-\alpha} & v_{PCC-\beta} \\ v_{PCC-\beta} & -v_{PCC-\alpha} \end{bmatrix}, \\ A &= \begin{bmatrix} -\frac{R_{esr}}{L} & -\omega \\ \omega & -\frac{R_{esr}}{L} \end{bmatrix}, \; E = \frac{3}{2L}\begin{bmatrix} v_{PCC-\alpha} & v_{PCC-\beta} \\ 0 & 0 \end{bmatrix} \end{aligned} \tag{40}$$

Thus the system is presented in state-space format with P and Q as the state variables. In (39) the v_i is the input and v_{PCC} is a measured value. Using the Euler Forward method, the discrete-time model of (39) can be found as,

$$\tilde{x}(k+1) = x(k) + T_s\left(Ax(k) + Bv_i(k) - Ev_{PCC}(k)\right) \tag{41}$$

This equation can be used to formulate the predicted active and reactive power at instant (k+1),

$$\begin{aligned}\tilde{P}(k+1) &= P(k) - \omega T_s Q(k) \\ &+ \frac{3T_s}{2L}\left(V_m^2 - v_{PCC-\alpha}(k)v_{i-\alpha}(k) - v_{PCC-\beta}(k)v_{i-\beta}(k)\right) \\ \tilde{Q}(k+1) &= Q(k) + \omega T_s P(k) \\ &- \frac{3T_s}{2L}\left(v_{PCC-\beta}(k)v_{i-\alpha}(k) - v_{PCC-\alpha}(k)v_{i-\beta}(k)\right)\end{aligned} \tag{42}$$

Thus, two of the control variables (active and reactive power) for grid-connected mode of operation can be predicted measuring the filter inductor current i_L (grid side current in grid-connected mode), the PCC voltage v_{PCC}, and the inverter output voltage v_i, all in two-axis stationary reference frame α-β. The other two control variables, i.e. inductor current (I_{L1}) and capacitor voltage (V_{C1}) on the PV side, are predicted using equations (12) and (14).

In the islanded mode of operation, the ZSI is disconnected from the grid at the PCC. The ZSI will supply the local loads in this mode. The controller objectives are to regulate the voltage across the local loads by using (29) and to control the impedance network current and voltages using (12) and (14).

C. Transition Modes: Grid Synchronization and phase Adjustment

According to the state diagram of Fig. 21, during the two transition modes the proposed grid synchronization and phase adjustment method will be triggered to ensure seamless transition. The block diagram of the proposed grid synchronization and phase adjustment method is illustrated in Fig. 22. The input to the grid synchronization algorithm is the peak grid voltage (V_g) and α component of the grid voltage ($v_{g\text{-}\alpha}$) which is generated using the SOGI module. The low pass filter characteristics of the SOGI modules filter out the grid voltage harmonics to obtain the fundamental component phase information of the grid voltage. The algorithm starts by estimating the grid voltage phase using,

$$\hat{\phi}_g = \sin^{-1}\left(\left|\frac{v_{g-\alpha}(t)}{V_g}\right|\right) \tag{43}$$

Due to symmetry characteristic of the sinusoidal waveform, the phase angle given by (43) can correspond to two different magnitude over one cycle. Thus, an exact phase angle determination is required. A zonal detection approach is used to determine the exact phase angle that corresponding to specific voltage magnitude according to (43). As it is illustrated in Fig. 23, a sinusoidal waveform can be divided into four zones in one cycle. A look-up table with saved values

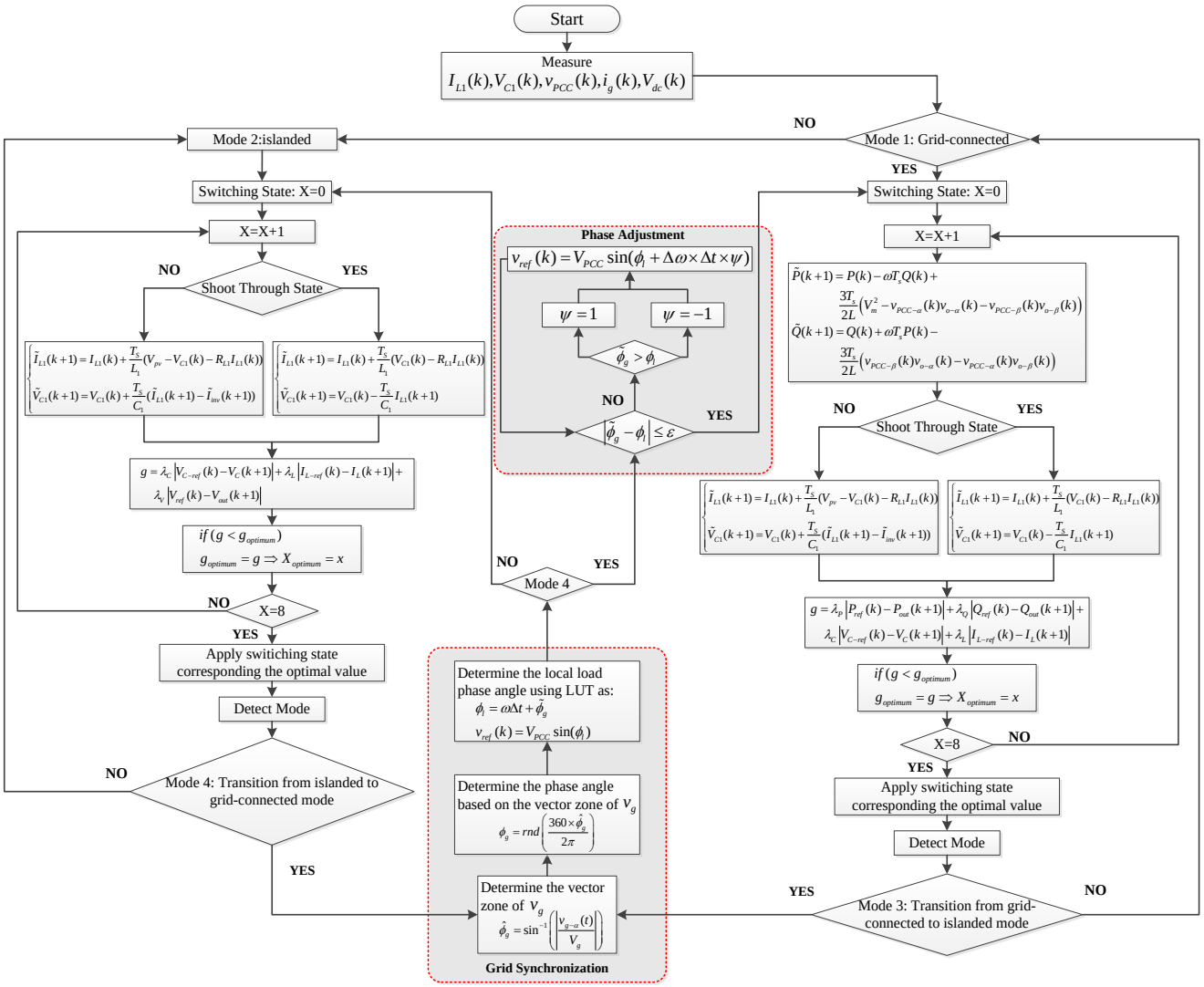

Fig. 22. Proposed model predictive control for z-source inverter dual mode operation: grid-connected and islanded.

of a sine function is used, four zones are identified over a sinusoidal cycle as illustrated in Fig. 23 in order to get the appropriate point in look-up table with the right phase angle information of the grid voltage. The vector zone of grid voltage and as a result the exact phase angle is determined using the $v_g(k)$ and $v_g(k\text{-}1)$ values as follows,

$$\begin{cases} v_g(k) > 0 \,\&\, v_g(k) > v_g(k-1) \Rightarrow zone\ 1 \\ v_g(k) > 0 \,\&\, v_g(k) < v_g(k-1) \Rightarrow zone\ 2 \\ v_g(k) < 0 \,\&\, v_g(k) < v_g(k-1) \Rightarrow zone\ 3 \\ v_g(k) < 0 \,\&\, v_g(k) > v_g(k-1) \Rightarrow zone\ 4 \end{cases} \tag{44}$$

$$\tilde{\phi}_g = \begin{cases} \phi_g & zone\ 1 \\ \dfrac{360}{2} - \phi_g & zone\ 2 \\ \dfrac{360}{2} + \phi_g & zone\ 3 \\ 360 - \phi_g & zone\ 4 \end{cases} \tag{45}$$

where

$$\phi_g = rnd\left(\frac{360 \times \hat{\phi}_g}{2\pi}\right) \tag{46}$$

Once the phase angle is determined according to (44)-(46), the reference voltage for the islanded mode of operation can be determined over the transition period by,

$$\begin{aligned} \phi_l &= \omega \Delta t + \tilde{\phi}_g \\ v_{ref}(k) &= V_{PCC} \sin(\phi_l) \end{aligned} \tag{47}$$

This grid synchronization is required for both transition modes (modes 3 and 4). In mode 4 (transition from islanded to grid-connected mode), a phase adjustment will be triggered after the grid voltage restauration. The phase adjustment algorithm evaluates the phase angle difference between the local load and the grid, if their difference is negligible (smaller than some predefined ε), then the phase angle information will be sent to grid-connected mode control algorithm. If the phase difference is bigger than ε, then a unit increment/decrement in the frequency is carried-out

to adjust the phase difference for seamless transition from islanded mode to grid-connected mode. Thus, the reference voltage is determined as:

$$v_{ref}(k) = V_{PCC}\sin(\phi_l + \Delta\omega \times \Delta t \times \psi) \tag{48}$$

where Ψ is 1 if $\tilde{\phi}_g > \phi_l$ and -1 if $\tilde{\phi}_g < \phi_l$, after each increment/decrement in the phase angle. The phase difference ($\left|\tilde{\phi}_g - \phi_l\right|$) is evaluated until the absolute value of the phase angle difference between the grid voltage and the local load voltage is smaller than ε.

D. Controller Formulation and Algorithm

As mentioned earlier, there are four modes of operation for the proposed controller of dual-mode inverter: two steady-state modes and two transition modes. The objective of two transition modes is to ensure synchronization and seamless transfer. The summary of the controller algorithm is illustrated in Fig. 22. In this paper a single cost function subject to minimization for all modes of operation is developed, the whole optimization problem for the system is formulated as follows,

$$\begin{aligned}
&\min g = \begin{cases} \lambda_P g_P + \lambda_Q g_Q + \lambda_C g_C + \lambda_L g_L & \text{for modes 1,3,4} \\ \lambda'_C g_C + \lambda'_L g_L + \lambda'_V g_V & \text{for mode 2} \end{cases} \\
&\text{subject to} \\
&\tilde{x}(k+1) = x(k) + T_S(Ax(k) + Bu(k)) \\
&g_P = \left|P_{ref}(k) - P_{out}(k+1)\right|, g_Q = \left|Q_{ref}(k) - Q_{out}(k+1)\right| \\
&g_C = \left|V_{C-ref}(k) - V_C(k+1)\right|, g_L = \left|I_{L-ref}(k) - I_L(k+1)\right| \\
&g_V = \left|V_{ref}(k) - V_i(k+1)\right|
\end{aligned} \tag{49}$$

The weight factors $\left(\lambda_P, \lambda_Q, \lambda_C, \lambda_L\right)$ are selected adaptively based on the modes of operation. According to (49), two set of $\left(\lambda_P, \lambda_Q, \lambda_C, \lambda_L\right)$ coefficient are selected: one set for modes 1, 3, 4 and another set for mode 2. The weights factors are determined using branch and bound technique [100], tracking errors of each control objectives and injected grid current THD are used as a tool for selection of weight factors using branch and bound technique.

Assuming the system is operating initially in mode 1, at the end of the control algorithm for mode 1, the mode detection algorithm determines the ZSI mode of operation. If mode 2 is detected, the grid synchronization algorithm will be triggered to determine the reference voltage for local loads to be regulated in mode 2. As it is illustrated in Fig. 22, mode 2 also regulates the C_1 voltage and L_1 current for determination of shoot through and non-shoot through operation. Then the optimization problem of (47) will be executed for mode 2. The voltage vector that minimizes the cost function will be determined and applied to the converter in mode 2. The mode detection algorithm runs again at the end of each loop. If the mode 1 is detected, the grid synchronization and phase adjustment algorithms will be triggered to seamlessly transit to grid-connected mode.

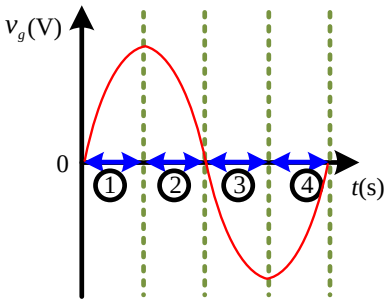

Fig. 23. Zonal representation of grid voltage.

E. Results and Discussion

The proposed controller is implemented in MATLAB/Simulink and experimentally validated using the PLECS RT Box. The proposed system is experimentally tested for several case studies in the grid-connected mode and islanded mode. The performance of the proposed controller is evaluated by looking into four important merit criteria: seamless transition between grid-connected mode and islanded mode, phase adjustment and grid synchronization, seamless transition between grid-connected and islanded mode with different frequencies, decoupled active and reactive power control in grid-connected mode, fast dynamic response of active and reactive power due to change in solar irradiance level or change in reactive power required by the grid at PCC, low tracking error

in steady state operation, and reliable operation under distorted grid voltage in grid-connected mode.

The transitions from grid-connected mode to islanded mode and vice versa are firstly examined. The v_{PCC}, i_L, and i_g waveforms for this transition are shown in the scope shots of Figs. 24 and 25. As pictured in Fig. 24, the dual-mode ZSI is initially connected to the grid and then it is disconnected from the grid. After disconnection from the grid, the grid current i_g goes to zero instantly. The dual-mode ZSI operates in islanded mode after a short period for islanding detection and transition. It can be seen that a seamless transition from grid-connected to islanded mode is achieved without overshoot/undershoot for PCC voltage v_{PCC} and/or inductor current i_L during this transition process. In order to demonstrate the flexibility and reliability of the proposed controller, the local loads in islanded mode are assumed to operate at 180 Hz instead of 60 Hz grid frequency. This case study demonstrate the capability of the proposed system to seamlessly transfer to islanded mode while the local load frequency is different than the grid frequency.

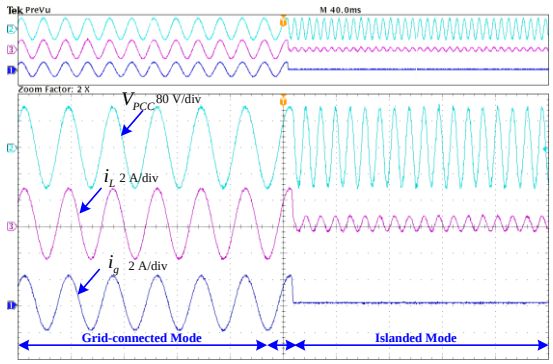

Fig. 24. Seamless transition from grid-connected to islanded mode.

Fig. 25 demonstrates the dual-mode ZSI performance for transition from islanded mode to grid-connected mode. As picture, the ZSI is initially supplying local loads when islanded, then it will go to transition mode when the grid is ready to re-connect and the grid synchronization as well

as phase adjustment algorithms are triggered. Similar to previous case, the transition happened seamlessly without harsh dynamic behavior in v_{PCC}, i_L, and i_g as shown in Fig. 25.

The experimental results of the dual-mode ZSI operation in islanded mode and grid-connected mode are shown in Figs. 26-28. A resistive load of 60 Ω is considered as the local load for islanded operation of the system in Fig. 26, the v_{PCC}, i_L, and i_g waveforms are shown in Fig. 26 for this experiment. As it is pictured, the load voltage is tracking its reference PCC voltage for this case study with peak voltage of 120 V.

Figs. 27 and 28 show the grid-connected mode operation when a step change is applied to active and reactive power references. In Fig. 27, the active and reactive power references are initially 300 W and 0 VAR (unity power factor) respectively, then a step change is applied to the active and reactive power references. The reactive power is changed to 200 VAR and active power is decreased to 200 W. In Fig. 28, the active and reactive power are changed back to 300 W and 0 VAR. As it is shown in Fig. 27 and 28, the grid current overshoot/undershoot is negligible. The active and reactive power tracking errors are less than 0.06%. In order to evaluate the quality of the injected current to the grid, the individual harmonic components of the grid side current, i_g, are tabulated in Table. I, the calculated i_g total harmonic distortion (THD) of 2.48% is within the IEEE-519 standards for grid-tied systems [86].

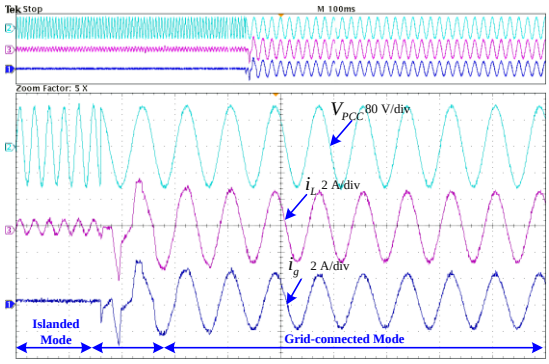

Fig. 25. Seamless transition from islanded mode to grid-connected mode

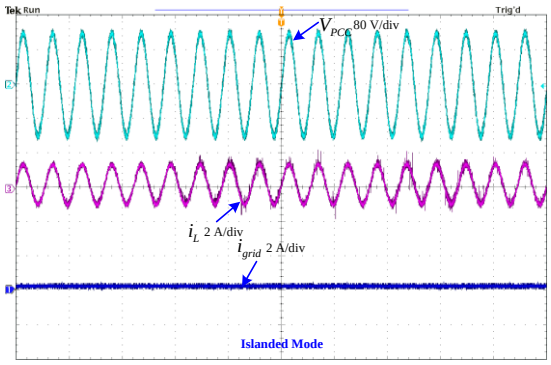

Fig. 26. Islanded mode of operation.

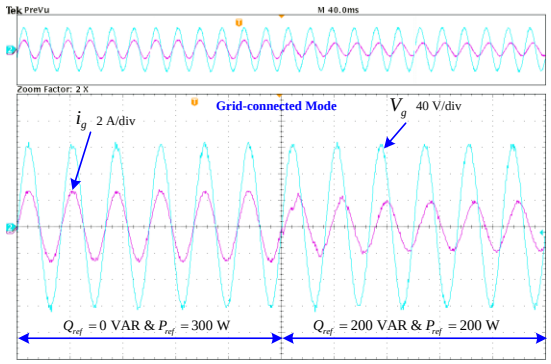

Fig. 27. Grid connected mode: step change in active and reactive reference power, the reactive power changed from 0 to 200 VAR and the active power is changed from 300 to 200 W.

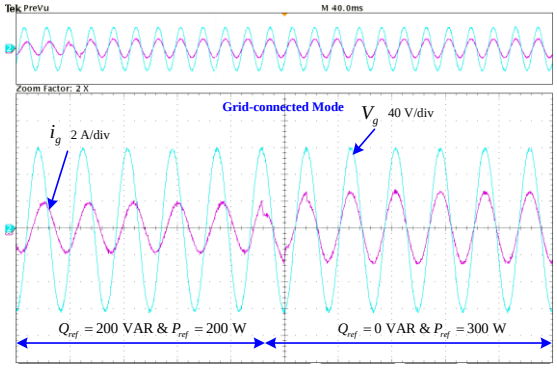

Fig. 28. Grid connected mode: step change in active and reactive reference power, the reactive power changed from 200 to 0 VAR and the active reference power is changed from 200 to 300 W.

Fig. 29 and 30 show the three phase inductor ($i_{L\text{-}abc}$) current during seamless transition for resistive local load of 30 Ω and 60 Ω. As it is pictured, for both cases of local load connected at the PCC to the system, seamless transition is achieved without significant deviation in the current.

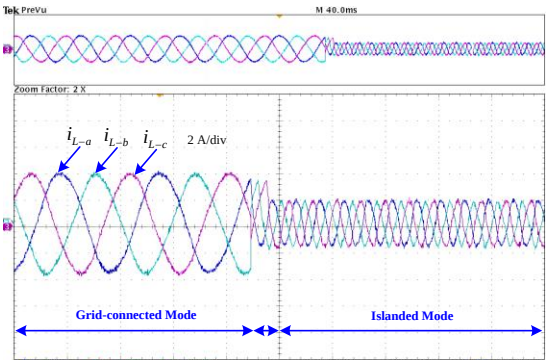

Fig. 29. The waveform of $i_{L\text{-}abc}$ during seamless transition from grid-connected mode to islanded mode for local load of 30 Ω.

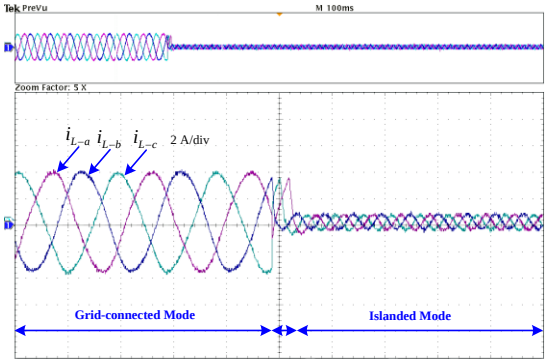

Fig. 30. The waveform of $i_{L\text{-}abc}$ during seamless transition from grid-connected mode to islanded mode for local load of 60 Ω.

TABLE IV:Harmonics distortion of grid-side current

Harmonics Order	Distortion (%)
3rd	0.94%
5th	0.03%
7th	0.54%
9th	0.14%
11th	0.28%
13th	0.22%
15th	0.14%
17th	0.11%

Fig. 31 shows the performance of the proposed controller under distorted grid voltage (v_g) in grid-connected mode. As it is shown in Fig. 31, the grid current is not affected by the distorted grid voltage. The commanded unity power factor operation with high quality current waveform is achieved. Fig. 32 shows the experimental dynamic performance of active and reactive power to

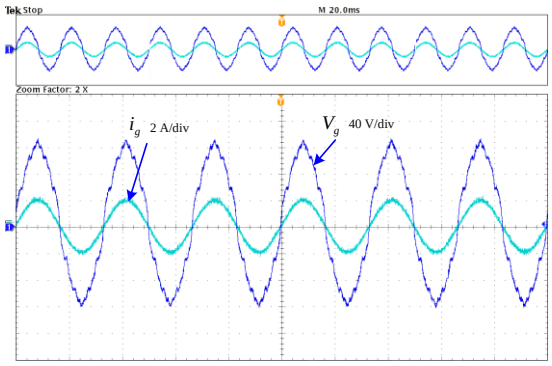

Fig. 31. The waveform of i_g and v_g under distorted grid voltage.

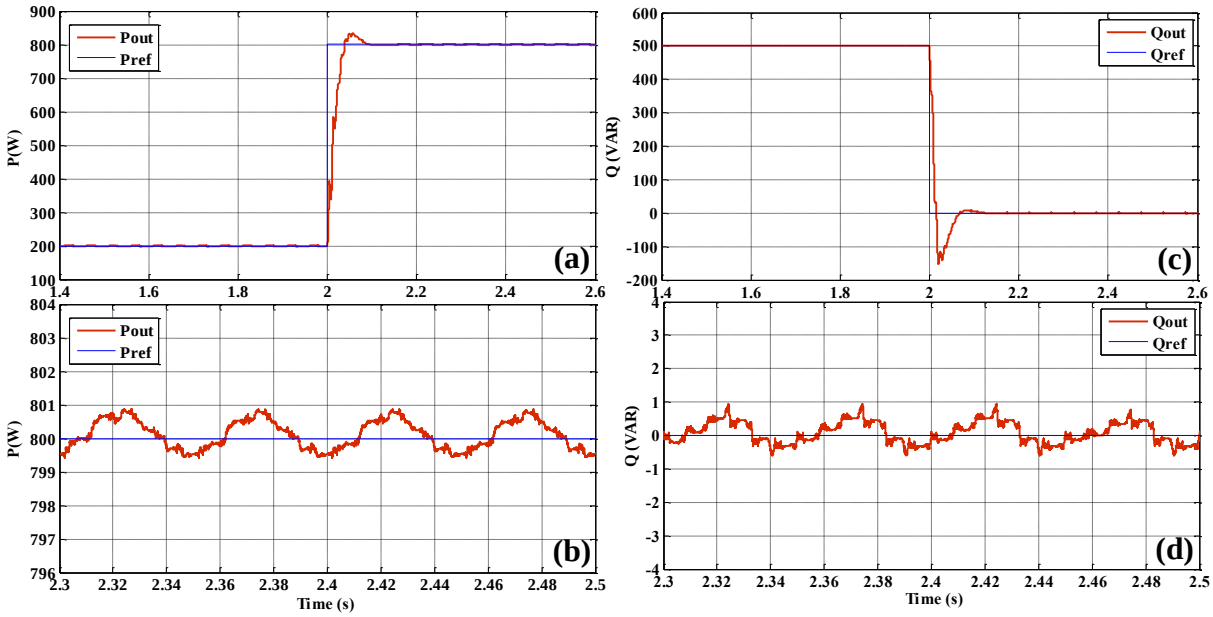

Fig. 32. Experimental results active and reactive power tracking: a) active power tracking response to step change from 200 W to 800 W b) active power steady state tracking error c) reactive power tracking response to step change from 500 VAR to 0 VAR d) reactive power steady state tracking error.

big step change in active and reactive power references. A step change is applied to active power from 200 W to 800 W and in reactive power from 500 VAR to 0 VAR. As it is pictured in Fig. 32, the reference of active and reactive power were initially 200 W and 500 VAR respectively, then at time 2 s, a step change is applied to active and reactive power from 200 W to 800 W and from 500 to 0 VAR respectively. As it is shown, the results demonstrate promising dynamic response for such a big step change also. The steady state operation tracking errors are shown in Fig. 32 (b) and (d), as it is pictured the power ripple are negligible. The active power tracking error is

negligible with active power ripple of less than 0.8 W peak to peak. Similarly, the reactive power is tracked with negligible oscillation and tracking error, for unity power factor reference, the achieved experimental power factor is around 0.99 and the reactive power ripple is less than 0.8 VAR peak to peak. It worth mentioning that, for the proposed multi-objective control system priorities can be given to individual control objectives by adjusting the weight factors in the MPC cost function (49). The active and reactive power tracking performance in Fig. 32 can be adjusted by lowering the tracking accuracy of other control objectives in (49) from their references. Thus an engineering trade-off is applied in this paper to balance the tracking performance between all the control objectives in the single hybrid cost function of (49).

F. Conclusion

This section of the dissertation proposes a MPC technique for a dual-mode ZSI with seamless transition between grid-connection and islanding mode without significant deviation in voltage and current due to mismatch in phase, frequency, and amplitude of grid voltage and load. The proposed single loop controller determines the optimal switching states for the ZSI based on its mode of operation. A single hybrid cost function is developed for all modes of operation which simplifies the design and practical implementation of the proposed model based predictive controller. This characteristic of the proposed system is well suited for the impedance source inverters which require advance and complex modulation scheme due to their shoot-through state in addition to active and null states. The hybrid cost function is optimized during each sampling time to: harvest the maximum power from the PV module, inject the active power to the grid, provide reactive power compensation for the grid as an ancillary service to the grid through PCC, and maintain the PCC voltage in the islanded mode. The explanation of system modes of operation, strategy to transit between modes of operation, and operation in steady state modes are provided.

Several experimental case studies are provided to validate the theoretical expectations. The results demonstrate robust operation in all modes of operation. The main features of the proposed controller are high quality grid current in grid connected mode, fast dynamic response in grid-connected mode to step change in active and reactive power, negligible power ripple in steady state operation, seamless transition between modes of operation without significant deviation in PCC voltage and current, robust operation under distorted grid voltage, and capability to operate at different frequency in islanded mode of operation.

IV. Z- Source Inverter for Photovoltaic Systems with Low Voltage Ride Through Capability

A. System Description

Fig. 33 illustrates the proposed smart PV system by model predictive based control of ZSI with LVRT capability. This section presents the predictive modeling of the PV side impedance network and the grid side filter. The dynamic model of the grid side filter is given by,

$$\frac{d}{dt}i_L(t) = \frac{1}{L}(v_i(t) - v_g(t) - i_L(t)R_{esr}) \tag{50}$$

$$\frac{d}{dt}v_C(t) = \frac{d}{dt}v_g(t) = \frac{1}{C}(i_L(t) - i_g(t)) \tag{51}$$

where i_L (t) is the inductor current, v_i (t) is the output voltage of the inverter, v_g (t) is the ac gridvoltage, L and C are the filter's inductance and capacitance values, and R_{esr} is the equivalent series resistance of the inductor. By applying the Euler forward approximation method to (50) and (51), the discretized model of (50) and (51) are found as:

$$\tilde{i}_L(k+1) = \frac{T_s}{L}(v_i(k) - v_g(k) - i_L(k)R_{esr}) + i_L(k) \tag{52}$$

$$\tilde{v}_C(k+1) = \frac{T_s}{C}(i_L(k) - i_g(k)) + v_C(k) \tag{53}$$

where T_s is the sampling period.

One of the main characteristics of ZSI is its shoot-through mode for flexible boosting of the input (PV) voltage. In this mode, both switches in one leg of the inverter are simultaneously turned ON. The equivalent circuit model of the ZSI in Fig. 33 for shoot-through mode and non-shoot-through modes (active states) are illustrated in Fig. 34 (a) and (b). Using these equivalent circuits and Euler forward approximation, the predictive model of the Z source network can be developed [117]. According to [117], the predictive equations for the inductor L_1 current and capacitor C_1 voltage in a non-shoot-through mode are,

$$\tilde{I}_{L1}(k+1) = I_{L1}(k) + \frac{T_S}{L_1}(V_{pv}(k) - V_{C1}(k) - R_{L1}I_{L1}(k)) \tag{54}$$

$$\tilde{V}_{C1}(k+1) = V_{C1}(k) + \frac{T_S}{C_1}(I_{L1}(k) - I_{inv}(k)) \tag{55}$$

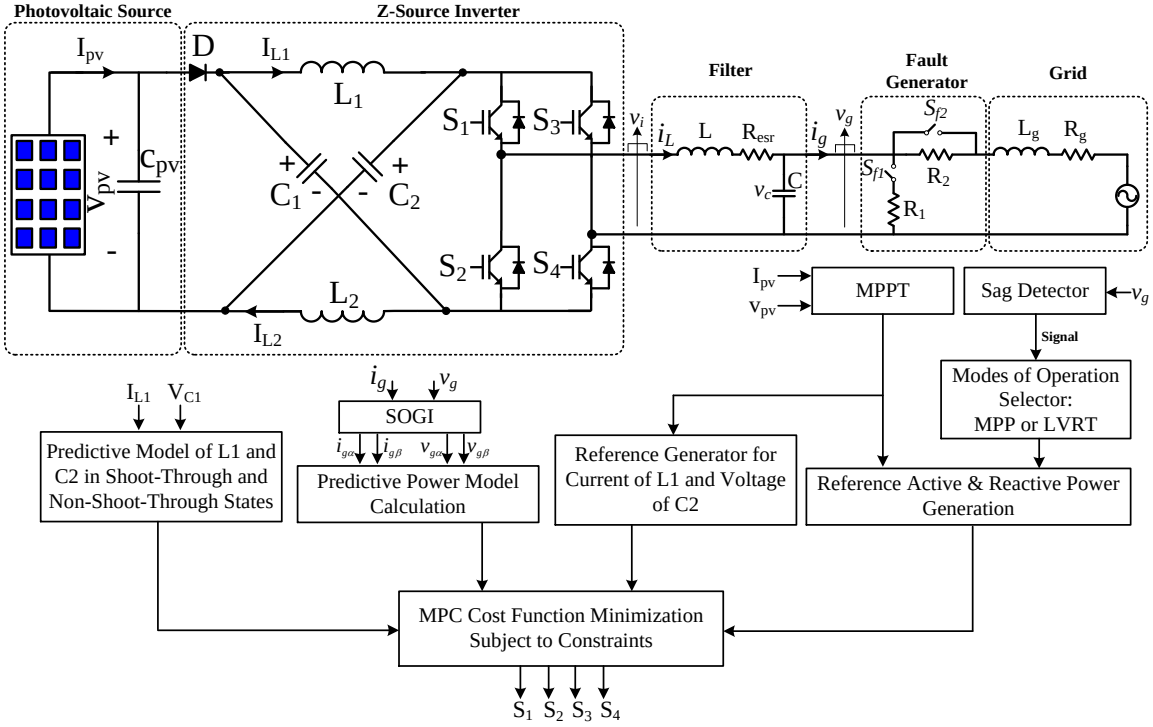

Fig. 33. General schematic of the proposed power electronics interface based on z-source inverter for grid-tied photovoltaic application with low voltage ride through capability.

while the same equations for a shoot-through state are,

$$\tilde{I}_{L1}(k+1) = I_{L1}(k) + \frac{T_S}{L_1}(V_{C1}(k) - R_{L1}I_{L1}(k)) \tag{56}$$

$$\tilde{V}_{C1}(k+1) = V_{C1}(k) - \frac{T_S}{C_1}I_{L1}(k) \tag{57}$$

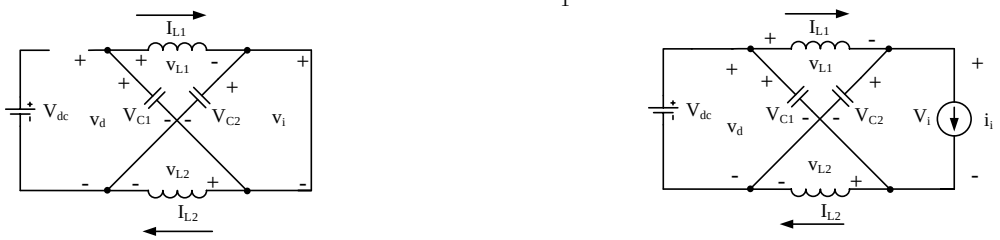

(a) equivalent circuit in shoot-through mode (b) equivalent circuit in non-shoot-through mode

Fig. 34. Equivalent circuit model of the impedance network of ZSI in Fig. 33 during shoot-through and non-shoot-through modes

The second order general integrator (SOGI) [115] is used to determine the in-phase and quadrature component ($\alpha\beta$) of grid voltage and current. The characteristic transfer functions of SOGI in S-domain are given by [115],

$$\frac{x_\alpha(s)}{x(s)} = \frac{\chi\omega s}{s^2 + \chi\omega s + \omega^2} \tag{58}$$

$$\frac{x_\beta(s)}{x(s)} = \frac{\chi\omega^2}{s^2 + \chi\omega s + \omega^2} \tag{59}$$

Where χ is the damping factor and ω is the fundamental frequency. The SOGI can filter the harmonics that are far from the fundamental frequency. The SOGI can effectively extract the fundamental component from signals associated with harmonic components. Thus, using SOGI the grid voltage v_g (t) and grid current i_g (t) can be formulated as,

$$\begin{aligned} v_{g\alpha}(t) &= V_g \sin(\omega t) \\ i_{g\alpha}(t) &= I_g \sin(\omega t + \varphi) \end{aligned} \tag{60}$$

$$\begin{aligned} v_{g\beta}(t) &= V_g \sin(\omega t + \pi/2) \\ i_{g\beta}(t) &= I_g \sin(\omega t + \varphi + \pi/2) \end{aligned} \tag{61}$$

Using this terminology and the instantaneous power analysis [118], the predictive equations for the active and reactive power can be determined as,

$$\tilde{P}(k+1) = \frac{T_S}{L}\begin{pmatrix} v_{i\alpha}(k)v_{g\alpha}(k) + v_{i\beta}(k)v_{g\beta}(k) \\ -v_{g\beta}^2(k) - v_{g\alpha}^2(k) \end{pmatrix} + P(k) \tag{62}$$

$$\tilde{Q}(k+1) = \frac{T_S}{L}\left(v_{i\alpha}(k)v_{g\beta}(k) - v_{i\beta}(k)v_{g\alpha}(k)\right) + Q(k) \tag{63}$$

B. Modes of Operation

Next generation PEIs similar to the one shown in Fig. 33 for grid-connected PV systems need to take into consideration the effects of reactive power injection into the grid under grid fault conditions. This is required according to grid standards and codes in addition to concern for the injected power quality.

The proposed system in Fig. 33 has two modes of operation: The MPP mode and the LVRT mode. In the MPP mode, the system operates at unity power factor and the maximum available active power from the PV is injected to the grid. The proposed system is also capable of providing reactive power for the grid as an ancillary service in the MPP mode. The system operates in MPP mode until the Sag Detector unit detects a grid voltage fault. After the fault detection, the controller triggers the mode change and the system enters the LVRT mode. In this mode, the system can tolerate the voltage drops for a short period of time. Simultaneously, the system injects reactive power into the grid to aid with re-establishing the grid voltage. The required reactive power injection in LVRT mode according to E.ON code [119] as an example, is illustrated in Fig. 35. As pictured, the required reactive power to recover the voltage is a function of the grid voltage (v_g). In addition to the grid voltage stabilization, in the LVRT mode, the avoidance of PV power generation can be realized [120]. The power generation profile during LVRT mode will be discussed in the next section.

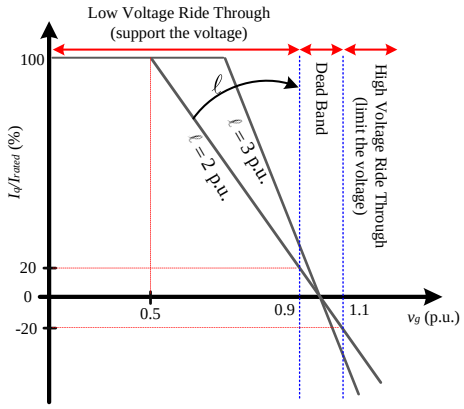

Fig. 35. Grid code requirement for reactive current injection, standard E.ON [93, 119, 121, 122]

C. Power Profiles

The overcurrent protection strategy and required amount of reactive power by the grid in LVRT mode determine the reactive power injection strategy. Literature suggests several reactive power injection strategies for single phase inverters [93, 122, 123]. Some notable examples are the

constant active current strategy, the constant average active power strategy, and the constant peak current strategy [122, 123]. The constant active current strategy extracts the maximum available power from the PV array. In this method, the amplitude of the injected current to the grid may exceed the inverter maximum allowable current. This operation situation may lead to the failure of the whole system and thus increase the operation and maintenance costs. Another approach to maximize the power harvest from the PV array is to maintain the average injected active power at a constant value in LVRT mode. This method is called constant average active power strategy. In this strategy also, there is a risk of overcurrent failure due to the demand for reactive power injection by the grid. In both aforementioned strategies, some constraints can be added to the controller to avoid inverter shutdown due to overcurrent protection. But considering an existing inverter with a specific robustness margin, enforcing additional constraints limits the reactive power injection capability. Thus, in this situation the active power generated by PV should be reduced to provide sufficient room for reactive power injection.

In this paper constant peak current strategy is used as the power profile during LVRT mode. In this method, the amplitude of the injected current to the grid is kept constant, thus the issue of overcurrent protection and inverter shutdown in previous two aforementioned methods are avoided. The current (I_q) injected can be calculated according to Fig. 35 as,

$$\begin{aligned} & I_q = \ell(1-v_g)I_{rated} \\ & \text{where: } 0.5 \text{ p.u.} \le v_g \le 0.9 \text{ p.u.} \\ & \qquad \ell \ge 2 \text{ p.u.} \end{aligned} \tag{64}$$

As it is shown in Fig. 35, for a specific grid voltage (v_g) and gain (ℓ), a certain level of reactive power should be injected into the grid according to level of voltage sag. For example for a 0.7 p.u. grid voltage (v_g) and $\ell = 2$ p.u., at least 70% of the rated grid current (I_{rated}) should be injected into grid. If the grid voltage (v_g) is less than 0.5 p.u., the ZSI will generate full reactive power (I_q=I_{rated}).

According to this grid code, the voltage control can have a dead band of ±0.1 as shown in Fig. 35. In this method, the maximum grid current is set as the rated current of the ZSI ($I_{g\text{-}max}$=I_{rated}). The phasor diagram of the system under normal grid condition and dur ing LVRT mode based on constant peak current strategy are illustrated in Fig. 36. As pictured, the injected active power to the grid is decreased in the LVRT mode.

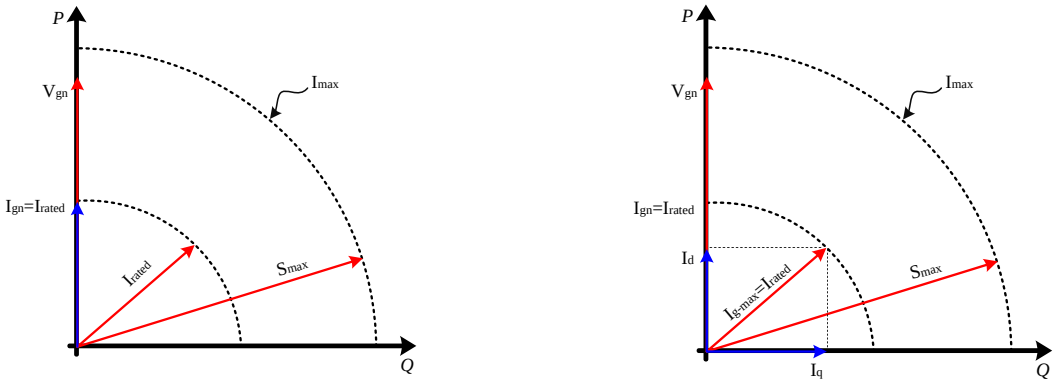

(a) Unity power factor power profile under normal grid condition.

(b) Constant peak current power profile during low voltage ride through operation.

Fig. 36. Power profile for single phase grid-tied z-source inverter.

D. Active and Reactive Power Refrence Generation

Active and reactive power control at the same time requires control of both of the power or their power components i.e. i_d and i_q. In this paper based on the mode of operation (MPPT or LVRT), the power components are adjusted through control of P and Q by MPC cost function. This section presents the active and reactive power reference generation for MPC cost function. During the normal grid condition operation, the reference for active power (P_{ref}) is determined by the MPPT unit. The previously developed model predictive based MPPT in [110] is used to harvest the maximum available power from the PV array under normal grid condition. This model predictive based MPPT method shifts the PV voltage to MPP voltage by adaptively incrementing/decrementing the future PV voltage according to proximity to MPP. The determined V_{PV} and I_{PV} can be used to calculate the P_{ref} in this mode of operation. This strategy minimizes the

oscillation around the MPP and improves the dynamic performance [110]. The reactive power reference (Q_{ref}) is set to zero for unity power factor operation in this mode of operation.

In the LVRT mode, the power reference is generated based on the grid requirement as shown in Fig. 35. Accordingly, the corresponding power factor in the LVRT mode can be expressed as,

$$\cos\varphi = \begin{cases} \sqrt{1-\ell^2\left(1-v_g\right)^2} & \left(1-1/\ell\right) < v_g < 0.9 \text{ p.u.} \\ 0 & v_g < \left(1-1/\ell\right) \text{ p.u.} \end{cases} \tag{65}$$

As mentioned in the previous section, the peak of injected current from ZSI into the grid is kept at its rated current ($I_{g\text{-}max}$=I_{rated}), then current (I_d) in *dq* rotating reference frame can be calculated as,

$$I_d = I_{rated}\sqrt{1-\ell^2\left(1-v_g\right)^2} \tag{66}$$

The required reactive current for injection can be determined by (64) in conjunction with grid code standard E.ON which is illustrated in Fig. 35. This standard demonstrate the required reactive power by the grid based on level of grid voltage sag. Thus the reference active (I_d) and reactive current (I_q) in LVRT can be calculated according to the grid standard (Fig. 35) and equations (64) and (66) in *dq* frame. Using the instantaneous power theory and calculated I_{dq}, the reference active (P_{ref}) and reactive (Q_{ref}) power can be calculated.

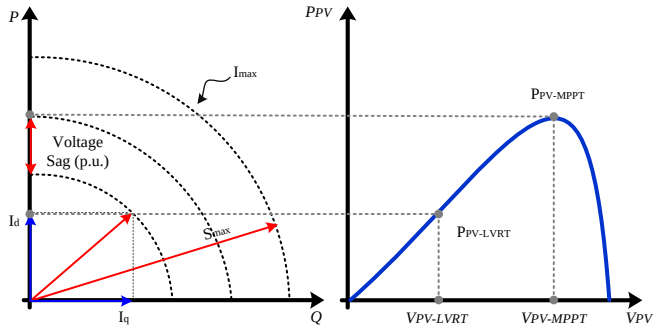

Fig. 37. Power profile for single phase grid-tied z-source inverter for photovoltaic application and P-V characteristics of photovoltaic panel when grid voltage sag occur: the active power drown from photovoltaic panel diminish in LVRT mode by moving from maximum power point operation coordinates when grid voltage sag occurs.

Fig. 37 illustrates the graphical representation of the power drawn from PV array during MPPT and LVRT modes of operation. The constant peak current strategy limits the active current drawn from the PV panels in LVRT in order to prevent ZSI shutdown due to current protection. As shown in Fig. 37, depending on the depth of voltage sag according to Fig. 35, the injected active current to the grid is decreased to maintain the constant grid peak current when delivering the required reactive current to the grid according to grid standards (Fig. 35). Thus, the active power drawn from the PV panels are decreased. In this situation, the PV power (P_{PV}) can be decreased by moving to the right or left of the MPP operating point. The proposed controller reduces the P_{PV} in LVRT mode by shifting the operating point to the left of the MPP as shown in Fig. 37, because operation in the right side of MPP may cause instability [124]. It is worth mentioning that, this strategy for the proposed PEI can be used for overnight operation of the PV system with energy storage in the absence of solar irradiance to support reactive power injection to the grid as an ancillary service.

E. MPC Cost Function Minimization

As mentioned in the previous section, the proposed system has two modes of operation: MPPT under normal grid condition and LVRT in case of grid voltage sag. Thus a hybrid cost function for MPC needs to be developed. The control variables references for the hybrid cost function is determined according to system's mode of operation, MPPT unit power output, and LVRT reference generation unit outputs. The sag detector triggers use of the appropriate weights in the hybrid cost function to change the mode from MPPT to LVRT. The designed cost function J is

$$
\begin{aligned}
&\min J^{\sigma\in[1,5]} = \sum_{n=1}^{2}\left(\lambda'_n g_P^{\sigma} + \lambda''_n g_Q^{\sigma} + \delta'_n g_{L1}^{\sigma} + \delta''_n g_{C1}^{\sigma}\right)\\
&\text{subject to}\quad g_P^{\sigma} = \left|\tilde{P}^{\sigma}(k+1) - P_{ref}^{n}(k)\right|,\\
&\qquad\qquad g_Q^{\sigma} = \left|\tilde{Q}^{\sigma}(k+1) - Q_{ref}^{n}(k)\right|,\\
&\qquad\qquad g_{L1}^{\sigma} = \left|\tilde{I}_{L1}^{\sigma}(k+1) - I_{L1-ref}^{n}(k)\right|,\\
&\qquad\qquad g_{C1}^{\sigma} = \left|\tilde{V}_{C1}^{\sigma}(k+1) - V_{C1-ref}^{n}(k)\right|.
\end{aligned}
\tag{67}
$$

In this cost function, *n* indicates the value of weighting factors associated to each mode of operation. Since we have a hybrid MPC cost function for each mode of operation (MPPT and LVRT), the weight factors ($\lambda'_n, \lambda''_n, \delta'_n, \delta''_n$) are selected adaptively based on the modes of operation. The system operates in MPPT and LVRT modes for *n* = 1 and *n* = 2 respectively. According to (18), two set of weight factors coefficient are selected: one set for MPPT mode (n=1) and another set for LVRT mode (n=2). If there is no grid voltage sag, then $\lambda'_{n=1}, \lambda''_{n=1}, \delta'_{n=1}, \delta''_{n=1} \neq 0$ and, if the voltage sag is detected then the $\lambda'_{n=1}, \lambda''_{n=1}, \delta'_{n=1}, \delta''_{n=1} = 0$ and the $\lambda'_{n=2}, \lambda''_{n=2}, \delta'_{n=2}, \delta''_{n=2} \neq 0$. This method of formulation will provide more flexibility to improve the dynamic performance of the reactive current injection to the grid in LVRT mode for provision of ancillary services. Similarly, in case of MPPT operation mode, priority can be given to PV power harvesting under dynamic PV ambient conditions.

The non-zero weights factors are determined using branch and bound technique [125, 126] in order to minimize the number of required simulations to find appropriate weight factors. This technique firstly identifies a couple of initial values for the weight factors (for example 4 values), commonly with different orders to have a very wide range. Then control objectives will be used as a measurement tool to narrow down the range of initially identified four weight factors by eliminating weight factors that doesn't meet the desired performance. Assuming that only two of the initially selected weight factors yield acceptable results, then four new weight factors will be

chosen for further tuning. This procedure is continued to finally determine optimal weight factors. In this paper we have chosen the tracking errors of each control objectives and injected grid current THD as a measurement tool for selection of weight factors using branch and bound technique.

The $I_{L1\text{-}ref}$ in MPPT mode is calculated from the determined maximum available PV power (P_{PV}) and the V_{PV} at MPP. In the LVRT mode, the $I_{L1\text{-}ref}$ is calculated according to the required reactive and active power that should be injected into the grid using the constant peak current method. In the LVRT mode, the system is not operating at its MPP, thus the P_{PV} and as a result $I_{L1\text{-}ref}$ will shift from MPP coordinates as shown in Fig. 37. The capacitor C_1 voltage should be greater than double the grid voltage [127], thus the $V_{C1\text{-}ref}$ is chosen to be $2.5\times V_{grid}$. Finally, the cost function (67) is minimized based on the system model for all active, zero, and shoot-through states $\left(\sigma \in [1,5]\right)$ and the calculated references according to the mode of operation. The predictions of the values of the control variables are obtained for each feasible voltage vector state, and the cost function (67) is calculated accordingly for each of these voltage vectors. The switching state σ that minimizes the cost function J^{σ} will be applied to the ZSI in Fig. 33.

F. Result and Discussion

The proposed system, illustrated in Fig. 33 with parameters given in Table V, is tested experimentally for several case studies in MPPT mode with normal grid condition and LVRT mode in case of grid voltage sag occurrence. Fig. 38 illustrates the proposed predictive model of the control objectives for MPC cost function. Fig. 38 (a) and (b) show the predictive model of inductor current and capacitor voltage in the impedance network (L_1 and C_1) for shoot- through mode and non shoot-through mode respectively. These predicted models depends on the system model parameters and sampling time T_S. Fig. 38 (c) shows the predicted active and reactive power

(P and Q) for regulating them based on MPPT and LVRT reference generation through MPC cost function (67).

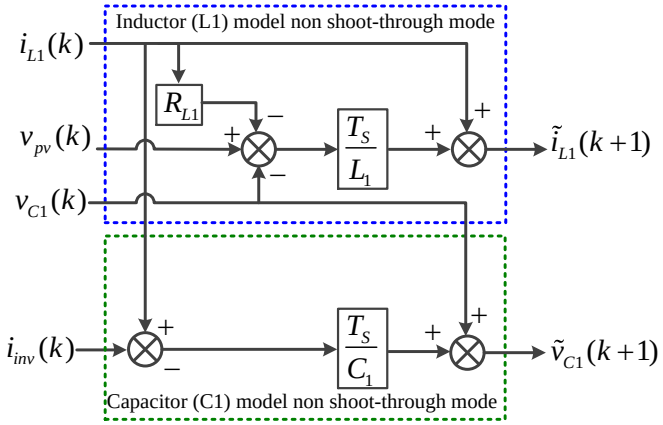

(a) Predictive model of the inductor current and capacitor voltage (L1, C1) in non shoot-through mode.

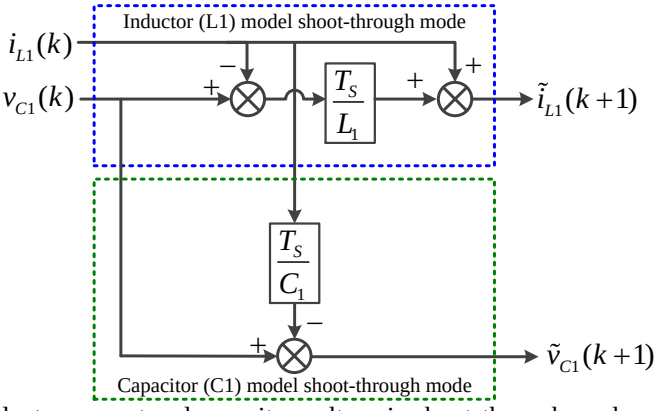

(b) Predictive model of the inductor current and capacitor voltage in shoot-through mode

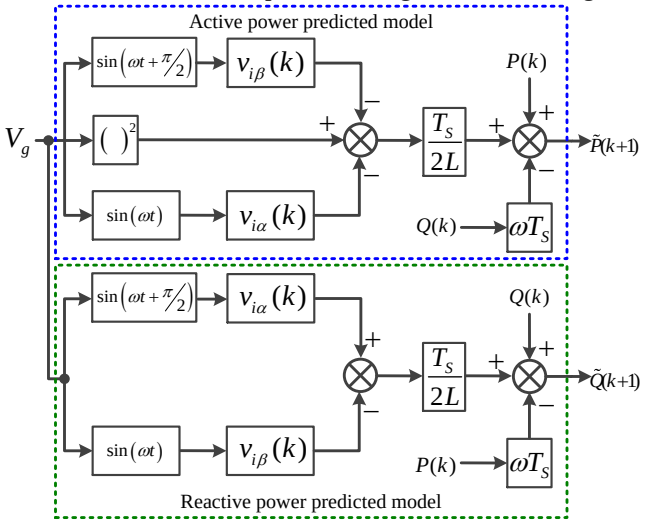

(c) active and reactive power predictive model.

Fig. 38. Proposed model predictive control block diagram.

The performance of the proposed system is evaluated by looking into the following important merit criteria: harvesting the maximum power with small oscillation around MPP, fast dynamic response under dynamic PV ambient condition, robust operation under grid voltage sag, reactive power injection support in LVRT mode according to grid standards and codes such as E.ON standard [119], decoupled active and reactive power control in MPPT mode without affecting the boosting operation of ZSI, and high quality current injection to the grid considering the Total Harmonic Distortion (THD) limits according to IEEE-519 standards [86].

In order to start the experiments, the system is initially tested in normal grid condition with the objective to operate at MPPT with unity power factor. The resulting waveforms for this condition are shown in the scope shot of Fig. 39 (a). Remaining in the healthy grid condition, the system is tested through a more realistic scenario in which the grid voltage has distortions. In this experiment, the highest allowed values of 3^{rd}, 5^{th}, 7^{th}, and 11^{th} order harmonics according to IEEE-519 standards [86] are added to grid voltage (v_g) using a programmable ac power source. As shown in the scope shot of Fig. 39 (b), the control objectives are achieved perfectly even in presence of grid voltage harmonics.

The performance of the controller during a grid voltage sag event (due to a fault) is tested next. The resulting waveforms are shown in the scope shots of Figs. 39 (c) and (d). In this experiment, the system is initially operating with normal grid condition at unity power factor. Subsequently, at time instant t_1, the sag detector detects 25% voltage sag in the grid voltage and according to the LVRT operation requirement and depth of sag, the ZSI is triggered to inject 400 VAR reactive power into the grid. As pictured in Fig. 39 (c), the peak of the grid current is kept constant before and after the reactive current injection, thus achieving the proposed predictive controller objective to maintain constant peak current in this mode of operation. Later, at instant t_2 the grid voltage

returns to normal condition, and the controller is triggered to return to MPPT operation mode at unity power factor as shown in Fig. 39 (d).

The last experiment is examining the response of the system to a change in solar irradiance in normal and faulty grid conditions. The effect of solar irradiance changes in normal grid condition (MPPT mode) is illustrated in Fig. 40 (a). The solar irradiance is initially at 1000 W/m^2, then at time t_3 the solar irradiance is stepped down to 700 W/m^2. As pictured, the peak grid current and inductor L_1 current are decreased according to the P-V characteristic of the PV panel. The grid current is maintained constant according to the available power from the PV panel and the step change in solar irradiance did not cause any inrush grid current. Fig. 40 (b) illustrates the response of the proposed system to step change in solar irradiance after the sag detector detects a 25% grid voltage sag and puts the system in the LVRT mode. The solar irradiance is initially at 700 W/m^2, then at time t_4 the solar irradiance is stepped up to 1000 W/m^2. As pictured, this change causes an increase in the grid peak current and inductor L_1 current. This case study demonstrates the capability of adjusting the power drawn from the PV panel by moving along P-V characteristic curve of PV panel according to available solar irradiance and depths of voltage sag to maintain LVRT operation requirement.

Finally, the active and reactive power for experiments in Figs. 39 (c) and (d) are obtained from oscilloscope and plotted in MATLAB for better observation of dynamic response of the controller when the sag detector detects 25% grid voltage sag. As it is shown in Fig. 41, the level of active power injected into grid is decreased to provide sufficient room for reactive power injection according to LVRT control mode requirement. Due to the capability of MPC for predicting the error before applying the switching state to the ZSI, the change in the mode of operation from MPPT to LVRT and vice versa is achieved seamlessly. As it is shown in Fig. 41, the proposed

predictive controller for ZSI, without requirement of challenging tuning in each mode of operation, has promising dynamic response and high control efficacy in steady state operation. Similarly, as pictured in the scope shots of Figs. 40, the proposed predictive controller effectively shifts the operating point of the ZSI along the P-V characteristic curve of the PV panel to maximize the energy harvest and provide the required reactive power without inrush grid current or diminishing the grid power quality. The individual harmonic components of the grid side current, i_g, are presented in Table. III. The calculated THD of i_g is 2.87% which is within the IEEE-519 standards for grid-tied systems.

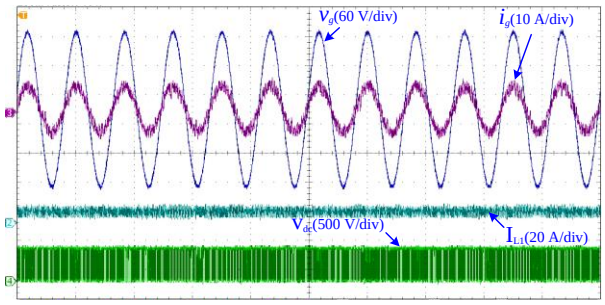

(a) The grid voltage (v_g), grid current (i_g), inductor L1 current (I_{L1}), and pulsating dc-link voltage (V_{dc}) when the system is operating in MPPT mode and unit power factor in normal grid condition.

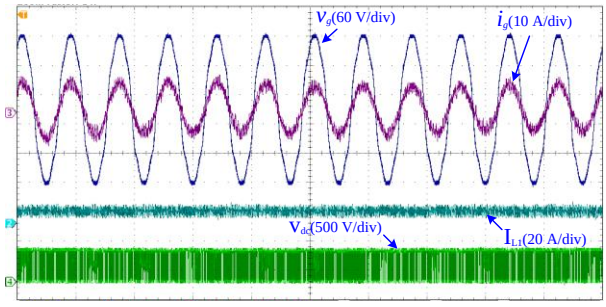

(b) The grid voltage (v_g), grid current (i_g), inductor L1 current (I_{L1}), and pulsating dc-link voltage (V_{dc}) when the system is operating in MPPT mode and unit power factor in normal grid condition with distorted grid voltage.

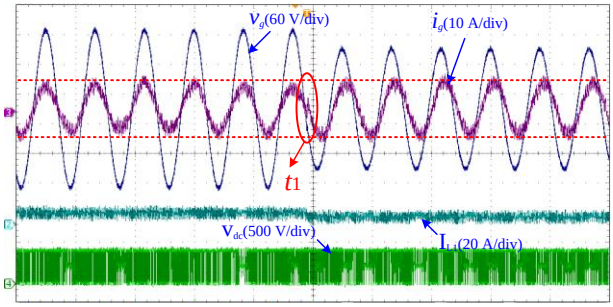

(c) The grid voltage (v_g), grid current (i_g), inductor L1 current (I_{L1}), and pulsating dc-link voltage (V_{dc}) when the 25% grid voltage sag occur at t_1 and the system change its mode of operation from MPPT to LVRT with reactive current injection

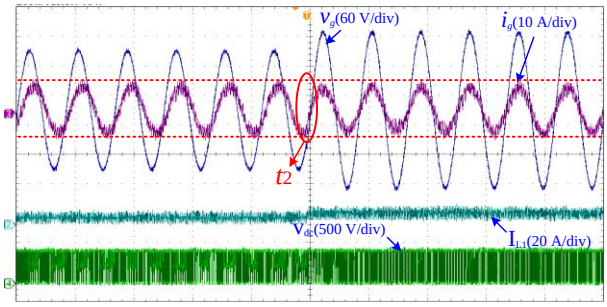

(d) The grid voltage (v_g), grid current (i_g), inductor L1 current (I_{L1}), and pulsating dc-link voltage (V_{dc}) when the grid goes back to normal condition at t_2 and the system changes it mode from LVRT to MPPT with unity power factor.

Fig. 39. System performance evaluation in steady state MPPT mode and transition between LVRT and MPPT modes.

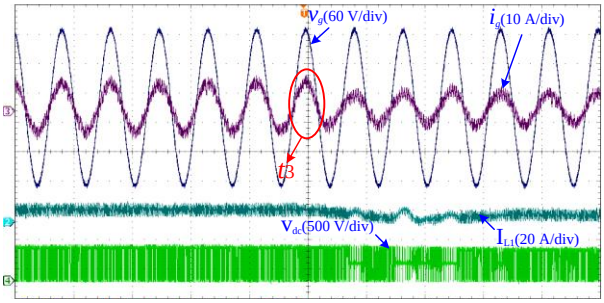

(a) The grid voltage (v_g), grid current (i_g), inductor L1 current (I_{L1}), and pulsating dc-link voltage (V_{dc}) with step change in solar irradiance level from 1000 W/m^2 to 700 W/m^2 at time t_3 when the system is operating in MPPT mode under normal grid condition.

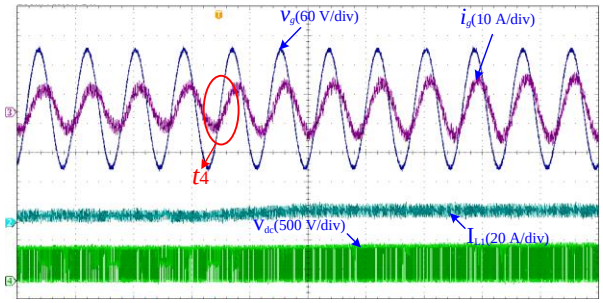

(b) The grid voltage (v_g), grid current (i_g), inductor L1 current (I_{L1}), and pulsating dc-link voltage (V_{dc}) with step change in solar irradiance level from 700 W/m^2 to 1000 W/m^2 at time t_4 when the system is operating in LVRT mode and 25% grid voltage sag.

Fig. 40. System performance evaluation to change in solar irradiance in MPPT and LVRT modes.

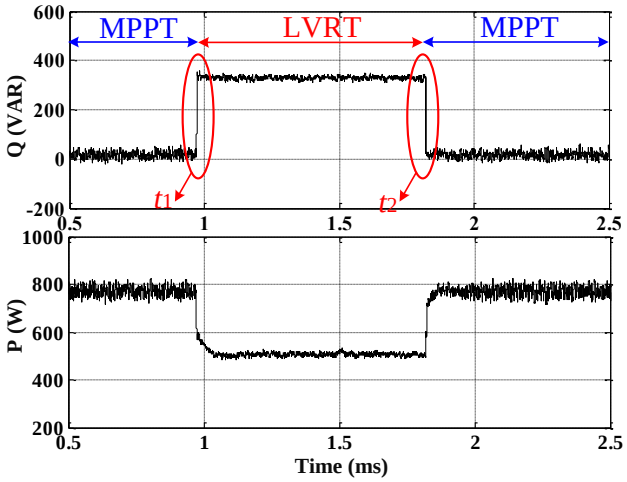

Fig. 41. Active and reactive power when the grid voltage sag of 25% occur for time interval t_1 to t_2. The system is operating in normal grid condition before t_1 and after t_2.

TABLE V: System Parameters

Parameter	Value
C1	1000 µF
C2	1000 µF
L1	0.7 mH
L2	0.7 mH
Sampling time	60 µs
Cpv	470 µF
Lgrid	1 mH

TABLE VI: Grid current harmonics distortions

Harmonics Order	Distortion (%)
3rd	0.79%
5th	1.1%
7th	0.34%
9th	0.28%
11th	0.18%
13th	0.06%
15th	0.04%
17th	0.08%

G. Conclusion

This section of the dissertation proposes a single stage power electronics interface based on impedance source inverter for photovoltaic applications with LVRT capability during the grid voltage sag according to grid standards. By using the MPC framework, a simple control strategy is proposed with an adaptive cost function to seamlessly operate under normal and faulty grid

condition. The proposed system eliminates the requirements of multi-nested-loop of classical controller. Due to the predictive nature of the controller, the proposed system has fast dynamic response to change in solar irradiance or grid reactive power requirement according to LVRT operation. The system is switching between LVRT and MPPT modes of operation seamlessly. The proposed system can be extended for overnight operation of PV sources in DGs with reactive power compensation capability as ancillary service from DG to main grid. Several experiments have been conducted to verify the performance of the proposed system. The results demonstrates robust operation, maximum power point operation during the healthy grid condition, high power quality injection during steady state condition, negligible overshoot/undershoot in grid current injection due to change in solar irradiance or reactive power reference, no observation of inrush current during dynamic change in MPC cost function references for LVRT operation, and maintaining constant peak grid current during LVRT mode.

V. Extremum Seeking Based Model Predictive MPPT for Grid-tied Z-Source Inverter for Photovoltaic Syetems

A. System Description

The purpose of this paper is to propose a discrete-in-time ES based Predictive MPPT (referred to as ESP-MPPT hereinafter) method without a modulator for a ZSI acting as a PEI, Fig. 42. The predictive controllers can be used for implementation of ES based MPPT algorithms on ZSIs with multi-objective control functionality. Comparing to classical control schemes, MPC techniques deliver fast dynamic response with high stability margin, making them well suited for PV systems in harsh ambient condition and abnormal grid condition. Also, for the ZSIs, the MPC eliminates the complex modulation stage required to implement the shoot through state [128].

The provided stability analysis of the proposed method by Lyapunov's Theorem guarantees the convergence of the algorithm to the MPP. The proposed method exhibits better performance in comparison to conventional hill-climbing methods and requires less computational effort than artificial intelligence-based and complex mathematical methods. This work proposes a method that performs better than the conventional MPPT methods while requiring less computational effort than more modern MPPT techniques, and is backed by a rigorous proof of convergence that guarantees stable operation even in presence of noise and dynamical environmental conditions. In addition, the proposed approach features fast dynamic response and negligible oscillations around the MPP at steady state, which results in size reduction of passive components in the impedance network of ZSI which is a challenge in ZSI design [129]. The one-line block diagram of the proposed system is illustrated in Fig. 42, the detail system description will be presented in sections B and C.

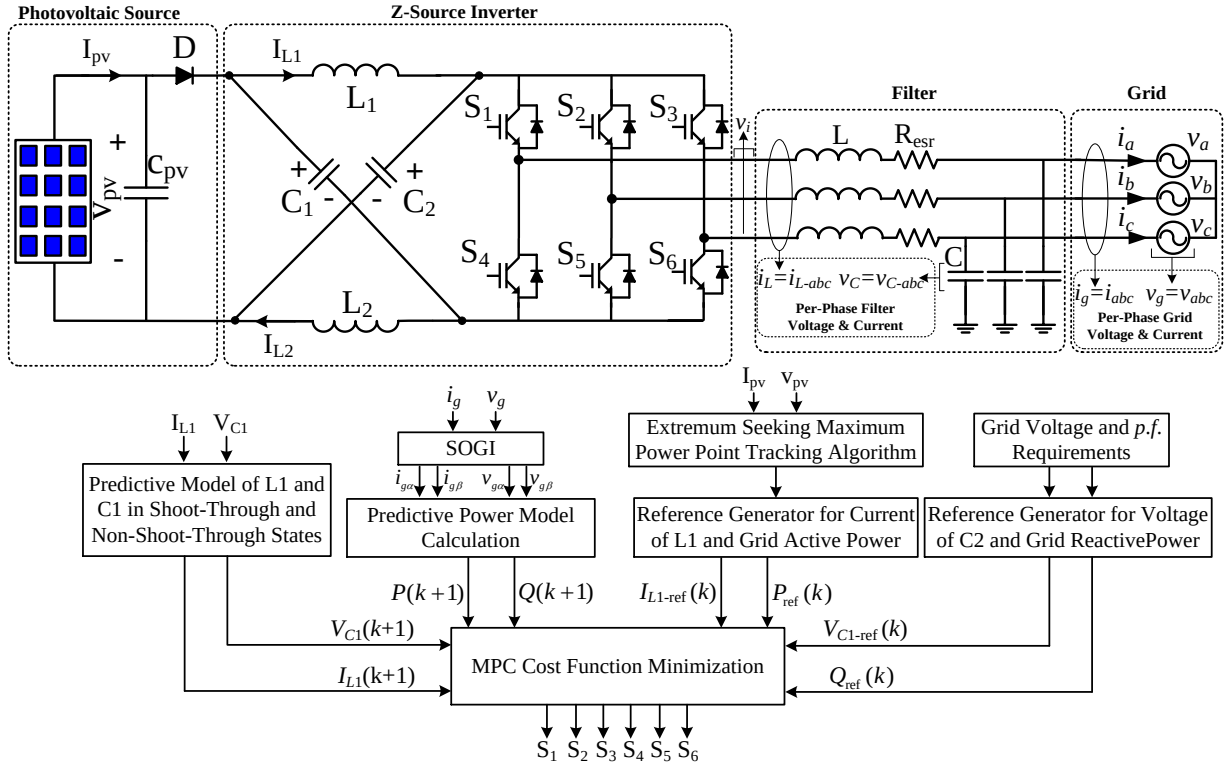

Fig. 42. General schematic of the proposed power electronics interface based on grid-tied z-source inverter for photovoltaic application.

B. System Model

This section presents the predictive modeling of the grid side filter and the PV side impedance network. The dynamic model of the grid side filter is given by,

$$\frac{d}{dt} i_L(t) = \frac{1}{L}(v_i(t) - v_g(t) - i_L(t)R_{esr}) \tag{68}$$

$$\frac{d}{dt} v_C(t) = \frac{d}{dt} v_g(t) = \frac{1}{C}(i_L(t) - i_g(t)) \tag{69}$$

Where i_L(t) is the inductor current, v_i(t) is the output voltage of the inverter, v_g(t) is the ac grid voltage, L and C are the filter's inductance and capacitance values, and R_{esr} is the equivalent series resistance of the inductor. By applying the Euler forward approximation method to (68)-(69), they can be discretized,

$$\tilde{i}_L(k+1) = \frac{T_s}{L}(v_i(k) - v_g(k) - i_L(k)R_{esr}) + i_L(k) \tag{70}$$

$$\tilde{v}_C(k+1) = \frac{T_s}{C}(i_L(k) - i_g(k)) + v_C(k) \tag{71}$$

where *Ts* is the sampling period.

One of the main characteristics of ZSI is its shoot-through mode for flexible boosting of the input (PV) voltage. In this mode, both switches in one leg of the inverter are simultaneously turned ON. The equivalent circuit model of the ZSI in Fig. 42 for shoot-through mode and non-shoot-through modes (active states) are illustrated in Fig. 43 (a) and (b). Using these equivalent circuits and Euler forward approximation, the predictive model of the Z source network can be developed [35]. According to [35], the predictive equations for the inductor L_1 current and capacitor C_1 voltage in a non-shoot-through mode are,

$$\tilde{I}_{L1}(k+1) = I_{L1}(k) + \frac{T_S}{L_1}(V_{pv}(k) - V_{C1}(k) - R_{L1}I_{L1}(k)) \tag{72}$$

$$\tilde{V}_{C1}(k+1) = V_{C1}(k) + \frac{T_S}{C_1}(I_{L1}(k) - I_{inv}(k)) \tag{73}$$

while the same equations for a shoot-through state are,

$$\tilde{I}_{L1}(k+1) = I_{L1}(k) + \frac{T_S}{L_1}(V_{C1}(k) - R_{L1}I_{L1}(k)) \tag{74}$$

$$\tilde{V}_{C1}(k+1) = V_{C1}(k) - \frac{T_S}{C_1}I_{L1}(k) \tag{75}$$

The second order general integrator (SOGI) [115] is used to determine the in-phase and quadrature component ($\alpha\beta$) of grid voltage and current. Thus, by using the instantaneous power analysis [118] and the $\alpha\beta$ component of grid voltage and current, the predictive equations for the active and reactive power can be determined as

$$\tilde{P}(k+1) = \frac{T_S}{L}\begin{pmatrix} v_{i\alpha}(k)v_{g\alpha}(k) + v_{i\beta}(k)v_{g\beta}(k) \\ -v_{g\beta}^2(k) - v_{g\alpha}^2(k) \end{pmatrix} + P(k) \tag{76}$$

$$\tilde{Q}(k+1) = \frac{T_S}{L}\left(v_{i\alpha}(k)v_{g\beta}(k) - v_{i\beta}(k)v_{g\alpha}(k)\right) + Q(k) \tag{77}$$

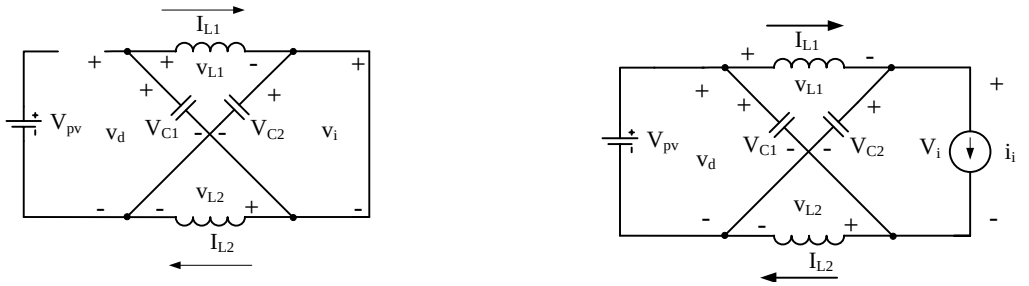

(a) equivalent circuit in shoot-through mode (b) equivalent circuit in non-shoot-through mode

Fig. 43. Equivalent circuit model of the impedance network of ZSI in Fig. 1 during shoot-through and non-shoot-through modes.

C. Proposed Contorller for Photovoltaic Side of ZSI

The Extremum Seeking Maximum Power Point Tracking Algorithm block diagram in Fig. 42 is responsible for determining a desirable trajectory for the L_1 current that leads to MPP. The trajectory provided by this block is tracked using the MPC. The MPC approach for determination of optimal switching state at each iteration are commonly formulated in discrete-time with fixed sampling intervals. This concept fits well with the proposed discrete-in-time ES based predictive MPPT algorithm. The general model of the ZSI impedance network can be represented as a nonlinear system in discrete-time state space form as,

$$x_{k+1} = f(x_k, u_k) \tag{78}$$

where $x \in \mathbb{R}^n$ and $u \in \mathbb{R}^m$ are the states and the inputs of the converter. For the ZSI of Fig. 42, for instance, one of the controller inputs for MPC is the reference signal generated by the Extremum Seeking-MPPT block and the states are the PV panel voltage (V_{pv}) and current (I_{pv}). The states (x) are inputs of a function that represents the P-V characteristic of the PV panel,

$$y = h(x) \tag{79}$$

where $h(x) \in \mathbb{R}$ is unknown and depends upon the ambient conditions and some elements of x, and y are the output power of the PV panel. While the MPPT algorithm is operating, it samples the inputs and outputs of this function (PV voltage and power, respectively). As a result, the sampled function can be represented as $y_k = h(x_k)$ where the subscript $k \in \mathbb{N}$ denotes the sampling of the MPPT algorithm. The subscript k will be used throughout the paper for all the

quantities sampled with this same rate. According to PV characteristic curves, (79) has a unique global maxima y_k^* (maximum power) subject to be found by adaptively tracking x_k^* (PV current),

$$y_k^* = \max_{x_k} h(x_k) = h(x_k^*) \tag{80}$$

The MPPT algorithm is responsible for the accurate tracking of x_k^* in presence of ambient and parameter variations. It also should be able to make the system globally asymptotically stable, and be easy and economical to implement. Without loss of generality, it is safe to assume that $h(x_k)$ can be expressed in a Linear-In-Parameter (LIP) form [130], similar to

$$h(x_k) = \gamma^T S(x_k) \tag{81}$$

where $\gamma \in \mathbb{R}^l$ is a vector of unknown parameters and is a known regression vector function of x_k . A typical P-V curve similar to the ones shown in Fig. 44 has a unique maxima that allows for the assumption that $h(x_k)$ can be locally expressed as a second-order polynomial in the following form: $S(x_k) \in \mathbb{R}^l$

$$h(x_k) = ax_k + bx_k^2 \tag{82}$$

where $a, b \in \mathbb{R}$ are unknown parameters. A second polynomial in form of (82) is chosen due to P-V characteristics as illustrated in Fig. 44. By looking at the Fig 44, one can recognize that the P-V curve has to pass through the origin that means the first term can be selected as zero, to minimize the estimation error and computation effort. Furthermore, the P-V curve is convex with a unique maximum which indicates that a polynomial in the form of (82) is an appropriate candidate to locally estimate it. Due to the same reason, a first order polynomial is not an appropriate fit because it does not offer any local maximum. Further, if we select a 3rd order polynomial, we will only add extra computation error to the estimation process because the estimation of the x^3 coefficient will inevitably converge to zero. In other words, on one hand, the developed theory in this work supports the selection of any higher order polynomial. But on the other hand, unnecessary higher

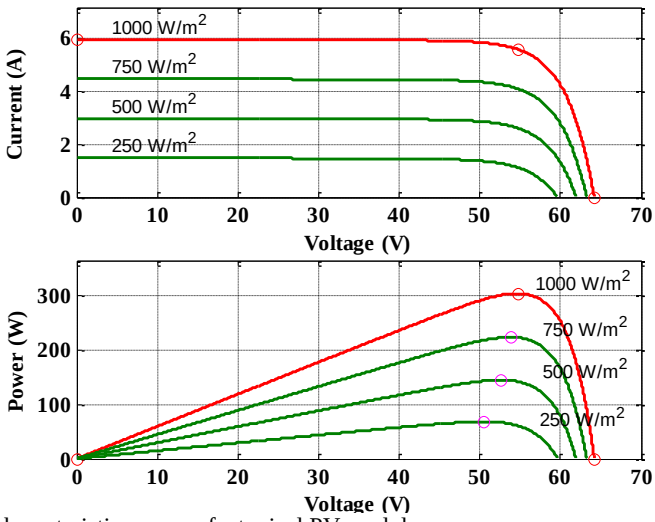

Fig. 44. The P-V and I-V characteristic curves of a typical PV module.

orders may cause larger transient errors and more demand of processing power. In (82), the vector of unknown parameters is equal to

$$\gamma = \begin{bmatrix} a & b \end{bmatrix}^T \tag{83}$$

and the regression vector is

$$S(x_k) = \begin{bmatrix} x_k & x_k^2 \end{bmatrix}^T \tag{84}$$

The $h(x_k)$ has a unique max that can be found by solving the differential equation obtained by taking the derivative of (81),

$$\frac{\partial h(x_k)}{\partial x_k} = \gamma^T \frac{\partial S(x_k)}{\partial x_k} = 0 \tag{85}$$

This equation has a unique solution with respect to x_k (MPP). The proposed MPPT method introduces the following iterative hill-climbing formula based on (85) that generates a desired trajectory (x_{k+1}^d) at (k+1) for the states to climb to the MPP,

$$x_{k+1}^d = x_k + \frac{\eta_k \hat{\gamma}_k^T \dfrac{\partial S(x_k)}{\partial x_k}}{1 + \left| \hat{\gamma}_k^T \dfrac{\partial S(x_k)}{\partial x_k} \right|} \tag{86}$$

where η_k is an adaptation parameter which will be discussed further below, and $\hat{\gamma}_k$ is the estimated value of γ_k. It will be proven later in this section that by convergence of $\hat{\gamma}_k$ to γ_k, the generated desired trajectory will direct the system toward the MPP. As a result, an update law to

effectively estimate $\hat{\gamma}_k$ is required for operation of this MPPT method. The proposed update law for estimation of $\hat{\gamma}_k$ based on least square estimation is

$$\hat{\gamma}_{k+1} = \left(\bar{S}_k^T \bar{S}_k\right)^{-1} \bar{S}_k^T Y_k \tag{87}$$

where Y_k is the sampled output vector,

$$Y_k = \begin{bmatrix} y_k & \dots & y_{k-j} \end{bmatrix}^T \tag{88}$$

and $\bar{S}_k$ is the sampled regression matrix of the form,

$$\bar{S}_k = \begin{bmatrix} S(x_k) & \dots & S(x_{k-j-1}) \end{bmatrix}^T \tag{89}$$

The *j* in (88) and (89) is the size of the sampled data stored in the memory. For example, for *j* equal to 3 the sampled output and regression matrices are,

$$Y_k = \begin{bmatrix} y_k & y_{k-1} & y_{k-2} \end{bmatrix}^T, S_k = \begin{bmatrix} x_k & x_k^2 \\ x_{k-1} & x_{k-1}^2 \\ x_{k-2} & x_{k-2}^2 \end{bmatrix} \tag{90}$$

The block diagram of the proposed MPPT system is shown in Fig. 45. The *Converter Dynamics* block in this figure represents the general dynamic model of the converter as in (78). The *PV Panel* block represents the P-V characteristic of the panel based on (79). The states of the converter (x_k) are inputs to this block. The output of this block is the amount of power generated by the PV panel (y_k). The two *Sample/Hold and Memory* blocks sample the states and the PV power and form Y_k and $\bar{S}_k$ in (88)-(89). These matrices are then fed to the *Parameter Estimator* block that realizes (87) to generate $\hat{\gamma}_k$. The estimated parameter vector ($\hat{\gamma}_k$) is then transferred to the *Desired Trajectory Determination* block to generate the desired state trajectory (x_k^d) based on (86). Thus two of the reference signals ($I_{L1-\text{ref}}(k), P_{\text{ref}}(k)$) for the MPC cost function formulation are determined as shown in Fig. 42. The MPC cost function, which will be developed at the end of this section, will track the desired trajectory (x_k^d) by operating in the shoot through and non-shoot through states. This results in the states of the system of (78) to converge to equilibrium point at x_k^* that coincides with the MPP,

$$x_{k+1}^* = x_k^* = f(x_k^*, u_k^*) \tag{91}$$

The optimization of the MPC cost function is performed with a sampling time at least two times

smaller than the sampling time of the Extremum Seeking-MPPT algorithm (desirable trajectory determination algorithm in Fig. 45). This gives the MPC enough time to safely regulate the states (x_{k+1}) to the desired reference points (x_k^d) before the next iteration of the MPPT loop. As a result, from the point of view of the outer MPPT loop, the actual states of the system are always equal to the desired states. With this assumption, from (86), it will not be an abuse of notation to write the MPPT algorithm's dynamics as

$$x_{k+1} = x_k + \frac{\eta_k \hat{\gamma}_k^T \dfrac{\partial S(x_k)}{\partial x_k}}{1 + \left| \hat{\gamma}_k^T \dfrac{\partial S(x_k)}{\partial x_k} \right|} \tag{92}$$

Although it is proven in [131] that the least squares estimation method utilized in (92) provides γ with minimum estimation error, to guarantee that $\bar{S}_K^T \bar{S}_K$ in (87) is invertible, the outer Extremum Seeking-MPPT algorithm should guarantee that at least two rows of (89) are linearly independent. The invertibility of $\bar{S}_K^T \bar{S}_K$ is in fact guaranteed according to the Persistence of Excitation (PE) [130] effect by the system's switching ripple imposed on all the system's states.

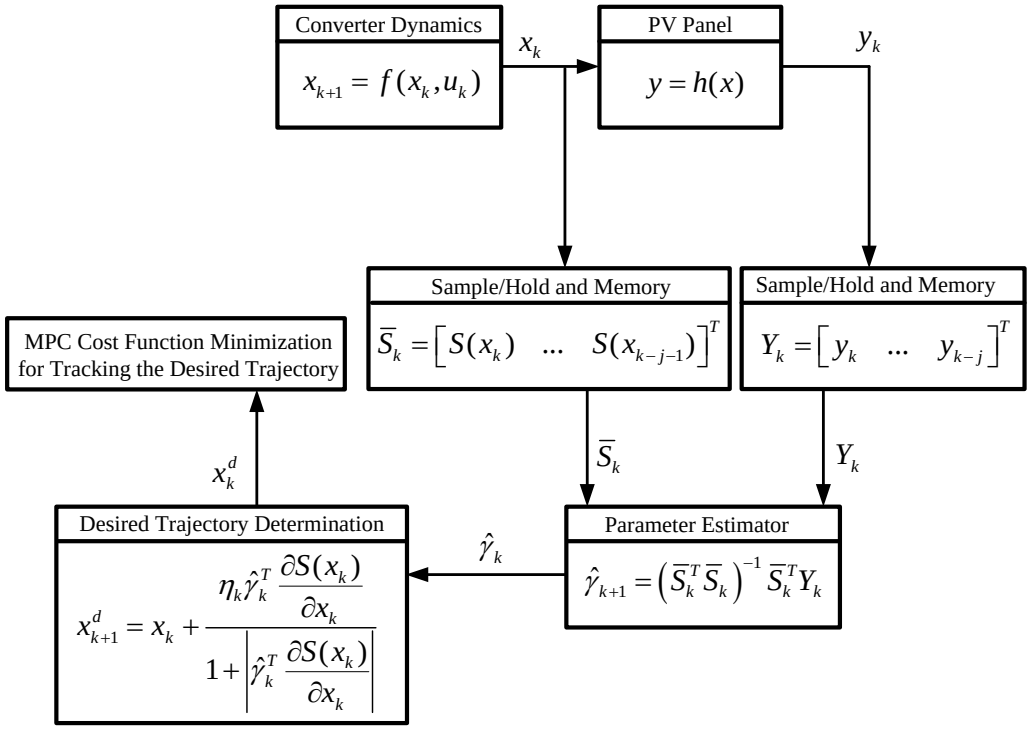

Fig. 45. The block diagram of the proposed ESP-MPPT method.

D. Proposed Controller for Grid Side of ZSI

At the grid side, the controller should inject the maximum power harvested from the PV panel and control the ratio of active/reactive power injected to the grid (power factor control). The developed grid side system model given by equations (76) and (77) are used to achieve these control objectives. Thus (76) and (77) are calculated for all possible voltage vectors. For the ZSI nine vectors are considered including six active states, two null states, and one shoot through state. Then the MPC cost function evaluates and compare these resulting (76) and (77) values with the desired active and reactive power to be injected to the grid. The active power reference ($P_{\text{ref}}(k)$) can be determined from the proposed ESP-MPPT method explained earlier in this section. The reactive power reference ($Q_{\text{ref}}(k)$) can be zero for unity p.f. operation or can be set by the grid operator according to grid requirement as an ancillary service.

E. MPC Cost Function Optimization

The control objectives for the ZSI are the inductor (L_1) current (I_{L1}), the capacitor (C_1) voltage (V_{C1}), the grid side active power (P), and the grid side reactive power (Q). In summary, the reference signal for inductor (L_1) current (I_{L1}) and active power (P) are determined from the ESP-MPPT. The reference signal for reactive power (Q) is set according to grid requirement by the grid operator or grid standards such as E.ON [119]. The capacitor (C_1) voltage (V_{C1}) reference signal is assumed to be 600 V which is more than double the grid voltage of 208 V_{RMS} to transfer the active power easily. The reference value for (V_{C1}) can be different according to active/reactive power requirement of the grid.

As explained in the previous section, the PV side of the system in Fig. 42 has 2 states: shoot through and non-shoot through states. This results into two possible values for ($V_{C1}(k+1)$) and ($I_{L1}(k+1)$) which can be calculated according to (72)-(75). For the grid side components (P, Q), there are 9 possible voltage vectors that results into 9 values for P (k+1) and Q (k+1) and are calculated using (76)-(77). Finally, in order to determine the optimal switching signal for the ZSI, a single cost function g is developed with all these control objectives and their corresponding desired values. The designed cost function g subject to minimization is given by,

$$\begin{aligned}
&\min g^{\sigma\in[1,9],\vartheta\in[1,2]} = \lambda_1 g_P^{\sigma} + \lambda_2 g_Q^{\sigma} + \lambda_3 g_{L1}^{\vartheta} + \lambda_4 g_{C1}^{\vartheta} \\
&\text{subject to} \\
&g_P^{\sigma} = \left|\tilde{P}^{\sigma}(k+1) - P_{ref}(k)\right|, g_Q^{\sigma} = \left|\tilde{Q}^{\sigma}(k+1) - Q_{ref}(k)\right|, \\
&g_{L1}^{\vartheta} = \left|\tilde{I}_{L1}^{\vartheta}(k+1) - I_{L1ref}(k)\right|, g_{C1}^{\vartheta} = \left|\tilde{V}_{C1}^{\vartheta}(k+1) - V_{C1ref}(k)\right|.
\end{aligned} \tag{93}$$

In this cost function, $\sigma \in [1,9]$ represents the 9 possible voltage vectors of ZSI and $\vartheta \in [1,2]$ represents the shoot through and non-shoot through states for $V_{C1}(k+1)$ and $I_{L1}(k+1)$ calculation. The switching state that minimizes the cost function g will be applied to the ZSI in Fig. 42. The value of weight factors $\lambda_{[1\text{-}4]}$ in (93) are determined by branch and bound technique [125]. The

branch and bound technique is a structured search method to determine certain variables in multi-objective control techniques according to several defined figures of merit. The figures of merit considered in this paper according to cost function (93) are the active and reactive power, inductor L_1 current, and capacitor C_1 voltage. The terms (M_1, M_2, M_3, M_4) are defined, these terms correspond to the measured active power, reactive power, L_1 current, and C_1 voltage respectively. The weight factors trades-off the control objectives in (93) versus each other, thus M_1, M_2, M_3, M_4 are evaluated for each group of weight factors ($\lambda_{1\text{-}4}$ at each iteration) to ensure that the tracking performance of control objectives are within desired performance specifications. In order to start the iterations, four values for the weight factors are selected $\lambda_{1\text{-}4}$ = (0.01, 0.1, 1, 10), then $M_{1\text{-}4}$ are measured for each of these weight factors. Since we have four weight factors in (93), for each iteration 2^4=16 evaluation for $M_{1\text{-}4}$ can be performed. Assuming that only the smaller values of the weight factors yield acceptable results, the interval [(0.01, 0.1)] are considered for further tuning. An additional value of λ is computed as the mean of the two endpoints (λ=0.055), and $M_{1\text{-}4}$ are again computed and evaluated for the new set of λ values. This procedure of branching and bounding weight factors is continued until an optimized value of λ is found. In order to furthermore minimize the simulations at each iteration, the value of one of the weight factors can be consider to be equal to 1 i.e. λ_1=1, and $\lambda_{2\text{-}4}$ can be tuned only. This is feasible because the ratio of the weight factors in multi-objective cost function is important, not their individual values.

F. Convergence Analysis of the ESP-MPPT

The concluding part in this section is to provide the proof of convergence for the proposed MPPT method. The proof of convergence is provided in the form of a theorem as follows:

Theorem - Consider the converter system of (78) harvesting energy from the PV panel with the P-V characteristic of (79), where $h(x_k)$ is unknown and variable with ambient condition

changes. Assuming the converter is operating under an input voltage controller that can stabilize the tracking error $e_k = x_k - x_k^d$ for a desired state trajectory x_k^d, if desired state trajectory is generated by (86) and unknown parameters of $h(x_k)$ are estimated using (87), then the desired state trajectory will converge to an equilibrium point that coincides with the MPP of the PV panel (x_k^*), where $\hat{\gamma}_k^T \partial S(x_k^*) / \partial x_k^* = 0$.

Proof – According to (85), the main objective is to prove that for the generated desired state trajectory,

$$\gamma^T \frac{\partial S(x_k)}{\partial x_k} \to 0 \tag{94}$$

by evolution of time. This means proving that the derivative of states go to zero under the proposed MPP tracker, which is the case when converging to the MPP. From (83)-(84) the following can be obtained:

$$\gamma^T \frac{\partial S(x_{k+1})}{\partial x_{k+1}} = a + 2bx_{k+1} \tag{95}$$

Substituting (92) in (95) yields

$$\begin{aligned} \gamma^T \frac{\partial S(x_{k+1})}{\partial x_{k+1}} &= a + 2bx_k + 2b \frac{\eta_k \hat{\gamma}_k^T \dfrac{\partial S(x_k)}{\partial x_k}}{1 + \left| \hat{\gamma}_k^T \dfrac{\partial S(x_k)}{\partial x_k} \right|} \\ &= a + 2bx_k + 2b \frac{\eta_k \left(a + 2bx_k \right)}{1 + \left| a + 2bx_k \right|} \end{aligned} \tag{96}$$

Using

$$\gamma^T \frac{\partial S(x_{k+1})}{\partial x_{k+1}} = a + 2bx_{k+1} \tag{97}$$

in (96) leads to further simplification of (98):

$$\gamma^T \frac{\partial S(x_{k+1})}{\partial x_{k+1}} = a + 2bx_k + 2b\frac{\eta_k\left(a+2bx_k\right)}{1+\left|a+2bx_k\right|} = \left(a+2bx_k\right)\left[1+2b\eta_k\frac{1}{1+\left|a+2bx_k\right|}\right] \tag{98}$$

Using (97), this equation can be transformed to

$$\gamma^T \frac{\partial S(x_{k+1})}{\partial x_{k+1}} = \gamma^T \frac{\partial S(x_k)}{\partial x_k}\left[1+2b\eta_k\frac{1}{1+\left|a+2bx_k\right|}\right] \tag{99}$$

Therefore, if the following holds,

$$-1 < 1+2b\eta_k\frac{1}{1+\left|a+2bx_k\right|} < 1 \tag{100}$$

it can be concluded that

$$\left|\gamma^T \frac{\partial S(x_{k+1})}{\partial x_{k+1}}\right| < \left|\gamma^T \frac{\partial S(x_k)}{\partial x_k}\right| \tag{101}$$

The inequality in (100) holds if η_k is chosen, such that

$$\eta_k = \frac{\xi}{1+2|b|} \text{ where: } -1 < \xi < 0 \tag{102}$$

As a result, designing an appropriate η_k using (102) leads to (101) holding true, which means the derivative of states converges to zero asymptotically. This means the operating point of the system will converge to x_k^* with an exponential rate. ■

Furthermore, the proposed method is based on estimating the unknown parameter, $\gamma = \begin{bmatrix} a & b \end{bmatrix}^T$, where γ is estimated using the least square method (87) that is proven to be the most robust solution in system identification when the unknown function is LIP. In this work, using the Lyapunov theorem, we guarantee that the desired state trajectory converges to MPP, while the γ

can vary due to the PV ambient conditions. Therefore, the proposed method is robust against the parameter variation.

G. Result and Discussion

The proposed controller is implemented and verified experimentally. The proposed PV grid-tied system using ZSI in Fig. 42 is evaluated according to several factors: the accuracy of tracking MPP, the extent of oscillation around the MPP, the dynamic response to varying ambient condition, quality of the injected current to the grid, injecting the maximum harvested power from the PV panel to the grid and operation at unity power factor. A PV emulator is used to emulate the I-V and P-V characteristic curves of a SUNPOWER SPR-305-WHT-U for the experiments. The control scheme is implemented on a dSPACE 1006 platform for the system test, the use of this embedded system is intended for expedited prototyping, but many cheaper boards is capable of handling the proposed controller. The switching devices used for ZSI are C3M0075120J for Inverter Bridge and C4D15120D for the diode. The current and voltage sensors are CAS 25-NP and LV25-600 respectively. A programmable bidirectional AC power source (Regenerative Grid Simulator) is used as the grid in the experiments.

The detail design of impedance network components is beyond the scope of this paper, several methods provided in literature to design the components in the impedance network of z-source inverters as [117]. In summary, the complete list of implemented system parameters for the experiments are given by Table I. Due to nature of MPC, the switching frequency is variable, in this experiment, for the sampling time 60 μs, the average switching frequency is around 9 kHz in steady state operation. Execution time measurements shows that the proposed MPC algorithm requires 25 μs which is feasible by most commercially available micro-controllers.

To begin the analysis, the operation of system with solar irradiance of 750 W/m^2 is evaluated.

The results for this experiment are shown by the scope shots of Fig. 46 and Fig. 47. The three phase grid side current and the inductor L_1 current of the impedance network at the PV side are shown in Fig. 46. As it is shown by the inductor L_1 current, the average current drawn from the PV panel is 4.1 A with 0.2 A current ripple where the expected PV array current at MPP is 4.2 A for 750 W/m^2 solar irradiance according to the PV array characteristic curves. Thus, the proposed system is accurately tracking the MPP. The waveforms of the three phase injected current to the grid are given in Fig. 46. As it is shown, the injected current to grid has negligible harmonic distortions. The individual harmonic distortion contents of the phase (a) grid current are tabulated in Table VII. The Total Harmonic Distortion (THD) of the injected grid current is 2.92% which is within IEEE-519 grid codes and standards. Fig. 47 demonstrates the unity power factor operation of the system and the pulsating dc-link voltage. The pulsating dc-link voltage demonstrates the operation of ZSI in shoot through (when the dc-link voltage is zero) and non-shoot through (when the dc-link voltage is non-zero) sates.

The second experiments evaluates the dynamic response of the system to a step change in solar irradiance from 1000 W/m2 to 750 W/m2 . Fig. 48, Fig. 49, and Fig. 50 demonstrate the system performance for this experiment. The system is initially operating at solar irradiance of 1000 W/m2 , then at instant t1, the solar irradiance is step changed from 1000 W/m2 to 750 W/m2 . Fig. 48 shows the dynamic response of the inductor L_1 current and the three phase injected current to the grid. At the PV side, as it is shown by inductor L_1 current, the controller tracks the new MPP fast, without significant overshoot/undershoot. At the grid side, the system reaches to its new operating point around 50 ms after the step change occurred at instant t_1. The injected currents to the grid do not show any inrush effect due to step change in solar irradiance. Fig. 49 illustrates the effect of solar irradiance change on unity power factor operation of the system. As it is captured in Fig. 49,

the system is injecting the current into the grid with smooth reduction in the grid peak current without change in its phase to maintain unity power factor operation. The effect of this step change in solar irradiance on capacitor C_1 voltage in the impedance network is shown in Fig. 50. As it is captured, the change in solar irradiance has minor effects on the C_1 voltage as it is expected according to the PV characteristics curve when there is a change in solar irradiance.

Finally, the response of the system to a step change in the ambient temperature of the PV panel is evaluated for a step of 25℃ to 50℃. The system performance for this experiment is shown in Fig. 51. As it is captured, after the step change at instant t_2, the inductor L_1 current moves to its new MPP operation and coordinates very fast to extract the maximum available power from the PV array. This will results in lower peak current at grid side. The grid side current is changed smoothly without experiencing inrush current.

Fig. 52 illustrates the response of the proposed system to step change in solar irradiance while providing reactive power of 400 VAR for the grid. The solar irradiance is initially at 700 W/m2 , then at time t_3 the solar irradiance is stepped up to 1000 W/m2 . As pictured, this change causes an increase in the grid peak current and inductor L_1 current. The performance of the controller during a grid voltage sag event is tested next. The resulting waveforms are shown in the scope shots of Figs. 53 and 54. In this experiment, the system is initially operating with normal grid condition at unity power factor. Subsequently, at time instant t_4, the ZSI is triggered to inject 400 VAR reactive power into the grid. Later, at instant t_5 the grid voltage returns to normal condition, and the controller is triggered to return to unity power factor operation as shown in Fig. 54.

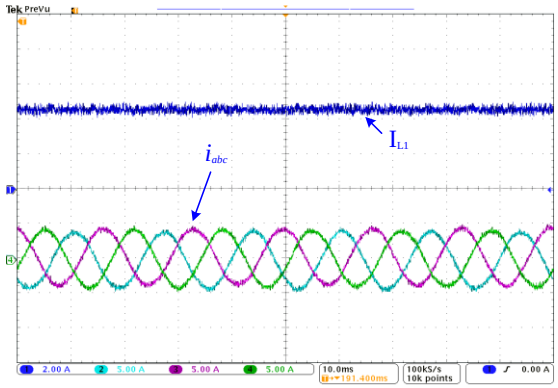

Fig. 46. System operation in steady state solar irradiance condition, the three phase grid side current and the inductor L1 current in the impedance network waveforms with 750 W/m^2 solar irradiance.

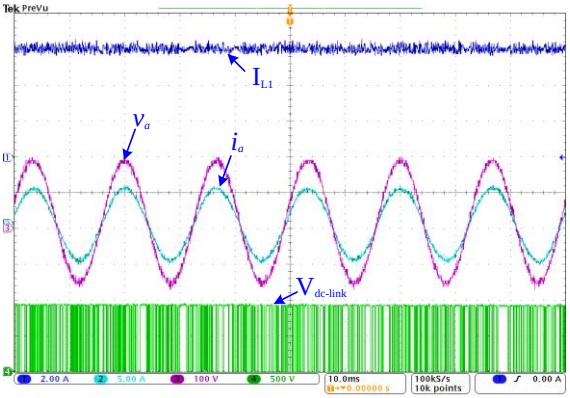

Fig. 47. System operation in steady state solar irradiance condition, phase (a) of grid voltage and current, pulsating dc-link voltage, and inductor L1 current in the impedance network with 1000 W/m^2 solar irradiance.

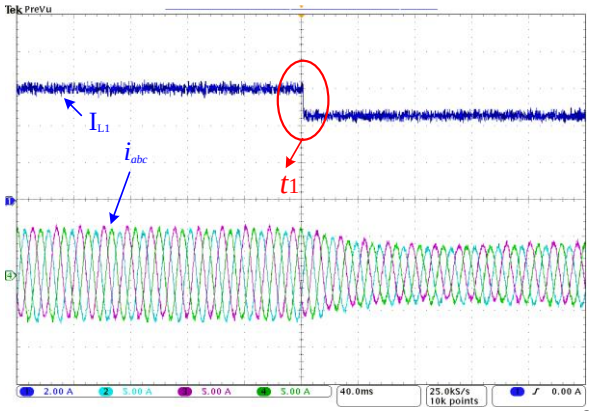

Fig. 48. Dynamic response of the system to step change in solar irradiance from 1000 W/m^2 to 750 W/m^2, the three phase grid side current and the inductor L1 current in the impedance network.

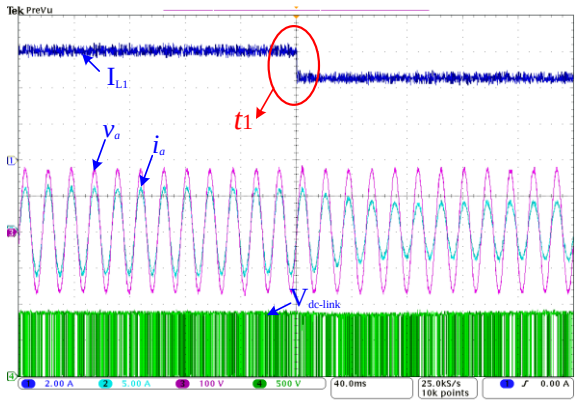

Fig. 49. Dynamic response of the system to step change in solar irradiance from 1000 W/m^2 to 750 W/m^2, phase (a) of grid voltage and current, pulsating dc-link voltage, and inductor L1 current in the impedance network.

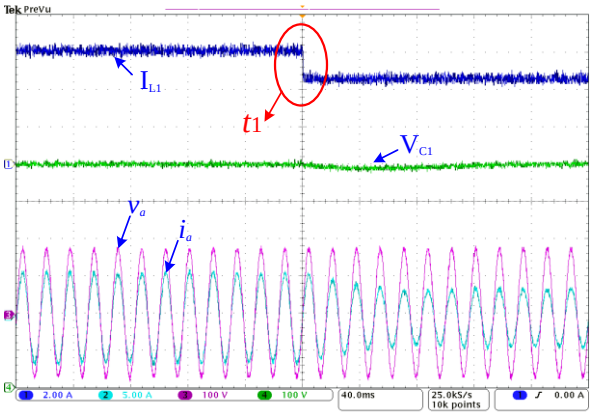

Fig. 50. Dynamic response of the system to step change in solar irradiance from 1000 W/m^2 to 750 W/m^2, capacitor C1 voltage and inductor L1 current in the impedance network, phase (a) of grid voltage and current.

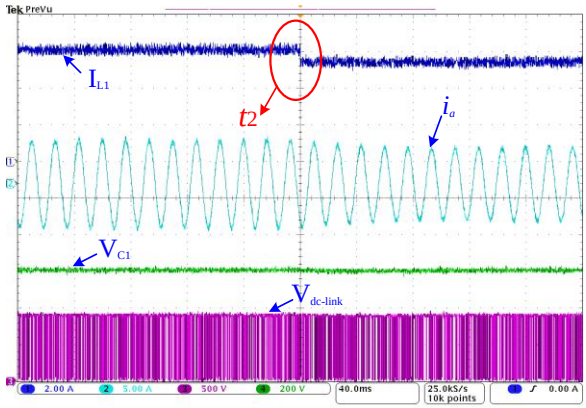

Fig. 51. Dynamic response of the system to step change in ambient temperature of the PV panel from 25 deg C to 50 deg C, capacitor C1 voltage and inductor L1 current in the impedance network, pulsating dc-link voltage, and phase (a) of grid current.

The injected current to grid has negligible harmonic distortions. The FFT spectrum analysis of the phase (a) of the grid current is shown in Fig. 55. The individual harmonic distortion contents of the phase (a) grid current are tabulated in Table VII. The Total Harmonic Distortion (THD) of

the injected grid current is 1.92% which is within IEEE-519 grid codes and standards. Fig. 56 shows the dynamic response of active and reactive power to step change in solar irradiance from 1000 W/m2 to 750 W/m2 at instant t1. As it is shown, the system response to this step change is fast without significant overshoot/undershoot. Although a step change in solar irradiance is not happening in realistic conditions, but this scenario is considered as the worst case situation for the proposed system evaluation in this paper.

In this paper, the robustness and performance of the proposed ESP-MPPT is analyzed for ±35% error (mismatch) in the impedance network model at the PV side of the system, the control efficacy at solar irradiance level of 1000 W/m^2 is calculated and plotted in Fig. 57. In this analysis, the error in the C_1 and L_1 models are assumed to be occurred concurrently, thus the worst case scenario is when there ±35% error in the models of C_1 and L_1 at the same time. The proposed MPPT controller efficacy is varying between 95.5% to 99.5% with the ZSI impedance network model parameter mismatch of up to ±35%. As it is shown in Fig. 57, even for the worst case scenario the controller has acceptable efficacy of 95.5%.

The performance of the proposed method is compared to P&O and Fuzzy algorithm experimentally. The generated data from these experiments are recorded using the DSP directly and plotted using MATLAB for better visualization and comparison. The P&O method are designed to perform at their best in terms of dynamic response and oscillations around MPP for ZSI. Fig. 58 (a) and (b) compares the performance of the proposed method vs. the P&O method. Fig. 58 (a) demonstrates the performance of the two methods when the temperature is stepped up from 25℃ to 75℃. Fig. 58 (b) compares the performance of the two methods when irradiance is stepped up from 700 W/m^2 to 1000 W/m^2. Fig. 58 (a) and (b) shows faster and more accurate response with negligible oscillation around MPP from the proposed method. According to this

figure, the proposed ESP-MPPT method maintains the PV voltage very close to the MPP voltage during the transient and regulates the PV current to the MPP current in a few seconds. Due to nature of predictive controllers which predicts the system behavior in a specified time horizon, the most significant advantage of the proposed technique is high accuracy tracking of gradually changing solar irradiance levels, a property absent in most well-known MPPT techniques such as P&O.

TABLE VII: Grid current harmonic distortions

Harmonics Order	Distortion (%)
3rd	0.52%
5th	0.05%
7th	0.51%
9th	0.28%
11th	0.25%
13th	0.19%
15th	0.12%
17th	0.11%

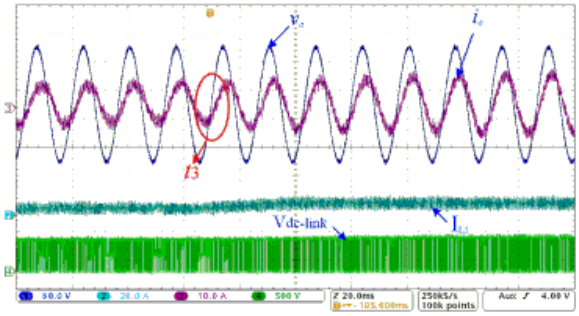

Fig. 52. Phase (a) of the grid voltage (va) and grid current, inductor L1 current (IL1), and pulsating dc-link voltage (Vdclink) with step change in solar irradiance level from 700 W/m2 to 1000 W/m2 at time t3 while 400 VAR reactive power is injected to the grid.

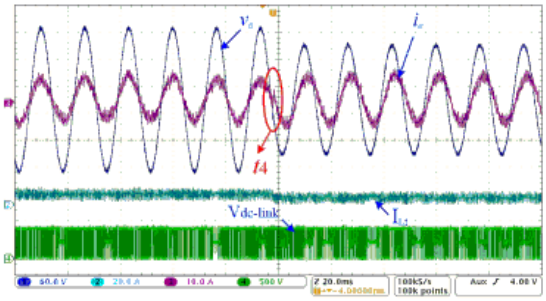

Fig. 53. Phase (a) of the grid voltage (va) and grid current, inductor L1 current (IL1), and pulsating dc-link voltage (Vdclink) when a 25% grid voltage sag occur at t4 and the system starts injecting reactive power of 400 VAR as an ancillary service.

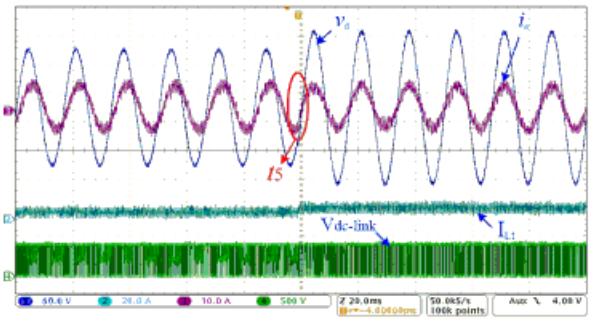

Fig. 54. Phase (a) of the grid voltage (va) and grid current, inductor L1 current (IL1), and pulsating dc-link voltage (Vdc-link) when the grid goes back to normal condition at t5 and the systems return to unity power factor operation.

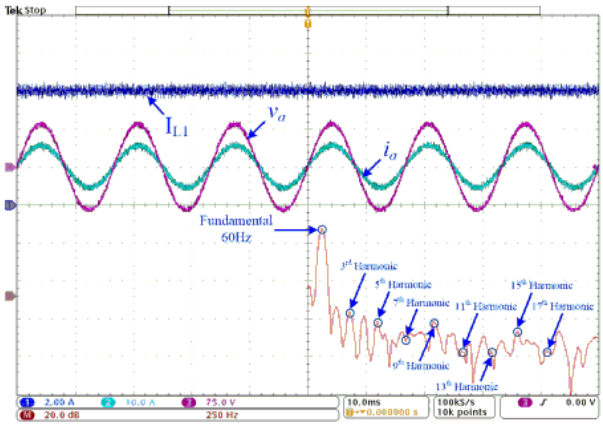

Fig. 55. FFT spectrum analysis of the phase "a" of the grid current.

Fig. 59 compares the performance of the proposed method versus the Fuzzy algorithm. Fig. 59 (a) demonstrates the performance of the two methods when the temperature is stepped down from 25℃ to 75℃. According to this figure the proposed method performs similar to the Fuzzy method. Fig. 59 (b) compares the performance of the two methods when irradiance is stepped up from 700 W/m^2 to 1000 W/m^2. According to this figure, the proposed method maintains the voltage very close to the MPP voltage during the transient and regulates the current to the MPP current in a few seconds. The performance of the Fuzzy method is mostly comparable to the proposed ESP-MPPT method in terms of convergence speed, however, the Fuzzy method increases the voltage for a short period of time during the transient which degrades its performance

slightly. Furthermore, the Fuzzy method effectiveness depends a lot on knowledge of the user or control engineer in choosing the right error computation and coming up with the rule base table, thus the design complexity is considered high in literature [5].

It worth mentioning that ZSI operates differently than conventional VSI/CSI. Using traditional control techniques for ZSI appears to be challenging since several cascaded loops are required [132, 133]. However the proposed ESP-MPPT in model predictive control frame achieves high performance MPP operation while keeping the design very simple through tackling a cost function subject to minimization. This is another reason that signifies the advantages of the proposed method for ZSI PV energy harvesting system.

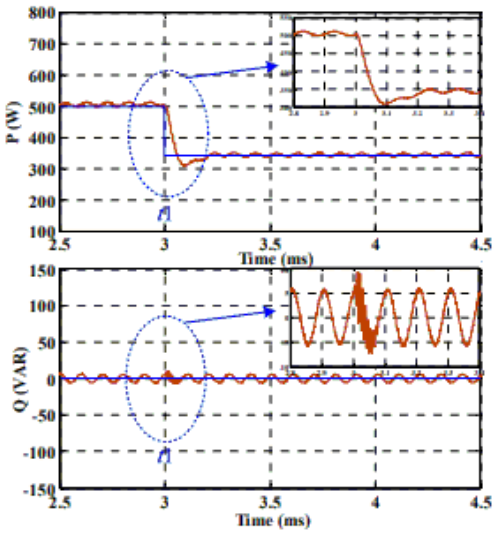

Fig. 56. System response to step change in solar irradiance from 1000 W/m2 to 750 W/m2 and unity power factor operation, the measured active and reactive power (orange waveform) and reference active and reactive power (blue waveform).

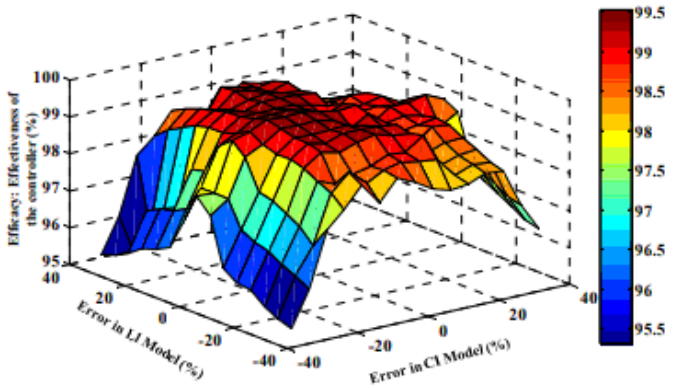

Fig. 57. Effect of ZSI model parameter mismatch on the proposed extremum seeking predictive MPPT technique efficacy (controller effectiveness).

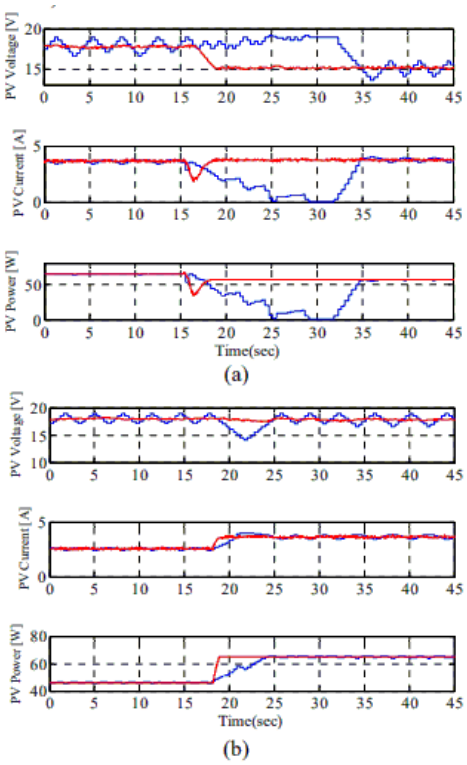

Fig. 58. (a) performance comparison of ESP-MPPT method (red curve) vs. the P&O method (blue curve) to step change in temperature (b) performance comparison of ESP-MPPT method (red curve) vs. the P&O method (blue curve) to step change in irradiance

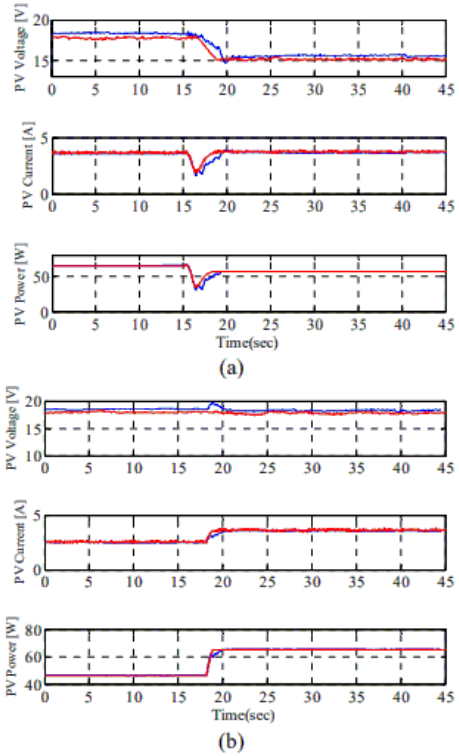

Fig. 59. (a) performance comparison of ESP-MPPT method (red curve) vs. the Fuzzy method (blue curve) to step change in temperature (b) performance comparison of ESP-MPPT method (red curve) vs. the Fuzzy method (blue curve) to step change in irradiance

H. Conclusion

This paper proposed a single stage PEI based on impedance source inverter for PV applications

with the capability to converge to true MPP operation. A new discrete-in-time ES based predictive MPPT algorithm is proposed for PV power harvesting systems using ZSI. The mathematical proof of convergence of the proposed method was provided to guarantee its effectiveness for tracking the MPP. Several experimental results were provided to validate the operation of the proposed method. The results demonstrate the proposed controller features: converges to true MPP with average tracking efficacy of 98.8% in steady state PV ambient condition, fast dynamic response to change in ambient condition of PV module, robust operation, high power quality injection, negligible overshoot/undershoot in grid current injection due to change in PV ambient condition, and no observation of inrush current during dynamic change operation. The proposed system has negligible current and voltage ripple in the impedance network; although the proposed controller can be used for other converters, its advantages will signify when used with a ZSI.

VI. FUTURE WORK

The current energy consumption structure's ongoing severe overreliance on fossil fuels, such as coal, natural gas, crude oil, and natural gas plant liquids, has raised two major potential concerns: the eventual development of an energy resource deficiency crisis and the onset of global warming due to greenhouse gas emissions. These issues have, in part, spurred on the rapid development of distributed generation (DG) systems and grid of nano-grids, which incorporate renewable energy sources and energy storage systems in distributed manner. As a result, the notion of a future smart grid of nano-grids in which modern sensors, communication links, and computational power can be used to improve the grid's flexibility and functionality is becoming popular among power and energy engineers. While the idea of a grid of nano-grids seems appealing at first, researchers must address several issues before they can implement this idea. The stability, protection, power quality, economic operation, active management, communication, and control of smart grids currently constitute the popular topics among the power society, most of which are still considered open problems. I find the problem of optimal operation of PEIs in smart grid of nano-grids, dynamic modeling, and control quite interesting because the future smart grid of nano-grids will be a nonlinear and complex system with extremely convoluted dynamics.

The future work of this dissertation is on advanced hierarchal control structure of the PEIs with advance functionalities in smart grid of nano-grids. The main aim of this future work is to develop an innovative and advanced highly reliable, efficient, and stable controller for the nano-grids to enable a high penetration of distrusted generation into the grid. The primary task involved in controlling the grid is balancing, or matching electrical generation with power consumption. Currently, electrical generation is adjusted to match a demand profile consisting of a large peak in

the afternoon and a valley at night. However, as the generation mix evolves from controlled central generation towards including more uncontrolled, distributed, renewable generation, grid operators require new algorithms to rapidly regulate loads to generation on the grid. An advanced control schemes will be investigated; including model based digital distributed control, to actively configure the grid topology to match loads with distributed generation and energy storage. Methods to have bump-less power generation in the system considering high penetration renewables using the proposed ZSI based energy harvesting system will be investigated. Additionally, the dynamic modeling of the grid of nano-grids with multiple PEI with advance functionalities will be studied.

VII. CONCLUSION

This work proposes predictive control for ZSI based PV energy harvesting systems. In the first part of the work, a highly efficient control scheme for a ZSI based grid-tied PV system is proposed. The presented control system has two components: The proposed model predictive based MPPT, and the grid side power injection controller. The model predictive based MPPT is proposed for tracking the MPP of the PV module. The proposed technique predicts the future values of the PV voltages and currents using a digital observer that estimates the values of the equivalent voltage and resistance of the PV module at any operating point. The perturbation size in PV voltage is adaptively predicted to determine the desirable trajectory PV voltage for the developed cost function, thus high control effectiveness is achieved from low to high solar irradiance level. The power injection control system uses the reference values generated by the MPPT system to control operation of the ZSI system while keeping the voltage stress on the converter switches at the lowest possible value. The experimental results provided demonstrate low THD of the grid side current that is within the IEEE 519 standards, fast dynamic response to a step change in solar irradiance level, and negligible oscillations around MPP under dynamically changing sky condition.

In the second part of the work, a MPC technique is proposed for a dual-mode ZSI with seamless transition between grid-connection and islanding mode without significant deviation in voltage and current due to mismatch in phase, frequency, and amplitude of grid voltage and load. The proposed single loop controller determines the optimal switching states for the ZSI based on its mode of operation. A single hybrid cost function is developed for all modes of operation which simplifies the design and practical implementation of the proposed model based predictive controller. This characteristic of the proposed system is well suited for the impedance source inverters which require advance and complex modulation scheme due to their shoot-through state

in addition to active and null states. The hybrid cost function is optimized during each sampling time to: harvest the maximum power from the PV module, inject the active power to the grid, provide reactive power compensation for the grid as an ancillary service to the grid through PCC, and maintain the PCC voltage in the islanded mode. The explanation of system modes of operation, strategy to transit between modes of operation, and operation in steady state modes are provided. Several experimental case studies are provided to validate the theoretical expectations. The results demonstrate robust operation in all modes of operation. The main features of the proposed controller are high quality grid current in grid connected mode, fast dynamic response in grid-connected mode to step change in active and reactive power, negligible power ripple in steady state operation, seamless transition between modes of operation without significant deviation in PCC voltage and current, robust operation under distorted grid voltage, and capability to operate at different frequency in islanded mode of operation.

The final part of this dissertation presents a simple control strategy with an adaptive cost function to seamlessly operate under normal and faulty grid condition. The proposed system eliminates the requirements of multi-nested-loop of classical controller. Due to the predictive nature of the controller, the proposed system has fast dynamic response to change in solar irradiance or grid reactive power requirement according to LVRT operation. The system is switching between LVRT and MPPT modes of operation seamlessly. The proposed system can be extended for overnight operation of PV sources in DGs with reactive power compensation capability as ancillary service from DG to main grid.

VIII. REFERENCES

[1] S. Esterly and R. Gelman, "2013 Renewable Energy Data Book," U. S. D. Energy, Ed., ed. United States: U.S. Department of Energy's National Renewable Energy Laboratory (NREL), 2013.

[2] F. Blaabjerg, Y. Yongheng, and M. Ke, "Power electronics - Key technology for renewable energy systems - Status and future," in *IEEE International Conference on Electric Power and Energy Conversion Systems (EPECS)*, 2013, pp. 1-6.

[3] H. Abu-Rub, M. Malinowski, and K. Al-Haddad, *Power electronics for renewable energy systems, transportation and industrial applications*: John Wiley & Sons, 2014.

[4] S. Kouro, J. I. Leon, D. Vinnikov, and L. G. Franquelo, "Grid-Connected Photovoltaic Systems: An Overview of Recent Research and Emerging PV Converter Technology," *IEEE Industrial Electronics Magazine,* vol. 9, pp. 47-61, 2015.

[5] T. Esram and P. L. Chapman, "Comparison of Photovoltaic Array Maximum Power Point Tracking Techniques," *IEEE Transactions on Energy Conversion,* vol. 22, pp. 439-449, 2007.

[6] L. Poh Chiang, D. M. Vilathgamuwa, L. Yue Sen, C. Geok Tin, and L. Yunwei, "Pulse-width modulation of Z-source inverters," *IEEE Transactions on Power Electronics,* vol. 20, pp. 1346-1355, 2005.

[7] S. Miaosen, A. Joseph, W. Jin, F. Z. Peng, and D. J. Adams, "Comparison of Traditional Inverters and Z -Source Inverter for Fuel Cell Vehicles," *IEEE Transactions on Power Electronics,* vol. 22, pp. 1453-1463, 2007.

[8] P. Fang Zheng, "Z-source inverter," *IEEE Transactions on Industry Applications, ,* vol. 39, pp. 504-510, 2003.

[9] Y. P. Siwakoti, P. Fang Zheng, F. Blaabjerg, L. Poh Chiang, and G. E. Town, "Impedance-Source Networks for Electric Power Conversion Part I: A Topological Review," *IEEE Transactions on Power Electronics,* vol. 30, pp. 699-716, 2015.

[10] Y. P. Siwakoti, P. Fang Zheng, F. Blaabjerg, L. Poh Chiang, G. E. Town, and Y. Shuitao, "Impedance-Source Networks for Electric Power Conversion Part II: Review of Control and Modulation Techniques," *IEEE Transactions on Power Electronics,* vol. 30, pp. 1887-1906, 2015.

[11] D. Vinnikov and I. Roasto, "Quasi-Z-Source-Based Isolated DC-DC Converters for Distributed Power Generation," *IEEE Transactions on Industrial Electronics, ,* vol. 58, pp. 192-201, 2011.

[12] A. Ravindranath, S. K. Mishra, and A. Joshi, "Analysis and PWM Control of Switched Boost Inverter," *IEEE Transactions on Industrial Electronics, ,* vol. 60, pp. 5593-5602, 2013.

[13] Y. Keping and M. F. Rahman, "A Matrix Z-Source Converter With AC-DC Bidirectional Power Flow for an Integrated Starter Alternator System," *IEEE Transactions on Industry Applications, ,* vol. 45, pp. 239-248, 2009.

[14] N. Minh-Khai, J. Young-Gook, and L. Young-cheol, "Single-Phase AC-AC Converter Based on Quasi-Z-Source Topology," *IEEE Transactions on Power Electronics, ,* vol. 25, pp. 2200-2210, 2010.

[15] G. Baoming, L. Qin, Q. Wei, and P. Fang Zheng, "A Family of Z-Source Matrix Converters," *IEEE Transactions on Industrial Electronics,* vol. 59, pp. 35-46, 2012.

[16] L. Liming, L. Hui, Z. Yi, H. Xiangning, and Z. J. Shen, "1 MHz cascaded Z-source inverters for scalable grid-interactive photovoltaic (PV) applications using GaN device," in *IEEE Energy Conversion Congress and Exposition (ECCE)*, 2011, pp. 2738-2745.

[17] P. Van den Heever, S. Oberholzer, and J. Enslin, "High-efficient solar panel/wind turbine converter with maximal power control," in *Proc. Eur. Conf. Power Electron. Appl*, 1989, pp. 663-668.

[18] J. Applebaum, "The quality of load matching in a direct-coupling photovoltaic system," *IEEE Transactions on Energy Conversion, ,* pp. 534-541, 1987.

[19] A. Braunstein, "On the dynamic optimal coupling of a solar cell array to a load and storage batteries," *IEEE Transactions on Power Apparatus and Systems, ,* pp. 1183-1188, 1981.

[20] K. Y. Khouzam, "Optimum load matching in direct-coupled photovoltaic power systems-application to resistive loads," *IEEE Transactions on Energy Conversion, ,* vol. 5, pp. 265-271, 1990.

[21] A. Kislovski and R. Redl, "Maximum-power-tracking using positive feedback," in *IEEE Power Electronics Specialists Conference (PESC)*, 1994, pp. 1065-1068.

[22] S. Wolf and J. Enslin, "Economical, PV maximum power point tracking regulator with simplistic controller," in *IEEE Power Electronics Specialists Conference (PESC)* 1993, pp. 581-587.

[23] C. R. Sullivan and M. J. Powers, "A high-efficiency maximum power point tracker for photovoltaic arrays in a solar-powered race vehicle," in *24th Annual IEEE Power Electronics Specialists Conference (PESC)*, 1993, pp. 574-580.

[24] Z. Salameh and D. Taylor, "Step-up maximum power point tracker for photovoltaic arrays," *Solar energy*, vol. 44, pp. 57-61, 1990.

[25] J. Gow and C. Manning, "Controller arrangement for boost converter systems sourced from solar photovoltaic arrays or other maximum power sources," *IEE Proceedings-Electric Power Applications*, vol. 147, pp. 15-20, 2000.

[26] M. Godoy Simões and N. Franceschetti, "A RISC-microcontroller based photovoltaic system for illumination applications," in *IEEE Applied Power Electronics Conference and Exposition (APEC)*, 2000, pp. 1151-1156.

[27] J. H. Enslin, M. S. Wolf, D. B. Snyman, and W. Swiegers, "Integrated photovoltaic maximum power point tracking converter," *IEEE Transactions on Industrial Electronics*, , vol. 44, pp. 769-773, 1997.

[28] A. F. Boehringer, "Self-Adapting dc Converter for Solar Spacecraft Power Supply " *IEEE Transactions on Aerospace and Electronic Systems,*, vol. AES-4, pp. 102-111, 1968.

[29] K. Hussein, I. Muta, T. Hoshino, and M. Osakada, "Maximum photovoltaic power tracking: an algorithm for rapidly changing atmospheric conditions," *IEEE Proceedings-Generation, Transmission and Distribution*, vol. 142, pp. 59-64, 1995.

[30] A. E. S. A. Nafeh, F. H. Fahmy, O. A. Mahgoub, and E. M. Abou El-Zahab, "Microprocessor control system for maximum power operation of PV arrays," *International Journal of Numerical Modelling: Electronic Networks, Devices and Fields*, vol. 12, pp. 187-195, 1999.

[31] O. Wasynezuk, "Dynamic Behavior of a Class of Photovoltaic Power Systems," *IEEE Transactions on Power Apparatus and Systems*, , vol. PAS-102, pp. 3031-3037, 1983.

[32] J. Schoeman and J. v. Wyk, "A simplified maximal power controller for terrestrial photovoltaic panel arrays," in *IEEE Power Electronics Specialists conference (PESC)*, 1982, pp. 361-367.

[33] S. Yuvarajan and X. Shanguang, "Photo-voltaic power converter with a simple maximum-power-point-tracker," in *Proceedings of the international symposium on circuits and systems* 2003, pp. III-399-III-402 vol.3.

[34] M. El-Shibini and H. Rakha, "Maximum power point tracking technique," in *Electrotechnical Conference, 1989. Proceedings.'Integrating Research, Industry and Education in Energy and Communication Engineering', MELECON'89., Mediterranean*, 1989, pp. 21-24.

[35] P. Ching-Tsai, C. Jeng-Yue, C. Chin-Peng, and H. Yi-Shuo, "A fast maximum power point tracker for photovoltaic power systems," in *Annual Conference of the IEEE Industrial Electronics Society (IECON)*, 1999, pp. 390-393 vol.1.

[36] Y. Gwon-Jong, J. Myung-woong, S. Jinsoo, C. In-Su, and H. In-Ho, "Maximum power point tracking with temperature compensation of photovoltaic for air conditioning system with fuzzy controller," in *IEEE Photovoltaic Specialist Conference (PVSC)*, 1996, pp. 1429-1432.

[37] K. Ro and S. Rahman, "Two-loop controller for maximizing performance of a grid-connected photovoltaic-fuel cell hybrid power plant,", *IEEE transactions on Energy Conversion, ,* vol. 13, pp. 276-281, 1998.

[38] T. Kitano, M. Matsui, and D.-h. Xu, "Power sensor-less MPPT control scheme utilizing power balance at DC link-system design to ensure stability and response," in *Annual Conference of the IEEE Industrial Electronics Society (IECON)*, 2001, pp. 1309-1314.

[39] G. Hart, H. Branz, and C. Cox, "Experimental tests of open-loop maximum-power-point tracking techniques for photovoltaic arrays," *Solar cells,* vol. 13, pp. 185-195, 1984.

[40] F. Huang, G. Zhimin, T. Forughian, and D. Tien, "A new microcontroller based solar energy conversion modular unit," in *Power Conversion Conference*, 1997, pp. 697-700.

[41] M. Matsui, T. Kitano, and D. Xu, "A simple maximum photovoltaic power tracking technique utilizing system inherent limit cycle phenomena," in *IEEE Industry Application Society (IAS) Annual Meeting* 2003, pp. 2041-2047.

[42] T. Ouchi, H. Fujikawa, S. Masukawa, and S. Iida, "A control scheme for three-phase current source inverter in interactive photovoltaic system," *TRANSACTIONS-INSTITUTE OF ELECTRICAL ENGINEERS OF JAPAN D*, vol. 120, pp. 230-239, 2000.

[43] T. Kitano, M. Matsui, and D. Xu, "A maximum power point tracking control scheme for PV system based on power equilibrium and its system design," *TRANSACTIONS-INSTITUTE OF ELECTRICAL ENGINEERS OF JAPAN D,* vol. 121, pp. 1263-1269, 2001.

[44] H. Dong, H. Sugimoto, and N. Nishio, "A maximum power tracking control method for photovoltaic power generation system based on derivation of output power with respect to output voltage," *TRANSACTIONS-INSTITUTE OF ELECTRICAL ENGINEERS OF JAPAN D,* vol. 118, pp. 1435-1442, 1998.

[45] Corte, x, P. s, A. Wilson, S. Kouro, J. Rodriguez, *et al.*, "Model Predictive Control of Multilevel Cascaded H-Bridge Inverters," *IEEE Transactions on Industrial Electronics, ,* vol. 57, pp. 2691-2699, 2010.

[46] J. Rodriguez, M. P. Kazmierkowski, J. R. Espinoza, P. Zanchetta, H. Abu-Rub, H. A. Young, *et al.*, "State of the Art of Finite Control Set Model Predictive Control in Power Electronics," *IEEE Transactions on Industrial Informatics, ,* vol. 9, pp. 1003-1016, 2013.

[47] T. Geyer and D. E. Quevedo, "Multistep Finite Control Set Model Predictive Control for Power Electronics," *IEEE Transactions on Power Electronics,* vol. 29, pp. 6836-6846, 2014.

[48] M. B. Shadmand, L. Xiao, R. S. Balog, and H. Abu Rub, "Model predictive control of grid-tied photovoltaic systems: Maximum power point tracking and decoupled power control," in *Smart Grid and Renewable Energy (SGRE), 2015 First Workshop on*, 2015, pp. 1-6.

[49] W. Mo, A. P. C. Loh, and B. Frede, "Maximum power point tracking technique implementation of Z-source inverter through finite step model predictive control strategy," in *Industrial Electronics and Applications (ICIEA), 2012 7th IEEE Conference on*, 2012, pp. 1523-1528.

[50] W. Mo, P. C. Loh, and F. Blaabjerg, "Model predictive control for Z-source power converter," in *Power Electronics and ECCE Asia (ICPE & ECCE), 2011 IEEE 8th International Conference on*, 2011, pp. 3022-3028.

[51] M. B. Shadmand, R. S. Balog, and H. Abu-Rub, "Model Predictive Control of PV Sources in a Smart DC Distribution System: Maximum Power Point Tracking and Droop Control," *Energy Conversion, IEEE Transactions on,* vol. 29, pp. 913-921, 2014.

[52] G. Baoming, H. Abu-Rub, L. Yushan, and R. S. Balog, "Minimized Quasi-Z source network for single-phase inverter," in *Applied Power Electronics Conference and Exposition (APEC), 2015 IEEE*, 2015, pp. 806-811.

[53] H. Yi, S. Miaosen, F. Z. Peng, and W. Jin, "Z-Source Inverter for Residential Photovoltaic Systems," *IEEE Transactions on Power Electronics,*, vol. 21, pp. 1776-1782, 2006.

[54] C. J. Gajanayake, D. M. Vilathgamuwa, and L. Poh Chiang, "Development of a Comprehensive Model and a Multiloop Controller for Z-Source Inverter DG Systems," *Industrial Electronics, IEEE Transactions on*, vol. 54, pp. 2352-2359, 2007.

[55] O. Ellabban, J. Van Mierlo, and P. Lataire, "A DSP-Based Dual-Loop Peak DC-link Voltage Control Strategy of the Z-Source Inverter," *IEEE Transactions on Power Electronics*, vol. 27, pp. 4088-4097, 2012.

[56] L. Yuan, J. Shuai, J. G. Cintron-Rivera, and P. Fang Zheng, "Modeling and Control of Quasi-Z-Source Inverter for Distributed Generation Applications," *Industrial Electronics, IEEE Transactions on*, vol. 60, pp. 1532-1541, 2013.

[57] S. A. Saleh, A. S. Aljankawey, E. Ozkop, and R. Meng, "On the Experimental Performance of a Coordinated Antiislanding Protection for Systems With Multiple DGUs," *IEEE Transactions on Power Electronics*, vol. 32, pp. 1106-1123, 2017.

[58] K. O. Oureilidis and C. S. Demoulias, "A Fault Clearing Method in Converter-Dominated Microgrids With Conventional Protection Means," *IEEE Transactions on Power Electronics*, vol. 31, pp. 4628-4640, 2016.

[59] F. Liu, W. Liu, X. Zha, H. Yang, and K. Feng, "Solid-State Circuit Breaker Snubber Design for Transient Overvoltage Suppression at Bus Fault Interruption in Low-Voltage DC Microgrid," *IEEE Transactions on Power Electronics*, vol. 32, pp. 3007-3021, 2017.

[60] H. T. Do, X. Zhang, N. V. Nguyen, S. S. Li, and T. T. T. Chu, "Passive-Islanding Detection Method Using the Wavelet Packet Transform in Grid-Connected Photovoltaic Systems," *IEEE Transactions on Power Electronics*, vol. 31, pp. 6955-6967, 2016.

[61] C. Li, J. Savulak, and R. Reinmuller, "Unintentional Islanding of Distributed Generation-Operating Experiences From Naturally Occurred Events," *IEEE Transactions on Power Delivery*, vol. 29, pp. 269-274, 2014.

[62] J. He, Y. W. Li, and F. Blaabjerg, "An Enhanced Islanding Microgrid Reactive Power, Imbalance Power, and Harmonic Power Sharing Scheme," *IEEE Transactions on Power Electronics,* vol. 30, pp. 3389-3401, 2015.

[63] K. T. Tan, P. L. So, Y. C. Chu, and M. Z. Q. Chen, "Coordinated Control and Energy Management of Distributed Generation Inverters in a Microgrid," *IEEE Transactions on Power Delivery,* vol. 28, pp. 704-713, 2013.

[64] J. K. Pedersen, M. Akke, N. K. Poulsen, and K. O. H. Pedersen, "Analysis of wind farm islanding experiment," *IEEE Transactions on Energy Conversion,* vol. 15, pp. 110-115, 2000.

[65] M. E. Ropp, M. Begovic, A. Rohatgi, G. A. Kern, R. H. Bonn, and S. Gonzalez, "Determining the relative effectiveness of islanding detection methods using phase criteria and nondetection zones," *IEEE Transactions on Energy Conversion,* vol. 15, pp. 290-296, 2000.

[66] A. Woyte, R. Belmans, and J. Nijs, "Testing the islanding protection function of photovoltaic inverters," *IEEE Transactions on Energy Conversion,* vol. 18, pp. 157-162, 2003.

[67] J. M. Bloemink and M. R. Iravani, "Control of a Multiple Source Microgrid With Built-in Islanding Detection and Current Limiting," *IEEE Transactions on Power Delivery,* vol. 27, pp. 2122-2132, 2012.

[68] N. Eghtedarpour and E. Farjah, "Power Control and Management in a Hybrid AC/DC Microgrid," *IEEE Transactions on Smart Grid,* vol. 5, pp. 1494-1505, 2014.

[69] T. V. Tran, T. W. Chun, H. H. Lee, H. G. Kim, and E. C. Nho, "PLL-Based Seamless Transfer Control Between Grid-Connected and Islanding Modes in Grid-Connected Inverters," *IEEE Transactions on Power Electronics,* vol. 29, pp. 5218-5228, 2014.

[70] S. Moayedi and A. Davoudi, "Unifying Distributed Dynamic Optimization and Control of Islanded DC Microgrids," *IEEE Transactions on Power Electronics,* vol. 32, pp. 2329-2346, 2017.

[71] A. Bidram, V. Nasirian, A. Davoudi, and F. L. Lewis, "Control and Modeling of Microgrids," in *Cooperative Synchronization in Distributed Microgrid Control*, ed: Springer International Publishing, 2017, pp. 7-43.

[72] W. R. Issa, M. A. Abusara, and S. M. Sharkh, "Control of Transient Power During Unintentional Islanding of Microgrids," *IEEE Transactions on Power Electronics*, vol. 30, pp. 4573-4584, 2015.

[73] L. G. Meegahapola, D. Robinson, A. P. Agalgaonkar, S. Perera, and P. Ciufo, "Microgrids of Commercial Buildings: Strategies to Manage Mode Transfer From Grid Connected to Islanded Mode," *IEEE Transactions on Sustainable Energy,* vol. 5, pp. 1337-1347, 2014.

[74] D. Dong, T. Thacker, I. Cvetkovic, R. Burgos, D. Boroyevich, F. Wang, *et al.*, "Modes of Operation and System-Level Control of Single-Phase Bidirectional PWM Converter for Microgrid Systems," *IEEE Transactions on Smart Grid,* vol. 3, pp. 93-104, 2012.

[75] G. Hernandez-Gonzalez and R. Iravani, "Current injection for active islanding detection of electronically-interfaced distributed resources," *IEEE Transactions on Power Delivery,* vol. 21, pp. 1698-1705, 2006.

[76] D. S. Ochs, B. Mirafzal, and P. Sotoodeh, "A method of seamless transitions between grid-tied and stand-alone modes of operation for utility-interactive three-phase inverters," *IEEE Transactions on Industry Applications,* vol. 50, pp. 1934-1941, 2014.

[77] Q.-C. Zhong; and T. Hornik;, "Cascaded current–voltage control to improve the power quality for a grid-connected inverter with a local load," *IEEE Transactions on Industrial Electronics,* vol. 60, pp. 1344-1355, 2013.

[78] Z. Yao, L. Xiao, and Y. Yan, "Seamless transfer of single-phase grid-interactive inverters between grid-connected and stand-alone modes," *IEEE Transactions on Power Electronics,* vol. 25, pp. 1597-1603, 2010.

[79] R.-J. Wai, C.-Y. Lin, Y.-C. Huang, and Y.-R. Chang, "Design of high-performance stand-alone and grid-connected inverter for distributed generation applications," *IEEE Transactions on Industrial Electronics,* vol. 60, pp. 1542-1555, 2013.

[80] Y. W. Cho, W. J. Cha, J. M. Kwon, and B. H. Kwon, "Improved single-phase transformerless inverter with high power density and high efficiency for grid-connected photovoltaic systems," *IET Renewable Power Generation,* vol. 10, pp. 166-174, 2016.

[81] X. Q. Guo and W. Y. Wu, "Improved current regulation of three-phase grid-connected voltage-source inverters for distributed generation systems," *IET Renewable Power Generation,* vol. 4, pp. 101-115, 2010.

[82] M. Hosseinzadeh and F. R. Salmasi, "Power management of an isolated hybrid AC/DC micro-grid with fuzzy control of battery banks," *IET Renewable Power Generation,* vol. 9, pp. 484-493, 2015.

[83] M. B. Shadmand, M. Mosa, R. S. Balog, and H. Abu-Rub, "Model Predictive Control of a Capacitorless Matrix Converter-Based STATCOM," *IEEE Journal of Emerging and Selected Topics in Power Electronics,* vol. 5, pp. 796-808, 2017.

[84] A. Momeneh, M. Castilla, J. Miret, P. Mart, xed, and M. Velasco, "Comparative study of reactive power control methods for photovoltaic inverters in low-voltage grids," *IET Renewable Power Generation,* vol. 10, pp. 310-318, 2016.

[85] R. Chilipi, N. Al Sayari, K. Al Hosani, and A. R. Beig, "Control scheme for grid-tied distributed generation inverter under unbalanced and distorted utility conditions with power quality ancillary services," *IET Renewable Power Generation,* vol. 10, pp. 140-149, 2016.

[86] I. W. Group, "IEEE recommended practices and requirements for harmonic control in electrical power systems," *IEEE STD,* pp. 519-1992, 1992.

[87] "IEEE Standard for Interconnecting Distributed Resources with Electric Power Systems," *IEEE Std 1547-2003,* pp. 1-28, 2003.

[88] I. E. Commission, "Characteristics of the utility interface for photovoltaic (PV) systems," *Report of IEC,* vol. 61727, 2002.

[89] "IEEE Guide for Monitoring, Information Exchange, and Control of Distributed Resources Interconnected with Electric Power Systems," *IEEE Std 1547.3-2007,* pp. 1-160, 2007.

[90] F. P. Marafão, D. I. Brandão, A. Costabeber, and H. K. M. Paredes, "Multi-task control strategy for grid-tied inverters based on conservative power theory," *IET Renewable Power Generation,* vol. 9, pp. 154-165, 2014.

[91] H.-L. Jou, W.-J. Chiang, and J.-C. Wu, "Virtual inductor-based islanding detection method for grid-connected power inverter of distributed power generation system," *IET Renewable Power Generation,* vol. 1, pp. 175-181, 2007.

[92] T.-Z. Bei, "Accurate active islanding detection method for grid-tied inverters in distributed generation," *IET Renewable Power Generation,* vol. 11, pp. 1633-1639, 2017.

[93] Y. Yang, F. Blaabjerg, and H. Wang, "Low-Voltage Ride-Through of Single-Phase Transformerless Photovoltaic Inverters," *IEEE Transactions on Industry Applications*, vol. 50, pp. 1942-1952, 2014.

[94] C. Y. Tang, Y. T. Chen, and Y. M. Chen, "PV Power System With Multi-Mode Operation and Low-Voltage Ride-Through Capability," *IEEE Transactions on Industrial Electronics*, vol. 62, pp. 7524-7533, 2015.

[95] Y. Yang, F. Blaabjerg, H. Wang, M. G. Sim, xf, and es, "Power control flexibilities for grid-connected multi-functional photovoltaic inverters," *IET Renewable Power Generation*, vol. 10, pp. 504-513, 2016.

[96] Z. Shao, X. Zhang, F. Wang, R. Cao, and H. Ni, "Analysis and Control of Neutral-Point Voltage for Transformerless Three-Level PV Inverter in LVRT Operation," *IEEE Transactions on Power Electronics*, vol. 32, pp. 2347-2359, 2017.

[97] P. Fang Zheng, "Z-source inverter," *IEEE Transactions on Industry Applications*, vol. 39, pp. 504-510, 2003.

[98] Y. Tang, J. Wei, and S. Xie, "Grid-tied photovoltaic system with series Z-source inverter," *IET Renewable Power Generation*, vol. 7, pp. 275-283, 2013.

[99] D. Sun, B. Ge, X. Yan, D. Bi, H. Zhang, Y. Liu, *et al.*, "Modeling, Impedance Design, and Efficiency Analysis of Quasi- Z Source Module in Cascaded Multilevel Photovoltaic Power System," *IEEE Transactions on Industrial Electronics*, vol. 61, pp. 6108-6117, 2014.

[100] J. Rodriguez, M. P. Kazmierkowski, J. R. Espinoza, P. Zanchetta, H. Abu-Rub, H. A. Young, *et al.*, "State of the Art of Finite Control Set Model Predictive Control in Power Electronics," *IEEE Transactions on Industrial Informatics*, vol. 9, pp. 1003-1016, 2013.

[101] M. Mosa, M. B. Shadmand, R. S. Balog, and H. A. Rub, "Efficient maximum power point tracking using model predictive control for photovoltaic systems under dynamic weather condition," *IET Renewable Power Generation*, vol. 11, pp. 1401-1409, 2017.

[102] L. Yushan, G. Baoming, H. Abu-Rub, and P. Fang Zheng, "Overview of Space Vector Modulations for Three-Phase Z-Source/Quasi-Z-Source Inverters," *IEEE Transactions on Power Electronics*, vol. 29, pp. 2098-2108, 2014.

[103] P. Fang Zheng, S. Miaosen, and Q. Zhaoming, "Maximum boost control of the Z-source inverter," *IEEE Transactions on Power Electronics,*, vol. 20, pp. 833-838, 2005.

[104] S. Miaosen, W. Jin, A. Joseph, P. Fang Zheng, L. M. Tolbert, and D. J. Adams, "Constant boost control of the Z-source inverter to minimize current ripple and voltage stress," *IEEE Transactions on Industry Applications,* , vol. 42, pp. 770-778, 2006.

[105] S. Miaosen, W. Jin, A. Joseph, F. Z. Peng, L. M. Tolbert, and D. J. Adams, "Maximum constant boost control of the Z-source inverter," in *IEEE Industry Applications Conference*, , 2004, pp. 1-147.

[106] D. G. Holmes and T. A. Lipo, *Pulse width modulation for power converters: principles and practice* vol. 18: John Wiley & Sons, 2003.

[107] L. Jingbo, H. Jiangang, and X. Longya, "Dynamic Modeling and Analysis of Z Source Converter-Derivation of AC Small Signal Model and Design-Oriented Analysis," *IEEE Transactions on Power Electronics,* vol. 22, pp. 1786-1796, 2007.

[108] P. C. Krause, O. Wasynczuk, S. D. Sudhoff, and S. Pekarek, *Analysis of electric machinery and drive systems* vol. 75: John Wiley & Sons, 2013.

[109] "IEEE Recommended Practices and Requirements for Harmonic Control in Electrical Power Systems," *IEEE Std 519-1992,* pp. 1-112, 1993.

[110] S. Sajadian and R. Ahmadi, "Model Predictive Based Maximum Power Point Tracking for Grid-tied Photovoltaic Applications Using a Z-Source Inverter," *IEEE Transactions on Power Electronics,* vol. 31, pp. 7611-7620, November 2016.

[111] Z. Yao, L. Xiao, and J. M. Guerrero, "Improved control strategy for the three-phase grid-connected inverter," *IET Renewable Power Generation,* vol. 9, pp. 587-592, 2015.

[112] M. Ciobotaru, V. G. Agelidis, R. Teodorescu, and F. Blaabjerg, "Accurate and Less-Disturbing Active Antiislanding Method Based on PLL for Grid-Connected Converters," *IEEE Transactions on Power Electronics,* vol. 25, pp. 1576-1584, 2010.

[113] S. Dasgupta, S. K. Sahoo, and S. K. Panda, "Single-Phase Inverter Control Techniques for Interfacing Renewable Energy Sources With Microgrid-Part I: Parallel-Connected Inverter Topology With Active and Reactive Power Flow Control Along With Grid Current Shaping," *IEEE Transactions on Power Electronics,* vol. 26, pp. 717-731, 2011.

[114] Z. Qing-Chang, N. Phi-Long, M. Zhenyu, and S. Wanxing, "Self-Synchronized Synchronverters: Inverters Without a Dedicated Synchronization Unit," *IEEE Transactions on Power Electronics,* vol. 29, pp. 617-630, 2014.

[115] F. Xiao, L. Dong, L. Li, and X. Liao, "A Frequency-Fixed SOGI-Based PLL for Single-Phase Grid-Connected Converters," *IEEE Transactions on Power Electronics*, vol. 32, pp. 1713-1719, 2017.

[116] E. Pouresmaeil, C. Miguel-Espinar, M. Massot-Campos, D. Montesinos-Miracle, and O. Gomis-Bellmunt, "A Control Technique for Integration of DG Units to the Electrical Networks," *IEEE Transactions on Industrial Electronics*, vol. 60, pp. 2881-2893, 2013.

[117] H. Abu-Rub, Y. Liu, B. Ge, F. Blaabjerg, O. Ellabban, and P. C. Loh, *Impedance source power electronic converters*: John Wiley & Sons, 2016.

[118] H. Akagi, E. H. Watanabe, and M. Aredes, *Instantaneous power theory and applications to power conditioning* vol. 31: John Wiley & Sons, 2007.

[119] E. Netz, "Grid code; high and extra high voltage," *E-One Netz GmbH, Bayreuth*, vol. 4, 2006.

[120] K. O. Kovanen, "Photovoltaics and power distribution," *Renewable Energy Focus*, vol. 14, pp. 20-21, 5// 2013.

[121] T. Neumann and I. Erlich, "Modelling and control of photovoltaic inverter systems with respect to German grid code requirements," in *IEEE Power and Energy Society General Meeting*, 2012, pp. 1-8.

[122] J. E.-G. Carrasco, J. Tena, D. Ugena, J. Alonso-Martinez, D. Santos-Martin, and S. Arnaltes, "Testing low voltage ride through capabilities of solar inverters," *Electric Power Systems Research*, vol. 96, pp. 111-118, 2013.

[123] C. T. Lee, C. W. Hsu, and P. T. Cheng, "A Low-Voltage Ride-Through Technique for Grid-Connected Converters of Distributed Energy Resources," *IEEE Transactions on Industry Applications*, vol. 47, pp. 1821-1832, 2011.

[124] A. Sangwongwanich, Y. Yang, and F. Blaabjerg, "High-Performance Constant Power Generation in Grid-Connected PV Systems," *IEEE Transactions on Power Electronics*, vol. 31, pp. 1822-1825, 2016.

[125] P. Cortes, S. Kouro, B. La Rocca, R. Vargas, J. Rodriguez, J. I. Leon, *et al.*, "Guidelines for weighting factors design in Model Predictive Control of power converters and drives," in *IEEE International Conference on Industrial Technology,*, 2009, pp. 1-7.

[126] J. Rodriguez and P. Cortes, *Predictive control of power converters and electrical drives* vol. 37: Wiley. com, 2012.

[127] Y. Li, S. Jiang, J. G. Cintron-Rivera, and F. Z. Peng, "Modeling and Control of Quasi-Z-Source Inverter for Distributed Generation Applications," *IEEE Transactions on Industrial Electronics,* vol. 60, pp. 1532-1541, 2013.

[128] S. Bayhan, M. Trabelsi, H. Abu-Rub, and M. Malinowski, "Finite-Control-Set Model-Predictive Control for a Quasi-Z-Source Four-Leg Inverter Under Unbalanced Load Condition," *IEEE Transactions on Industrial Electronics,* vol. 64, pp. 2560-2569, 2017.

[129] B. Ge, Y. Liu, H. Abu-Rub, R. S. Balog, F. Z. Peng, S. McConnell, *et al.*, "Current Ripple Damping Control to Minimize Impedance Network for Single-Phase Quasi-Z Source Inverter System," *IEEE Transactions on Industrial Informatics,* vol. 12, pp. 1043-1054, 2016.

[130] M. Krstic, P. V. Kokotovic, and I. Kanellakopoulos, *Nonlinear and Adaptive Control Design*: John Wiley \& Sons, Inc., 1995.

[131] A. Charnes, E. L. Frome, and P. L. Yu, "The Equivalence of Generalized Least Squares and Maximum Likelihood Estimates in the Exponential Family," *Journal of the American Statistical Association,* vol. 71, pp. 169-171, 1976.

[132] C. J. Gajanayake, D. M. Vilathgamuwa, and P. C. Loh, "Development of a Comprehensive Model and a Multiloop Controller for Z-Source Inverter DG Systems," *IEEE Transactions on Industrial Electronics,* vol. 54, pp. 2352-2359, 2007.

[133] Y. Huang, M. Shen, F. Z. Peng, and J. Wang, "$ Z $-Source Inverter for Residential Photovoltaic Systems," *IEEE Transactions on Power Electronics,* vol. 21, pp. 1776-1782, 2006.